Evaporative Printing of Organic Materials and Metals and Development of Organic Memories

by

Sung Hoon Kang
B.S. Materials Science and Engineering
Seoul National University, 2000

Submitted to the Department of Materials Science and Engineering
in partial fulfillment of the requirements for the degree of

Master of Science

at the

MASSACHUSETTS INSTITUTE OF TECHNOLOGY

September 2004

Author .....
Department of Materials Science and Engineering
July 30, 2004

Certified by .....
Vladimir Bulović
Associate Professor of Electrical Engineering and Computer Science
Thesis Supervisor

Read by .....
Francesco Stellacci
Assistant Professor of Materials Science and Engineering
Thesis Reader

Accepted by .....
Carl V. Thompson
Stavros Salapatas Professor of Materials Science and Engineering
Chair, Departmental Committee on Graduate Students

Evaporative Printing of Organic Materials and Metals and Development of Organic Memories

by

Sung Hoon Kang

B.S. Materials Science and Engineering

Seoul National University, 2000

Submitted to the Department of Materials Science and Engineering
on July 30, 2004, in partial fulfillment of the
requirements for the degree of
Master of Science

Abstract

The advantages of directed printing make it the ideal fabrication tool for the ubiquitous electronic technologies of the future. However, direct printing techniques such as ink-jet technology, are currently limited to materials that can be processed in solution. We developed a novel micro-machined print head capable of expanding the capabilities of inkjet printing to metals and molecules that are suited for evaporative deposition. Deposition of metals is particularly desirable advantage of the proposed printer. We demonstrate arbitrary organic and metal patterns by printing, with the line width modulated by controlling the micro-machined shutter. With the challenges and solutions for ambient pressure printing are also studied. Additionally, the printer can be used for organic crystal formation, and controlled doping.

In the second part of the thesis we examine charge trapping and storage in organic thin film devices. We demonstrate that by controlled doping, we can engineer charge storage in active organic electronic devices. Charge trapping in organic heterojunction structures results in two distinct phenomena that both manifest as a memory behavior. Trapped charge can (1) increase the carrier mobility in organic structures, (2) generate current during the de-trapping process. Both processes are demonstrated in practical structures.

Thesis Supervisor: Vladimir Bulović
Title: Associate Professor of Electrical Engineering and Computer Science

Acknowledgments

"When times are good, be happy; but when times are bad, consider: God has made the one as well as the other. Therefore, a man cannot discover anything about his future." [Ecclesiastes 7:14]

Doing a graduate study on new fields in a new country was not easy for me, but there have been many people who helped me in time of need. I don't think I can thank all of them enough. I appreciate my parents for encouragements and cares. As an engineer, my father was glad that I continued my study and encouraged me to be a good researcher. My mother always supported my plan and prayed for me. Without them, I could not start my study at MIT. I appreciate my advisor, Prof. Vladimir Bulovic for his help and advices. His bright ideas and keen insight along with his excitement about new discoveries gave me a good example for an outstanding researcher. He has been very supportive to make our group to be a place that group members can enjoy working. I am grateful for Prof. Francesco Stellacci for reading my thesis and opening my eyes to nanoscale materials. I enjoyed his class and could learn how my knowledge of material science can be applied to a new and emerging field of nanoscience.

I would like to thank my group members. When I joined my group, I had no previous experience in organic material research. Seth Coe-Sullivan and Conor Madigan helped me learn to use various equipments and experiment techniques and they gave me valuable comments on my research. I appreciate Debbie Mascaro for her friendship. As a fellow material science student in the group, she was a good person to talk with, often sharing feelings about studying a new field of organic materials and gave encouragements. I would like to thank Jonathan (Yaakov) Tischler for helpful discussion about various topics. I appreciate Alexi Arango for his help in testing setup and advice about my future career. I appreciate John Kymissis for helps and comments. He gave me answers to most of questions that I had and always gave me valuable comments on my ideas from his insight. I appreciate Jianglong (Gerry) Chen for co-work in Hewlett Packard molecular jet printer project. From the experience

that I worked together with Gerry, I learned that one person plus one person is much more than two persons for doing a research. I would like to thank Valerie Leblanc who collaborated with me for HP project. She fabricated micro-machined shutters, which were crucial parts for the project. With her outstanding efforts, we could demonstrate the molecular jet printer. I would like to thank Dr. Paul Benning of HP, Prof. Marty Schmidt, and Prof. Marc Baldo, who gave me valuable comments about the project at weekly meeting. Presenting progress every week was a bit challenging, but it helped me materialize plans and improve my presentation skills.

I appreciate my Korean friends, especially my Korean classmates Wonjoon Jung, Kisuk Kang, Young-Su Lee, Heejae Kim, Donghwan Ahn, Hojong Kim, Byungchan Han and Zung-Sun Choi. I enjoyed their friendship and it is my good memory that I had time with them. I would like to thank Dr. Dae-Sung Choi who always welcomed my visit, gave me advices and encouragements and prayed for me. I would like to thank members of First Korean Church in Cambridge. I regained strength from fellowship, and their testimony. I would like to thank my girlfriend, Kiryoung Kim. Without her love and support, none of this would have been possible. Especially, I appreciate her consistent prayers and encouragements.

I would like to thank Republic of Korea Ministry of Information for a financial support. This research was supported by Hewlett Packard, the MARCO Focused Research Center on Materials, Structures and Devices, and the NSF Materials Research Science and Engineering Center.

The LORD is my shepherd, I shall not be in want.
He makes me lie down in green pastures, he leads me beside quiet waters,
he restores my soul. He guides me in paths of righteousness for his name's sake.
Even though I walk through the valley of the shadow of death, I will fear no evil, for you are with me; your rod and your staff, they comfort me.
You prepare a table before me in the presence of my enemies. You anoint my head with oil; my cup overflows.
Surely goodness and love will follow me all the days of my life, and I will dwell in the house of the LORD forever. [Psalms 23:1-6]

Contents

List of Figures

List of Tables

Chapter 1

Background

1.1 Properties of Organic Material

Organic materials are the foundation of the emerging field of active organic electronics. There are abundant interdisciplinary researches efforts precipitated by the perceived potential of organic material systems. These efforts include new material synthesis, the exploration of fundamental physical phenomena, the development of novel material growth techniques, and the structuring of practical active devices. Electroactive organic materials are now being considered as the active components in displays (Figure 1-1), electronic circuits,[4] solar cells,[5] chemical and biological sensors,[6] [7] actuators,[8] lasers,[9] memory elements,[10] and fuel cells.[11]

The flexibility of their molecular design and synthesis makes it possible to fine-tune the physical properties and material structure of organic solids to meet the requirements of technologically significant applications. In contrast to inorganic materials, active organic thin films can be deposited at much lower substrate temperatures (less than 120°C) in low-vacuum or atmospheric-pressure environments. It has been demonstrated that low-cost deposition techniques such as solution spin coating, casting, and even printing can be used for the deposition of solution-soluble organic materials. These processing advantages, together with the natural abundance of organic solids, make electroactive organic materials attractive for large-area and low cost applications.[12]

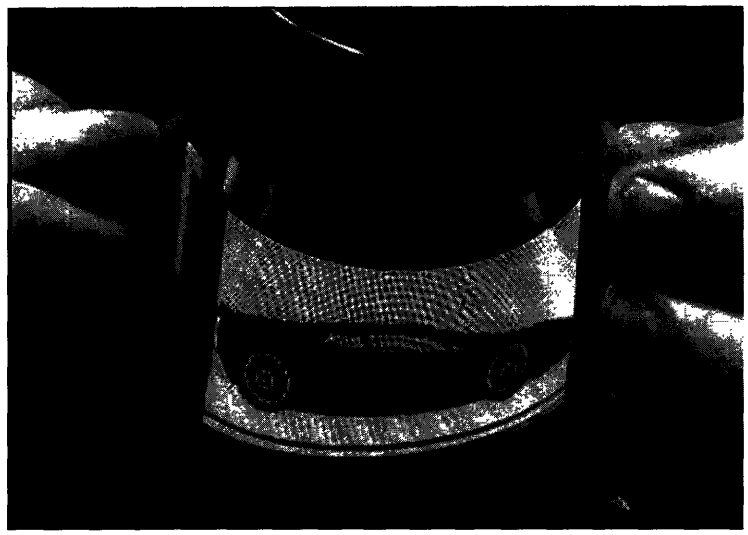

Figure 1-1: A flexible, monochrome, passive-matrix, phosphorescent organic light-emitting-diode display with 128 × 64 pixels at 60 dpi resolution. The display is fabricated on a 0.175 mm poly(ethylene terephthalate)(PET) substrate and is operated at a refresh rate of 60 Hz.[1]

There is increasing demand for 'ubiquitous electronics': low performance circuits incorporated within everyday items, such as smart identification tags on consumer goods, driving circuits for cheap flexible video screens, or even the next generation of mobile computing devices. The challenge in realizing the potential of these circuits is integration; mainstream fabrication techniques cannot directly pattern silicon devices on the required range of low cost substrates because of high processing temperature. The processing temperature of organic materials is less than 400 °C, and the substrate is typically at room temperature. Organic materials can be deposited simply by evaporation of materials without using very expensive and dangerous systems like molecular beam epitaxy (MBE) and metal organic chemical vapor deposition (MOCVD). They can be grown on almost any substrate for example, silicon, glass, and transparency film. In addition, large area bulk processing is an attractive characteristic from manufacturing point of view. The cost of organic material is not a significant portion of fabrication cost because typical device thickness is a fraction of 1 μm.

Organic materials have unique properties unobtainable in conventional materials. Vacuum deposition on plastic sheets also allows mass-production of large-area OLEDs via roll-to-roll processing.[13, 14] Transparent display were demonstrated.[15] For example, flexible, small-molecule-based organic light emitting device (OLED) have been demonstrated on ITO-coated polyester substrates.[16] Flexible polymeric OLEDs are well known in the literature, creating the potential for roll-up or conformable displays on curved surfaces.[17]

1.2 Principles of Organic Light Emitting Device

Organic electroluminescence (EL) is the electrically driven emission of light from organic materials, which was first observed in single crystal anthracene and in single crystal anthracene with approximately 0.1 mole % tetracene.[18] A variety of studies of the mechanisms for transport and injection were done, but the difficulty of single crystal growth and the large voltages required for macroscopic samples limited the practicality of such a scheme.[19] In 1987, Tang et al. of Kodak introduced a diamine and tris-8-hydroxyquinoline aluminum (Alq_3) double layer organic light emitting device (OLED), which combined thin film deposition techniques with suitable materials and structure to give high external quantum efficiency (1% photon/electron), luminous efficiency (1.5 lm/W), and brightness (>1000 cd/m^2) at a low driving voltage (< 10V).[20] In 1990, Friend et al. announced a conducting polymer polyparaphenylenevinylene (PPV)-based LED. [21] The development of a solution-processable precursor for PPV and soluble conjugated polymer derivatives simplified OLED fabrication by opening possibility of spin casting.[22] [23] Since then, there have been increasing interests and research activities in OLEDs, and enormous progress has been made in improving the luminance efficiency and device stability. Because of its potential application in flat pannel displays, most of major semiconductor companies around the world have invested in research and development of OLED flat pannel displays and some companies like Kodak, Seiko Epson, Samsung and Philips have developed proto types.

Why do OLEDs glow? OLEDs are different from conventional inorganic light emitting diodes (LEDs) in at least three aspects:

1. In OLEDs, electrons and holes combine to form localized excited states (excitons) that can relax to give off light, while inorganic LEDs emit light by recombination of electrons and holes across the energy band of the device.

2. Because organic films generally have disordered structure, charge carriers transport by hopping mechanism, which results in a power-law dependence of current on voltage ($I \propto V^m$), in contrast to the exponential dependence of current on voltage in inorganic LEDs ($I \propto \exp(qV/kT)$).

3. It has not been possible to dope organic materials to form luminescent p-n junctions. Typically, heterostructure devices with hole transport layer (HTL) and electron transport layer (ETL) are fabricated for efficient exciton recombination as shown in Figure 1-2.

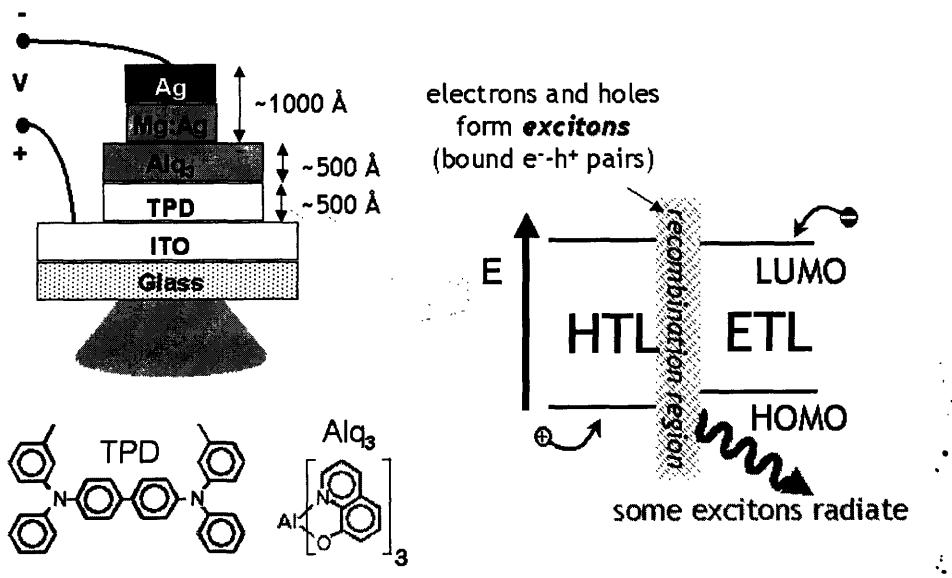

Figure 1-2: Typical structure of OLED and its operating principle

Figure 1-2 shows a typical device structure of an OLED. The molecular structure of exemplary molecules is shown in the figure. 8-hydroxyquinoline aluminum (Alq_3) is a

green light emitting material which preferentially transports electrons. N,N'-diphenyl-N,N'-(3-methylphenyl)-1,1'-biphenyl-4,4'-diamine (TPD) is a blue light emitting material which preferentially transports holes. Electrons injected from the cathode recombine with holes from anode and form radiative excitons. The anode is a typically high work function material for easy hole injection and is usually transparent so that light emission from the organic device can be directly observed. Indium tin oxide (ITO) is the most widely used anode material because it has a relatively high work function and is transparent in visible part of the spectrum. The carrier injection from the anode can be modified by depositing additional layer such as Poly-3,4-Ethylenedioxythiophene (PEDOT) poly(styrenesulfonate)(PSS) (PEDOT:PSS) on top of ITO.[24] For the cathode, low work function metals are ideal for easy electron injection but usually low work function metals are reactive. So, composite electrodes such as Mg:Ag and Li:Al are used to reduce reactivity while keeping the low work function.[19]

One of the important developments in the OLED technology is to use the guest-host doped emitter system.[25] A host material with optimized luminescent and transport properties can be used together with a various highly fluorescent guest dopants for high efficiency OLEDs. Another advantage of the doped emitter system is the improvement of OLED stability by transferring excitons to a highly emissive and stable dopant site to minimize non-radiative decay.[26] Baldo et al. developed a high-efficiency fluorescent OLEDs using a phosphorescent sensitizer by energetic coupling between phosphorescent (guest dopant) and fluorescent molecular species (host) through a long-range, non-radiative energy transfer. By using this approach, the internal efficiency of fluorescence can be as high as 100 % and we can nearly quadruple the efficiency of a fluorescent red organic light.[27] In this thesis doping will be used to facilitate charge trapping in active organic devices.

This thesis consists of two parts. In the first part, evaporative printing of organic materials and metals will be discussed. We demonstrate a new direct printing system, which can pattern metals and molecules. In the second part, charge trapping and storage in organic thin film devices will be discussed. We demonstrate that by

controlled doping, we can engineer charge storage in active organic electronic devices.

Chapter 2 will begin with an overview of different approaches for patterning organic materials. Shadow mask process, stamping and inkjet printing are popular approaches. We will briefly explain principles of each method and discuss pros and cons. From the overview, we will discuss the motivation of molecular jet printer as a new way of direct printing of organic materials and metals.

Chapter 3 will discuss the experimental setup of the evaporation chamber and the micro-machined shutter. Effusion cell is used for an evaporation source and computer programmable x and y axis manipulator and the micro-machined shutter is used to make patterns. For high resolution patterns, it is critical to reduce vibrations of the system. Special parts are designed for the purpose. We will describe the parts of the chamber and operation principles and fabrication procedures of the shutter.

Chapter 4 will show experimental data using the designed system for organic materials and metals. Fluorescent microscope, atomic force microscope and WYKO optical profiler are used to characterize printed patterns. Starting from a single pixel, printing arbitrary patterns are demonstrated with line width modulated by controlling the micro-machined shutter.

Chapter 5 will analyze the characteristics of the micro-machined shutter by applying bias to the chip. It is demonstrated that the shutter opening size can be modulated by controlling bias. In addition, processing issues such as broadening of patterns depending on source emission geometry and clogging of materials to the shutter are addressed. This chapter will conclude with numerical analysis results for different pressures.

Chapter 6 will discuss the future directions of this work. Challenges of molecular jet printer and possible solutions to overcome the issues are addressed. Then, we will give three examples for possible applications of the molecular jet printer. Organic crystal formation and controlled doping are promising applications of the system and we consider integration with conventional inkjet for full materials capabilities.

In Chapter 7, we will draw conclusions of the first part.

Chapter 8 will introduce demand for low cost high performance non-volatile mem-

ory and explain charge conduction mechanisms of organic materials.

Chapter 9 will discuss organic memory devices based on charge trapping mechanism. It will describe the structures and fabrication procedures of the devices as well as current-voltage (I-V) characteristics and time resolved I-V characteristics. Aluminum tris (8-hydroxyquinoline) (Alq_3) is used for organic layers and laser dye [2-methyl-6-[2-(2,3,6,7-tetrahydro-1H, 5H-benzo [i,j] quinolizin-9-yl)-ethenyl]-4H-pyran-4-ylidene]propane-dinitrile (DCM2) or silver (Ag) is used for an embedded layer. Magnesium (Mg) and silver (Ag) are used for electrodes. Then, it will explain a memory mechanism based on trap limited conduction model and it is verified from experimental data. Formation of nanoclusters that trap charge when very thin metal films are deposited on organic layers shows a good evidence of the proposed model.

Chapter 10 will discuss memory effects of reverse biased organic light emitting devices. It will describe the structures and fabrication procedures of the devices as well as current-voltage (I-V) characteristics and time resolved I-V characteristics. Alq_3, TPD, and DCM2 are used for organic layers and magnesium (Mg) and silver (Ag) are used for electrodes. Then, it will discuss memory mechanisms from experimental results. Charge storing is a proposed mechanism for memory behaviors and they are verified from photoluminescence quenching measurements. The electrical charge density is quantified from the room temperature optical measurements and I-V characteristics.

In Chapter 11, we will draw conclusions of the second part.

Part I

Evaporative Printing of Organic Materials and Metals

Chapter 2

Patterning Organic Materials

2.1 Different Approaches for Patterning Organic Materials

Lithography is the cornerstone of modern IC manufacturing. The ability to print patterns with submicron feature and placement of those patterns on a silicon substrate with better than 0.1 μm precisions is what makes today's chips possible. However, the conventional lithography techniques can not be used for organic materials because chemicals typically used for lithography dissolve or chemically react with organic materials. Therefore, alternative approaches for patterning organic materials have been developed. Among them, shadow mask, stamping, and inkjet printing are most actively studied methods.

2.1.1 Shadow Mask Patterning

The most common method for depositing molecular organic thin film is thermal evaporation. By heating a material source in vacuum, organic molecules are evaporated or sublimed and adsorbed onto substrates placed above the source. This allows a precise control in deposition of multilayer structures. In order to pattern the organic layers, a shadow mask is placed in vicinity of the substrate.[28] Because the background pressure is typically less than 10^{-5} Torr, very few gas collisions occur and the mean

free path of the evaporated molecules is larger than the chamber dimension. As a result, the organic molecules travel in the line-of-sight through the shadow mask to the substrate and form well-defined features. For better thickness uniformity, it is desirable to place a substrate far from the source.[29] The disadvantage of this method is low deposition efficiency. If we consider the total amount of evaporated materials, only small portion of materials reach the substrate. Furthermore, most of molecules that travel to the substrate deposit onto the shadow mask, necessitating periodic cleaning of the shadow mask to ensure sharpness of features. Typically, the material usage efficiency is less than 5 % in high vacuum and it gets worse as the background pressure increases. In addition, the sharpness of deposited feature decreases as the spacing between the substrate and the mask increases. Putting the mask in intimate contact with the substrate results in the best sharpness, but can also result in damage of the underlying layers.

2.1.2 Stamping

In the stamping technique, a patterned elastomer (usually polydimethylsiloxane(PDMS)) is used as the mold, stamp, or mask to generate or transfer the pattern. Figure 2-1 shows the schematic of the stamping process, which is often called as soft lithography. Soft lithography offers an advantage over photolithography and other conventional microfabrication techniques for applications in which patterning of nonplanar substrates, unusual materials, or large area patterning are the major concerns. To date, this method has been demonstrated for patterning of relatively simple, single-layer structures. It is limited by speed and chemistry of the stamp inking process and pattern irreproducibility due to the adhesion of mold and replica.[30]

2.1.3 Inkjet Printing

Inkjet printing is familiar as a method for printing computer data onto paper or transparencies. Industrially, it is also widely used to print date information onto cans and bottles. Inkjet printer uses drop-on-demand systems. A heated plate causes

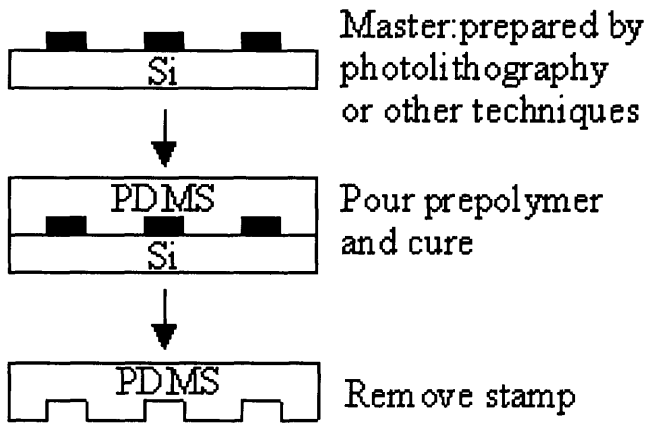

Figure 2-1: Schematic procedure of stamping

a vapor bubble to form and eject a droplet of ink through a nozzle. The plate temperature rises to about 300°C as the current pulse of a few microseconds passes through it. The main challenge of this technology is to avoid clogging of the nozzle by dried ink. The nozzle sizes are in the range of 20-30 μm. Smaller nozzles allow smaller droplets and higher resolution. Droplets are in the range of 10-20 pL. Ink viscosity and surface tension are crucial parameters in the design of a printer head. Inkjet printing of organic light-emitting diodes might one day allow patterning of arrays of active device pixels. So far, however, it has not been possible to inkjet print pinhole-free layers.[31] Pinholes lead to shorting of the layered devices. Furthermore, due to the presence of a solvent in the ink-jet droplet, the printed material generally mixes with the underlying organic layer that was previously on the substrate. For such multilayer printing, the dyes redistributes between layers while the droplet is wet changing the device cross section and preventing formation of sharp heterointerfaces.

Since the resolution of displays is similar to that of printed paper, inkjet printing should readily lend itself to OLEDs once a wider range of materials and multiple layers become possible. Inkjet printing can be used for printing organic transistors. However, a major problem has been the relatively large size of inkjet dots (>50 μm).[32] The first inkjet printed organic transistor was demonstrated by Sirringhaus

et al.[4] In this case, fine lines were obtained by printing on a stepped surface, such that the ink was pulled into the step as it dried. The source and drain electrodes were printed in a conducting polythiophene in this way and then the semiconducting polymer layer was spin-coated on top. Printing an electrode on either side of a lithographically defined 5 μm polyimide barrier allowed a 5 μm channel length to be defined, despite the drops being printed with a resolution of 50 μm.

Printed patterns of conducting polymer have also been reported by Pede et al.[33] They printed polymer solution onto a solid substrate and then doped the printed polymer to the conducting form with iodine vapor. Polymer was also printed onto a layer of a dopant ($Fe(ClO_4)_3$) to induce conductivity and monomer was similarly printed onto an oxidant layer to induce polymerization and doping. Resolution was about 50 μm. Printing these solutions required a special solvent-resistant print head. It should also be noted that inkjet printing is very vulnerable to blockage due to solvent drying; hence, a printing method that relies on rapid evaporation of solvent is intrinsically difficult to maintain.

There are reports that inkjet printing are used for various materials. Inkjet printing of ceramics was developed by Blazdell et al.[34] A dilute dispersion of zirconia and polyvinylbutyral binder in solvent was printed and dried to a 60 vol % ceramic dispersion that could be burnt out and sintered to dense ceramic. Many of the materials previously discussed can be printed as fine particles or as solutions. Since sedimentation must be avoided in inks, particle sizes should be less than a micrometer.

There is much interest in conventional inkjet printing with nanoparticle inks.[35] One obvious target is to print nanoparticulate suspensions of gold or other metals to form conductors for electronics. It is also possible to form electrodes by printing a solution of a metal precursor, followed by conversion to metal. Silver metallorganic ink has been described which converts to metal below 300 °C.[36] Multilayer printing, with firing steps between layers, has been used to deposit silver electrodes with a resistance of 1 Ω/square for photovoltaic cells. Bismuth was added to improve adhesion and further heat treatment was needed to achieve low contact resistance.[37] More recently, copper contacts have been printed using a precursor route.[38]

2.2 Motivation of Molecular Jet Printer

Inkjet printing is an attractive solution to the fabrication needs of ubiquitous electronics. It also promises to transform the electronics industry from reliance on a relatively small number of multi-billion dollar fabrication facilities, to a delocalized model where the end user prints their own electronics with much greater control over design and function. The semiconducting materials in inkjet printed circuits are organic molecules or inorganic nanoparticles. But, inkjet printing is currently restricted to materials that can be processed in solution. Insoluble semiconductors and metals are not suited for present inkjet technologies.

Three major components required in printed electronics are thin film transistors, light emitting devices and photodetectors. The performance of organic thin film transistors depends critically on the morphology of the organic channel. In Figure 2-2, we show the performance characteristics of thermally-evaporated pentacene transistors. These p-channel devices have charge transport mobility, $\mu > 1$ cm^2/V·s, and a threshold voltage close to zero; specifications that typically exceed p-channel amorphous Si transistors.[2]

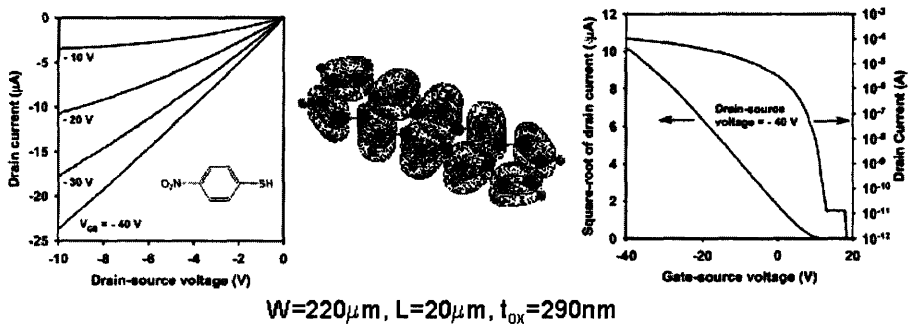

Figure 2-2: Current voltage characteristics of high performance thermally-evaporated pentacene transistors. Also shown: a numerical simulation of the highest occupied molecular orbital of pentacene and (inset, left) a nitrobenzenethiol, used to chemically functionalize the gold contacts. Optimum charge transport mobility requires overlap of the molecular orbitals of pentacene and is highly dependent on molecular packing.[2]

Optimum performance of pentacene devices requires the creation of a strained,

close-packed molecular layer at the gate oxide interface.[39] Exposure to solvents relaxes this layer and degrades the performance by at least an order of magnitude, necessitating film deposition by thermal evporation.[40] To improve the performance of solution-processed devices, some polymers incorporate non-conductive alkane side chains similar to liquid crystals.[41] However, self-organization in solution-processed devices can only approach the performance of unstrained thermally-evaporated films, and the charge transport mobility of self-organizing polymers remains inferior to strained, close packed pentacene by at least an order of magnitude.[42]

Thermal deposition of OLEDs is also beneficial over the solution processing of OLED layers. There are two obstacles to generating solution-processed OLEDs: first, the most efficient OLEDs require complex device structures with at least three layers, and, maintaining solvent compatibility in multiplayer structures is challenging. Secondly, the OLED lumophores phase segregate in mixtures with a soluble polymer host, leading to significant losses in efficiency.

	Thermal evaporation	Solution processing
Thin film morphology	Amorphous Polycrystalline Crystalline	Amorphous
Strained layers	Yes	No
Purity	High	Depends on solvent
Multilayer devices	Yes	Bilayer possible, > 2 layers difficult
Molecular doping	Yes	Dopants phase separate
TFT mobility	> 1 $cm^2/V{\cdot}s$ [43]	< 0.1 $cm^2/V{\cdot}s$ [44]

Table 2.1: A comparison of solution processed and thermally-evaporated devices demonstrating the clear need for a printing technique capable of patterning devices by an evaporative technique. Despite their superior characteristics in devices, thermally evaporated materials must be patterned by shadow masks.

Thermally evaporated and solution processed devices are compared in Table 2.1. In addition to the deleterious effects of solution-processing on the performance of both organic TFT's and LED's, many solution-processed devices require potentially hazardous solvents that may also increase impurity levels. In contrast, it is much easier to maintain the required purity standards in thermally-evaporated devices.

We propose to demonstrate a micro-machined thermal evaporator, or 'molecular jet printer', thereby combining the proven film deposition advantages of thermal evap-

oration with the high speed patterning capability of directed printing. The print head will be mounted on an X-Y translation stage. There is a control in the Z direction to maintain print head-substrate spacing of < 100 μm.

The proposed print head for organic materials has two main components:

1. micro-machined shutter controlling an opening of < 100 μm
2. evaporatioin source to contain the organic material

Chapter 3

Experimental Setup

3.1 Evaporation Chamber

We built a thermal evaporation chamber to house the effusion cell, MEMS shutter and the substrate. The system has following features:

1. x and y axis motion is controlled by computer-programmable motorized manipulator.

2. the substrate and the MEMS shutter spacing is adjustable by z axis manipulator.

3. the source and substrate spacing is controlled by a manipulator with the maximum displacement 10 inch.

Figure 3-1 shows the cross-section of the evaporation chamber. The base pressure of the chamber is 1×10^{-7}Torr. The system is connected to a transfer line, which enables us to do multilayer deposition using various deposition techniques without breaking vacuum as shown in Figure 3-2.

3.1.1 Effusion Cell

Luxel Radak II furnace (available from Luxel Corporation, Friday Harbor, WA) is installed for stable temperature control and capability of controlling source temper-

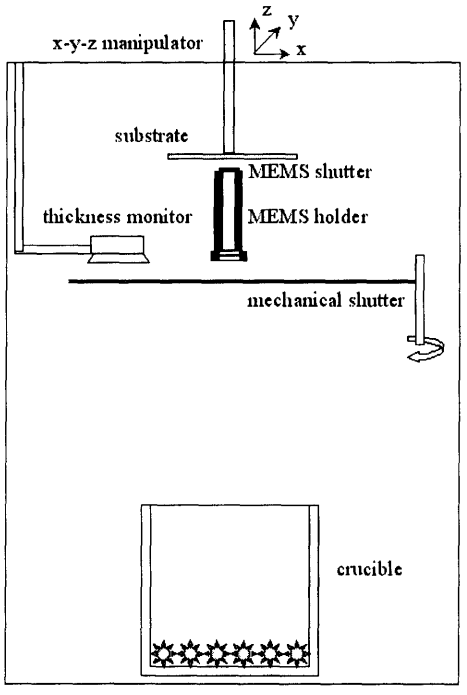

Figure 3-1: Cross-section of the evaporation chamber

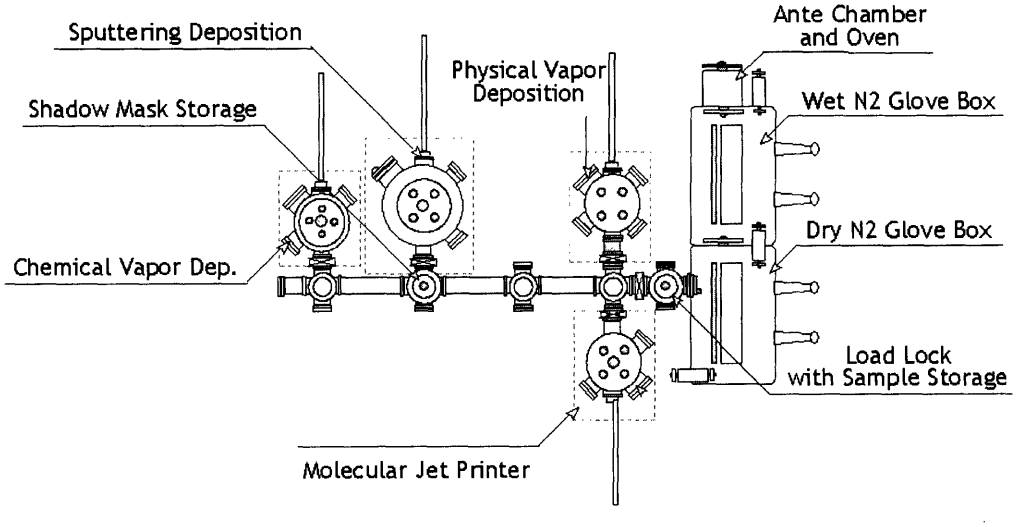

Figure 3-2: Integrated growth system

ature from room temperature up to 1500 °C. Figure 3-3 is a schematic picture of the furnace. The effusion cell controller can control temperature by receiving feedbacks from a crucible through type C thermocouples. It also has capability of programming heating curve. Due to stable temperature control, we can demonstrate steady-rate deposition at very high growth rates compared with a typical evaporation source using a tungsten metal boat. Typical growth rate for a boat type source is 1-10 Å/s while the highest growth rate we tried with the effusion cell is over 100 Å/s. The reason for this difference is the effusion cell has feedbacks while a boat type source does not. Depending on materials we use, crucibles made of different materials are used. For organic materials and gold, we use high purity alumina crucible and for silver, we use a molybdenum crucible.

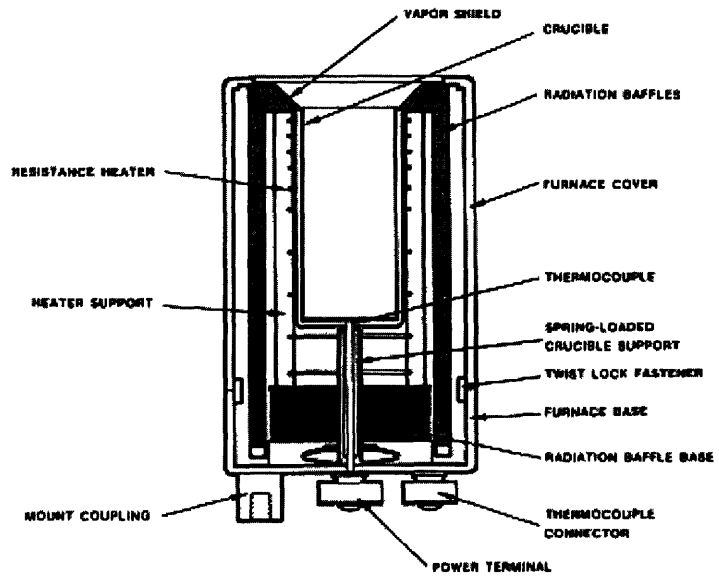

Figure 3-3: Micro furnace (Luxel Radak II)

We calibrated temperature of the controller using a Fluke 50 series II thermometer. As it is shown in the Figure 3-4, there is a linear relation between two readings within a range of typical organic material deposition temperatures. Type C thermocouple

has a better characteristic in high temperature region, because it is typically used at high temperature while type K thermocouple cannot be used over 1200 °C.

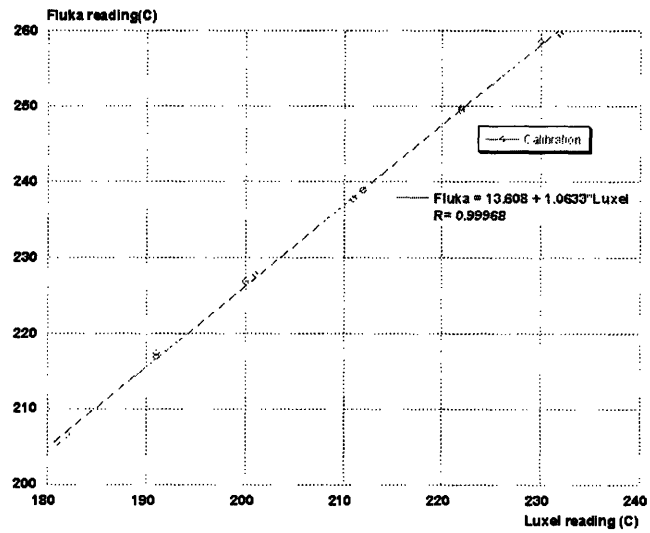

Figure 3-4: Temperature calibration of the micro furnace

3.1.2 Computer Programmable X and Y Axis Manipualtor

The x and y axis motion of the substrate is controlled by stepping motors. Attached to a micrometer stage with 25 μm revolution. The stepping motor has following features:

1. Programmable microstepping rates up to 51,200 steps per revolution
2. Drive rates to over 3 million pulses per second
3. RS-232 communication to program motions

By moving the substrate with this computer programmable x and y axis manipulator, we can print material patterns with arbitrary shapes. When the substrate holder moves, there can be vibrations of the shaft, which holds the substrate holder.

This can be understood as a classical free body movement. This is an important issue because when the chamber was assembled, the resonant frequency of the assembly was low and the substrate holder vibrated for a long time with a small force. We did theoretical study about this issue to select a diameter of the shaft. In addition, there is another vibration source: because the chamber keeps vacuum using a dry pump, the vibration from the roughing pump can cause the chamber to vibrate. To reduce this effect, we installed additional fixtures which will be described in the next paragraph.

3.1.3 Approaches for Reducing Vibrations

In the previous paragraph, we mentioned that there are at least two vibration sources in this system. One is the x-y manipulator and the other is a roughing pump. Figure 3-5 is a result of simplified calculation based on a free body oscillation model. If the vertical alignment of the shaft is off 1 degree, then a horizontal force of 0.087 N is applied to the substrate holder. From the vibration analysis, the deflection force for 25 μm displacement is 0.073 N. So, significant displacement of the substrate holder can happen which is beyond our target resolution (25 μm) if the vertical alignment of the shaft is off 1 degree. As we increase the diameter of the shaft, we can reduce this effect. However, the inner diameter of the tube where a shaft is welded on to the flange of the tube is 1.37 inch. So, if we use a large diameter shaft, the motion of a substrate will be limited and the patterning area is reduced. We chose 0.75 inch as a shaft diameter so that we can cover 0.5 inch square deposition, with maximum expected vibration error of 0.1 μm.

Figure 3-6 is the top view of the chamber with additional fixtures.

Figure 3-7 shows detailed images of the parts 1, 2 and 3.

In Figure 3-7, part 1-1 is a part, which holds the part 1-2 so that it can keep the MEMS shutter vertically and horizontally precisely aligned by connecting with part 2 and part 3. Part 1-2 can rotate the MEMS shutter out of the deposition path so that blanket deposition is also possible when MEMS shutter is not used. Part 2 is a part which holds the MEMS shutter so that it can be positioned exactly same location

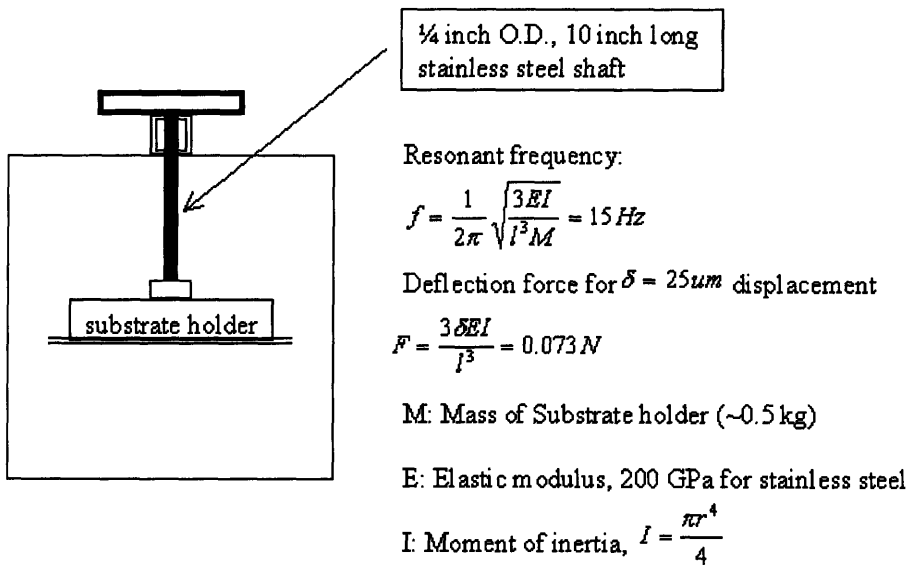

Figure 3-5: Vibration analysis

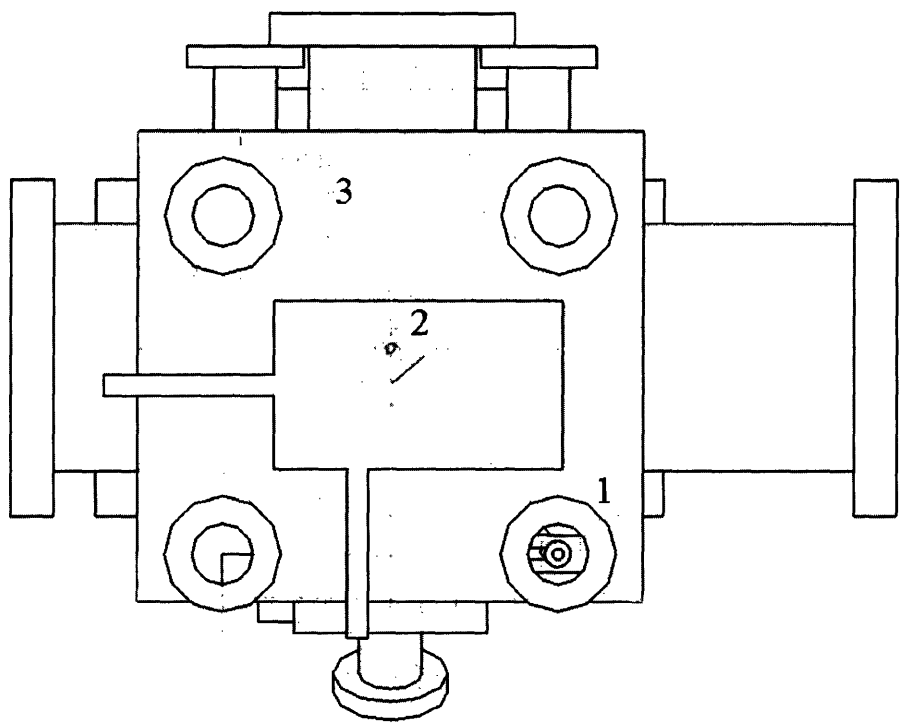

Figure 3-6: Top view of the chamber with additional fixtures

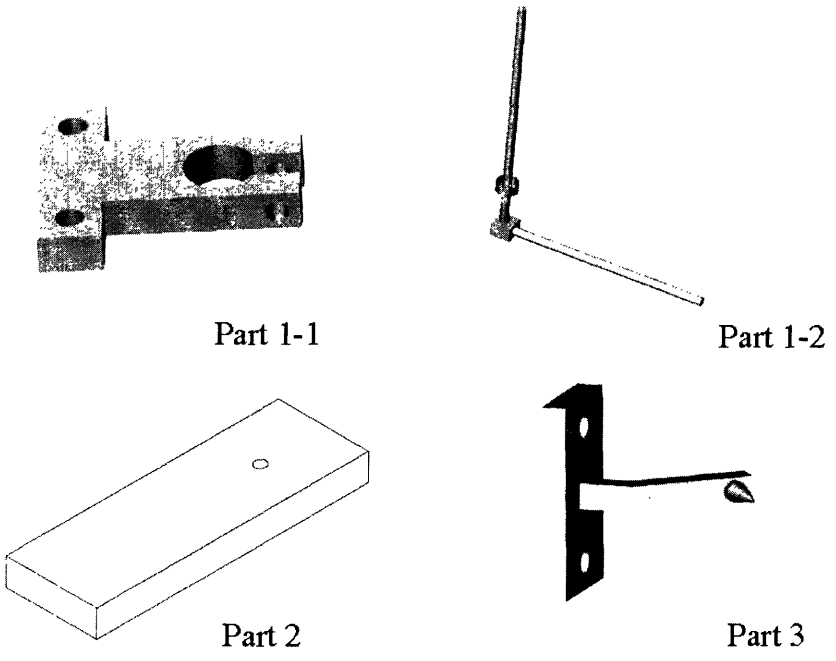

Figure 3-7: Detailed Images of Parts 1, 2 and 3 of Figure 3-6

every time. In part 2, there is a hole in which the sharp cone shape of part 3 goes in so that we can reduce the vibration in x and y direction. Experimental data shows that there is small broadening of the deposited patterns by vibration effects because of effectively reduced vibrations. Figure 3-8 shows the side view of the chamber with the location of important parts.

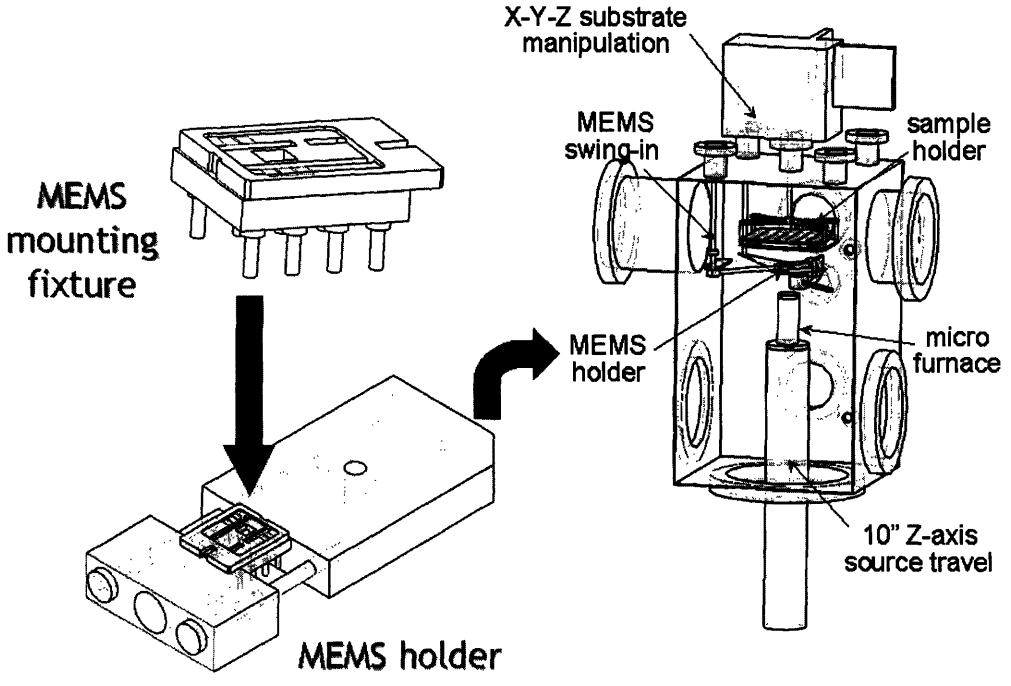

Figure 3-8: Side view of the printing chamber

In our system, we used a specially designed ceramic package which allows electrical connection to the MEMS shutter without increasing the spacing between the substrate and the MEMS shutter. At the center of this package, there is an opening which allows evaporated material to travel from the bottom to a substrate through the MEMS shutter. This package is fabricated by Kyocera following the design in Figure 3-9.

Figure 3-10 shows the pictures of the assembled printing system and the micro-furnace used for an evaporation source.

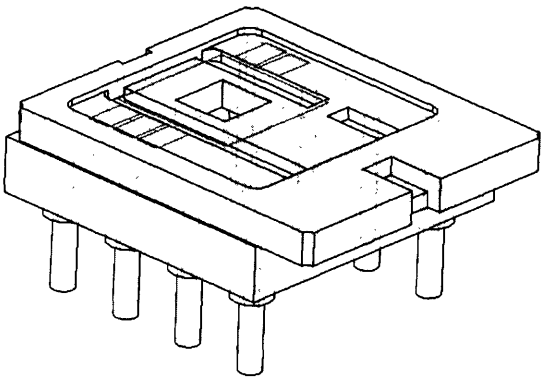

Figure 3-9: Package for the MEMS shutter

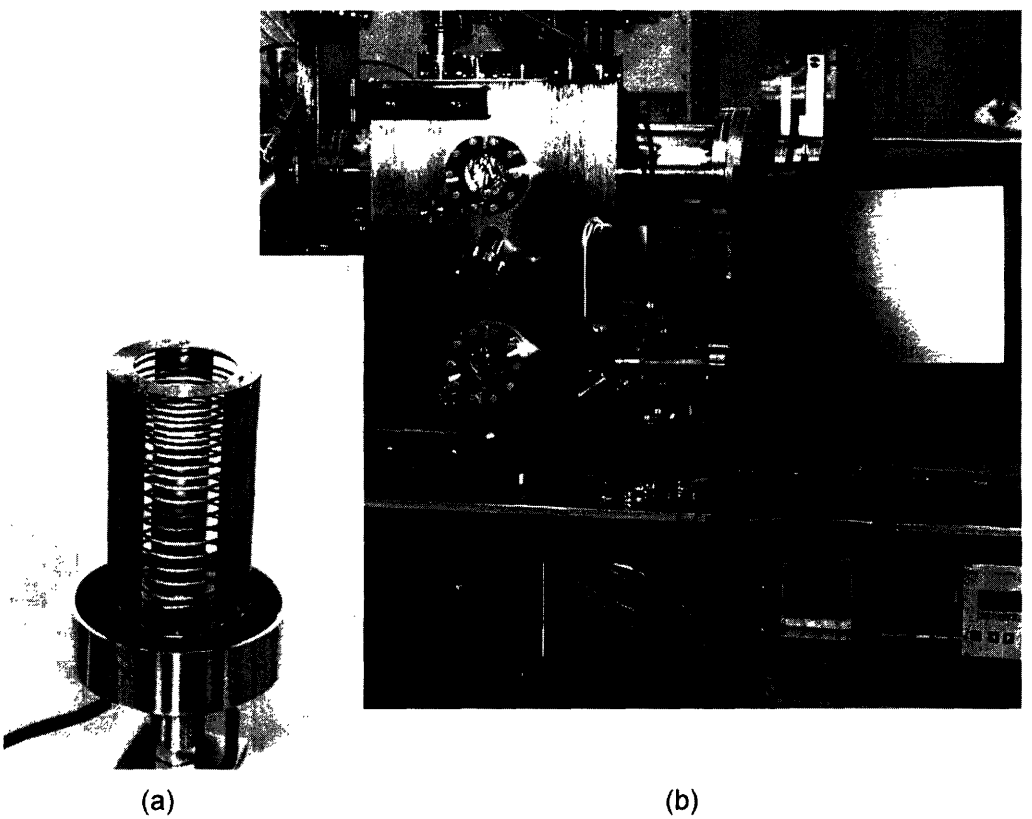

Figure 3-10: Actual picture of the printing system (a) microfurnace (b) chamber

3.2 MEMS Shutter

3.2.1 Operation Principle of the MEMS Shutter

The MEMS actuator is composed of a fixed and a mobile interdigitated electrodes. Figure 3-11 shows principle of the comb-drive electrostatic actuator that is the key part of the MEMS shutter.

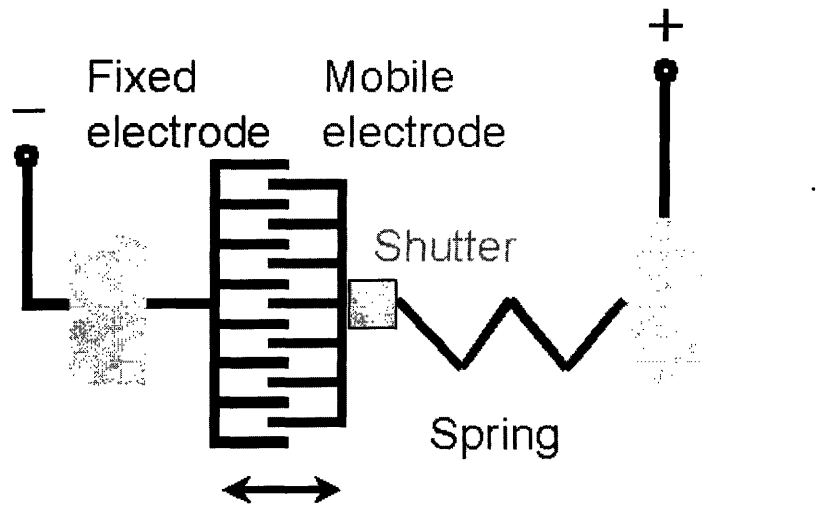

Figure 3-11: Principle of the comb-drive electrostatic actuator

As shown in Figure 3-11, one electrode is fixed and the other electrode is moving by electrostatic interaction when a voltage is applied to the actuator. And the mobile electrode is connected to the cover of the shutter by an elastic component which can adjust length.

Figure 3-12 shows the geometry of the electrodes used for calculating a displacement of the electrodes as a function of the applied voltage.

For given geometry, if there are n fingers, the capacitance of the interdigitated electrodes can be written as

$$C = \frac{2n\epsilon h(y + y_0)}{d} \tag{3.1}$$

, where ϵ is the dielectric constant.

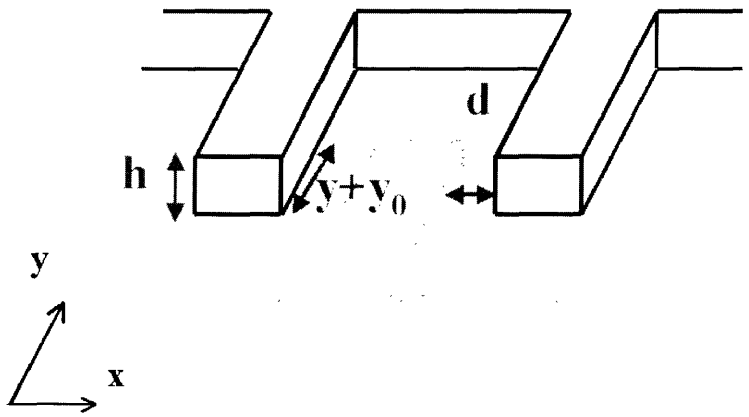

Figure 3-12: Geometry of electrodes

Then, the electrodes are attracted by an electrostatic force:

$$F_{el,y} = \frac{1}{2}\frac{\partial C}{\partial y}V^2 = \frac{n\epsilon_0 h}{d}V^2 \tag{3.2}$$

The mobile electrode is therefore displaced of a distance y toward the fixed electrode.

$$F_{el,y} = k_y y \tag{3.3}$$

so that

$$y = \frac{n\epsilon_0 h}{k_y d}V^2 \tag{3.4}$$

From the above equation, we can see that the displacement of the mobile electrodes can be modulated by applied voltage. Hence, the relative displacement of the mobile electrodes to the fixed electrodes can be controlled. Figure 3-13 shows the device layout of the MEMS shutter, which can control the opening of the shutter by the comb-drive actuator.

The black square in the middle of the figure shows the opening of the MEMS shutter. Figure 3-14 shows the schematic image of the three dimensional view of

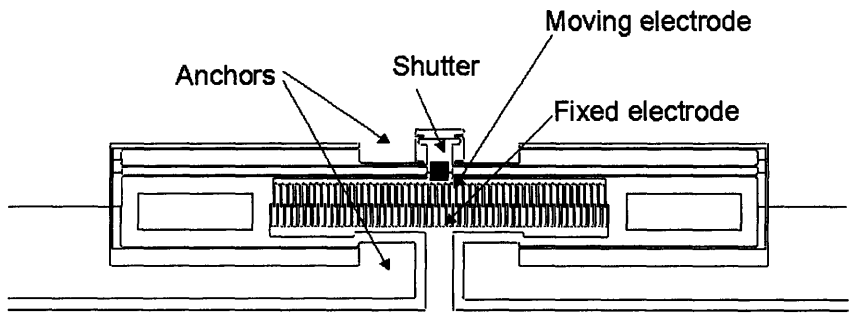

Figure 3-13: Device layout of the MEMS shutter

the MEMS shutter. Figure 3-15 is the picture of the fabricated shutter following the design of the Figure 3-13.

3.2.2 Fabrication Procedures of the MEMS Shutter

The MEMS shutter was fabricated by Valerie Leblanc in Professor Marty Schmidt's group at MIT. Figure 3-16 shows the schematic diagram of the MEMS fabrication process.

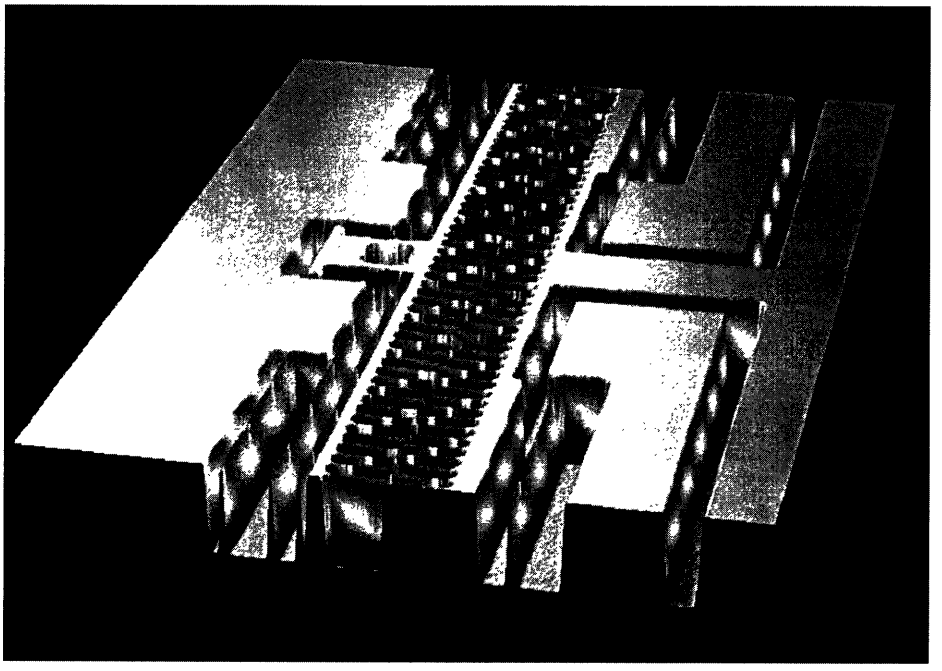

Figure 3-14: Schematic view of the MEMS shutter in three dimension

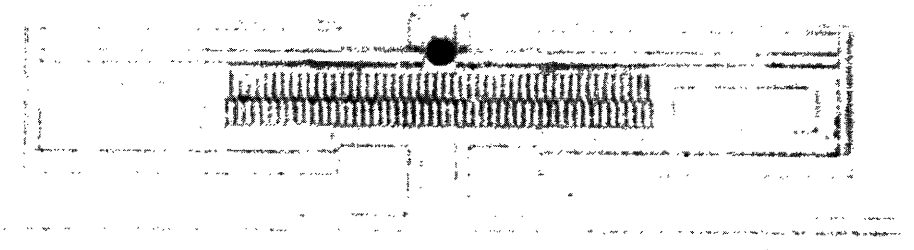

Figure 3-15: Actual MEMS device layout

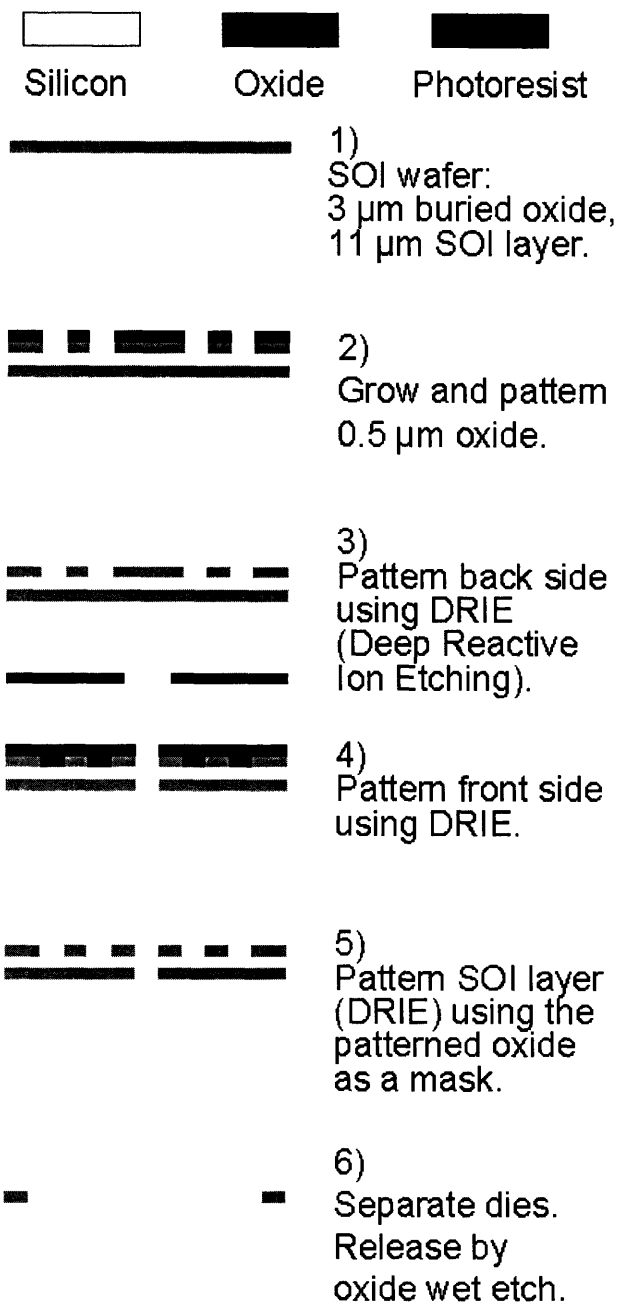

Figure 3-16: Fabrication procedures of the MEMS shutter

Chapter 4

Experimental Data

4.1 MEMS Shutter Characteristics

The chip layout of the MEMS shutter is shown in Figure 4-1. The total chip size is 4.3 mm by 4.3 mm and the 25 μm opening is centered with respect to the chip. Two large pads are used for electrical connection to a power source.

The electrical characteristics of the MEMS shutter are measured by Agilent 4156C Semiconductor Parameter Analyzer. Figure 4-2 (a) shows the current-voltage characteristic between two pads shown in Figure 4-1. The I-V characteristic shows that the chip has a higher resistance compared with a typical silicon wafer, but the electrical connection between two pads is good. Figure 4-2 (b) shows the curent-voltage characteristic between one pad and backside of the chip. This data shows that the leakage current of the chip is negligible and the chip is fabricated well.

The opening size of the MEMS shutter can be modulated by bias as it is described by Equation 3.4. Figure 4-3 shows optical microscope images of the MEMS shutter as the applied bias changes. The shutter is initially fully-open. By displacement of comb drive, the shutter start to close as voltage increases. If the voltage is over 30 V, the shutter is completely closed by covering the opening in the MEMS chip through the comb drive displacement.

Figure 4-4 shows summary of data taken from Figure 4-3. The opening size of Figure 4-4 (a) is measured from optical microscope images. The displacement of

Figure 4-1: The chip layout of the MEMS shutter

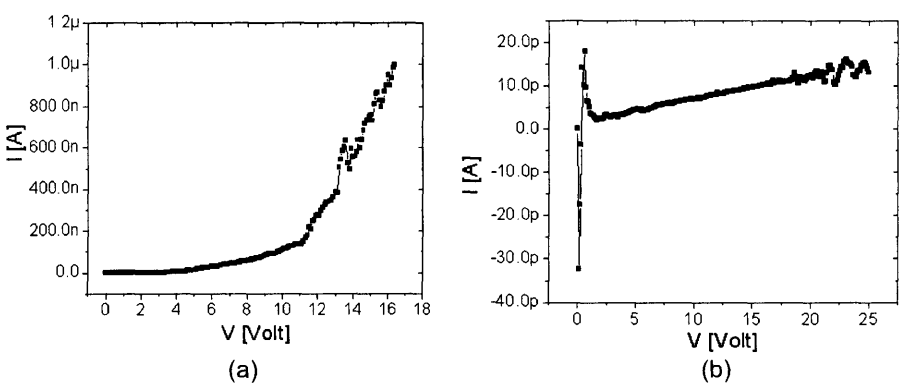

Figure 4-2: Electrical characteristics of the MEMS shutter (a) between two pads (b) between one pad and backside of the chip

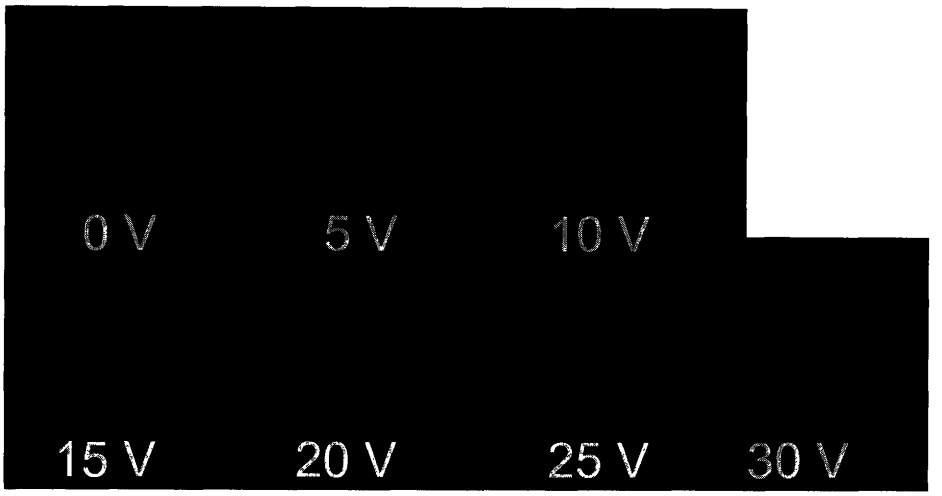

Figure 4-3: Modulation of the MEMS shutter opening by applied voltage

shutter in Figure 4-4 (b) is calculated by subtracting the opening size from the initial opening size. The data is consistent with the theoretical prediction of Equation 3.4 that the shutter displacement is proportional to the voltage square.

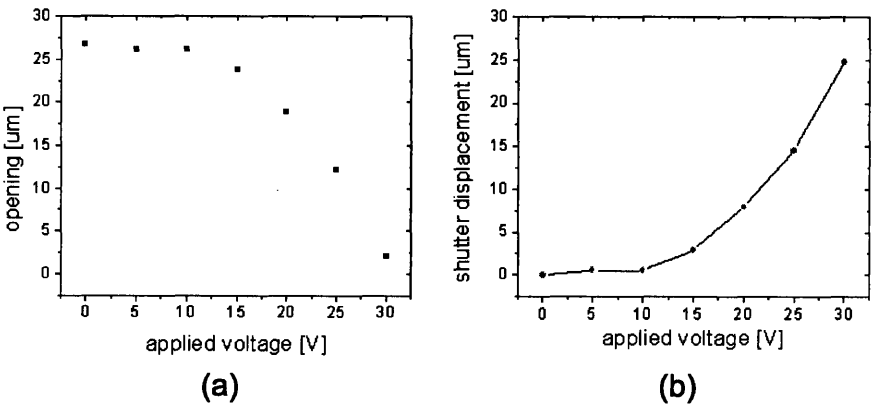

Figure 4-4: MEMS shutter modulation data from Figure 4-3 (a) opening size vs voltage (b) shutter displacement vs voltage

4.2 Deposition of Organic Material, Alq_3

By using the printer head, a square pattern of organic semiconductor can be deposited as seen in Figure 4-5. An electroluminescent material aluminum tris(8-hydroxyquinoline) (Alq_3) was used. Alq_3 is chosen because it is a frequently used material for making OLEDs and it is easy to observe Alq_3 patterns using a fluorescent microscope. The film growth is stable and we can get very high growth rate. Though the limit was not explored, a steady growth rate of 100 Å/s can be achieved without any difficulty. Then, by translating in x-direction, 1×3 array of pixels are formed as shown in Figure 4-5.

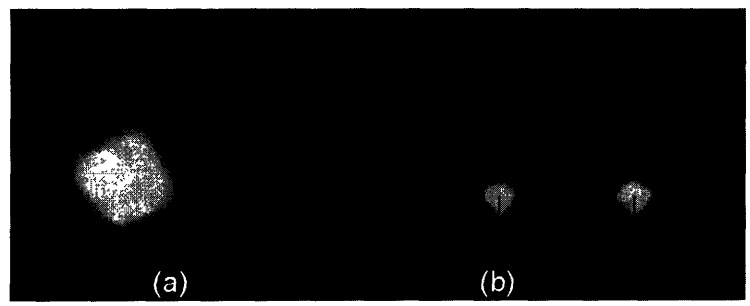

Figure 4-5: Fluorescent image of Alq_3 using the micro-machined printer head: (a) Single pixel (b)1×3 Pixel Array

Figure 4-6 shows fluorescent microscope images of Alq_3 patterns that are formed by x-y movement of the substrate stage. The deposition thickness was monitored by a quartz crystal thickness monitor. This demonstrates that arbitrary patterns can be printed by manipulation of stage.

One of the advantages of the fluorescent microscope is that it is easy to see the patterns that are deposited even though the thickness of printed materials are not very thick. However, the microscope image can not give accurate sizes of each pixel because of the optical bluring in the microscope optics. In order to see actual profiles of printed patterns, WYKO optical profiler is used. Before measurement, 300 $\mathring{A}$ of silver was blanket deposited over the substrate for better contrast of reflectivity. Figure 4-7 is the 3D profile of Figure 4-6(a). From the given image, the thickness of

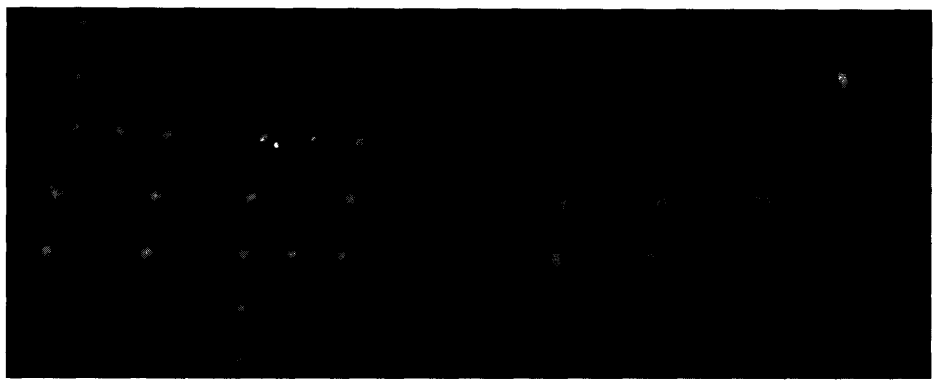

(a) (b)

Figure 4-6: Fluorescent image of deposited characters (a) hp (b) MIT: each pixel is $35 \times 35\mu$m, and the spacing between them is 50 μm.

the center of each pixel is highest and each pixel has a shape of mountain peak. This is because the flux of the evaporated material is the highest at the center of aperture when it is perfectly aligned with a source and as it goes outside, the flux decreases because of some of materials deposited at the wall of the aperture due to geometric relation between aperture depth and size. Because the temperature of the MEMS shutter is kept at room temperature, the molecules that hit the wall of the aperture adsorbed on the surface of the wall. If large amount of materials are evaporated, this deposit can change the opening size of the MEMS shutter.

Once, we have confidence in substrate manipulation, we deposited an array of 4×10 pixels to test parallel and vertical alignment between pixels. As it is shown in Figure 4-8, the pixels have good parallel and vertical alignment. In the Figure 4-8, not every pixel is shown since the image is not clear at lower magnification. The pixels were dim as the deposited film was very thin.

As described in introduction, deposition of metals is a particularly desirable advantage of the molecular jet printing. Metals are usually used as electrical connections between active layers and a power source. Therefore, it will be desirable that we can form lines in addition to separate pixels.

As a preliminary step, we form Alq_3 lines by slow stepping motor movement

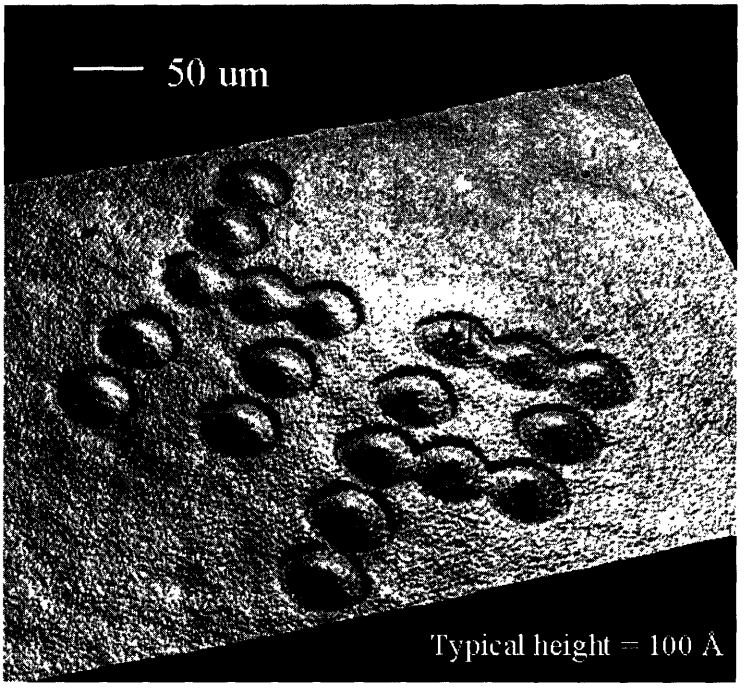

Figure 4-7: 3D Profile of deposited letters in Figure 4-6(a)

Figure 4-8: 4×10 pixel arrays for testing alignments between pixels

while continuously evaporating materials. The length of each line in Figure 4-9 is 2.5 mm long and both lines are straight. This shows that the motion of the x and y manipulator is good enough to form lines that can be used as interconnects if we change the material. For these depositions, the shutter remained open during the entire depostion.

Figure 4-9: Alq_3 lines

In order to demonstrate the ability of the MEMS shutter, we printed letters MIT using Morse Code, using the experimental setup in the inset of Figure 4-10. At 0V applied bias the MEMS shutter is open and it closes when > 30V of bias is applied. The fluorescent image in Figure 4-10 shows the printed patterns. By comparing the printed patterns with the experimental setup, it is clear that no material is deposited when the shutter is closed. The thickness of the printed patterns depends on the moving speed of the manipulator because more material is deposited if the moving speed is slow. This is shown in line (1) and (2). The image of line (2) is brighter than line (1) because more material is deposited due to slower moving speed. From position (3), two pixels overlap slightly if the spacing between them is less than 40 μm. This defines the minimum pixel size using the given shutter and the spacing between the substrate and the shutter. If the spacing between the MEMS shutter and the substrate is reduced, the broadening of pattern is reduced as it will be discussed in the next chapter. The break point of the position (4) is clear because it has larger spacing between pixels. If we compare the image of space between the Morse code "M", and "I" with that of "I" and "T", there is no difference in the image by using

different moving speed when the shutter is closed. This shows that almost no material is deposited when the shutter is closed.

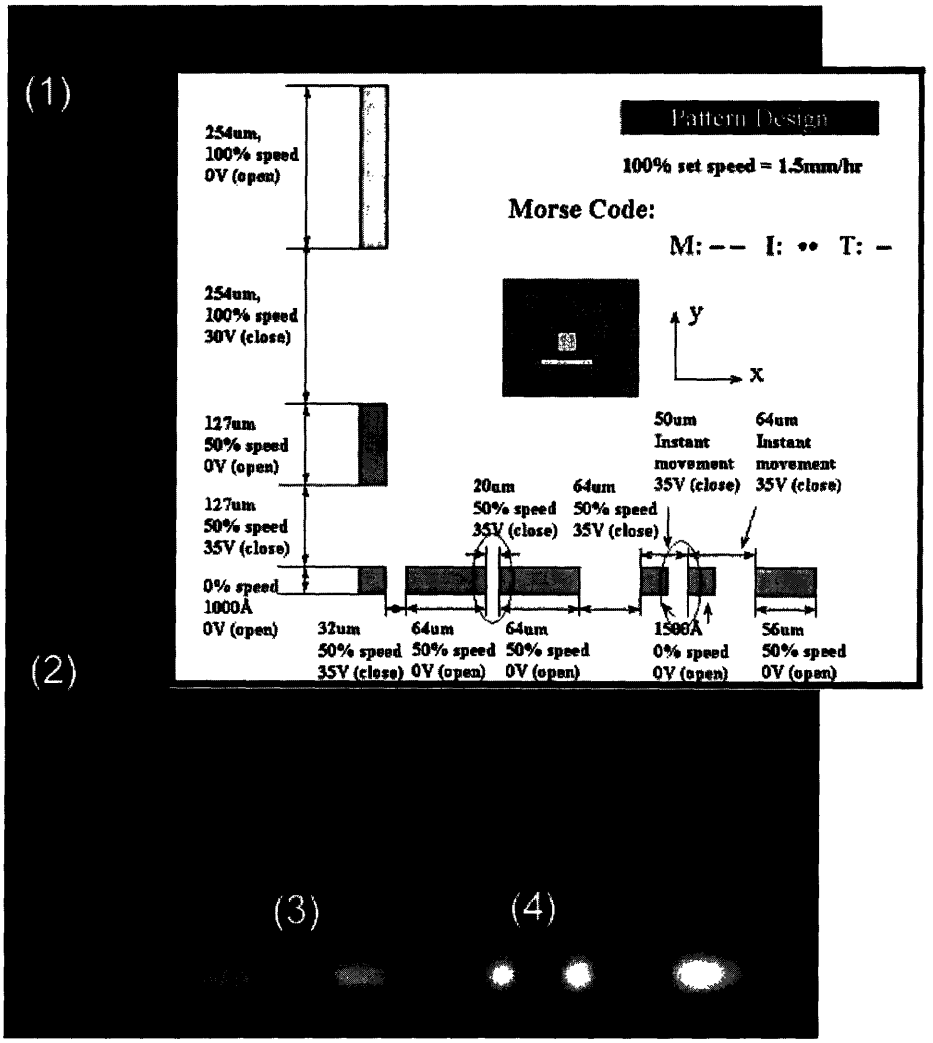

Figure 4-10: Printing of letters MIT using Morse code and experimental set-up (inset) for manipulation. The voltage refers to the bias applied over the MEMS.

Furthermore, control of pattern sizes by applying different voltages over the MEMS is studied. Figure 4-11 shows the images of printed patterns with different MEMS voltages. This study is done using a diamond shape opening. (1), (2), and (3) are deposited pixels at different MEMS voltages. Two pixels are printed for each voltage to check the reproducibility of the shutter. From the fluorescence intensity we can

qualitatively state that the pixel size decreases when MEMS voltage is increased.

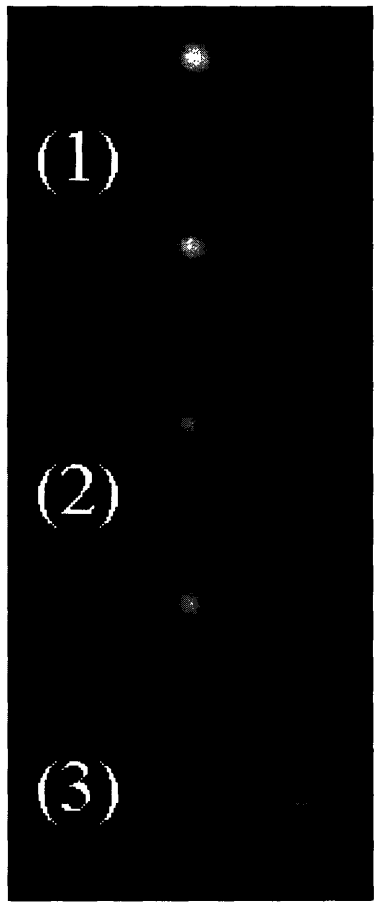

Figure 4-11: Pattern size modulation by voltage

Table 4.1 shows the applied MEMS voltage, shutter opening and pixel size for each condition for a second MEMS shutter. The voltage to close the shutter is higher than in the Figure 4-10 and Figure 4-11 examples due to the difference in MEMS processing. For all three voltages, there is a 15 μm broadening from the given geometry, so the pattern sizes are 15 μm wider than the shutter opening size. Figure 4-11 and Table 4.1 demonstrate well that modulation of pattern sizes is possible by controlling applied MEMS bias.

	MEMS voltage	Shutter opening	Pattern size
(1)	0V	33 μm	48 μm
(2)	30V	22 μm	37 μm
(3)	45V	14 μm	28 μm

Table 4.1: Relation between shutter opening and pixel size as a function of voltage applied over the MEMS

Material	Melting point (°C)	Resistivity ($\mu\Omega$·cm)	Density (g/cm^3)	Temperature at vaporization pressure (°C)			Crucible material
				10^{-6} torr	10^{-5} torr	10^{-4} torr	
Silver	961	1.6	10.49	847	958	1105	Molibdenum
Gold	1062	2.2	19.32	807	947	1132	Alumina

Table 4.2: Material properties of silver and gold

4.3 Deposition of a Metal, Ag

In order to deposit metal patterns, we need to increase the source temperature by several hundred degrees as it is seen in Table 4.2. This requirement raises new challenges such as minimization of heat flow to the substrate. It is important to prevent destruction of pre-patterned organic materials or permanent deformation of the substrate by heat flow. So, we increased the spacing between substrate and the source for metal deposition and we selected silver deposition because silver is frequently used as electrode in OLEDs and it has a good electrical conductivity.

By keeping the printer head stationary for certain time and then moving it to next position, we deposited dotted silver line as shown in Figure 4-12. The differing spacing between pixels and curved trace was not expected, indicating a problem in the deposition.

Instead of discontinuous motion, we modified the manipulator moition by putting coordinates for an oval and moving the manipulator very slowly to make a well defined metal line. Figure 4-13 is the result of oval deposition. The oval at right is programmed shape of pattern and the left pattern is the actual printed line. It is noted that the starting point and the end point do not match.

Two printed lines that were programmed as parallel straight lines were also not

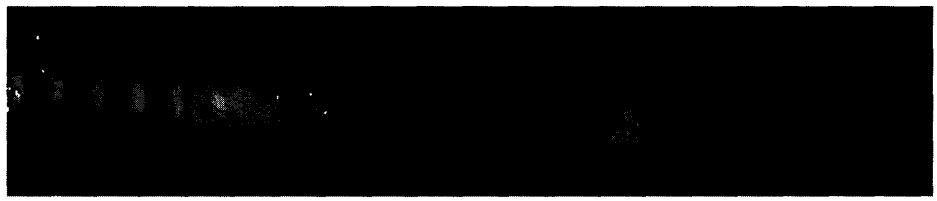

Figure 4-12: Silver line: the total travel distance of the substrate is 500 μm, and the continuous part is $\sim$0.3 mm.

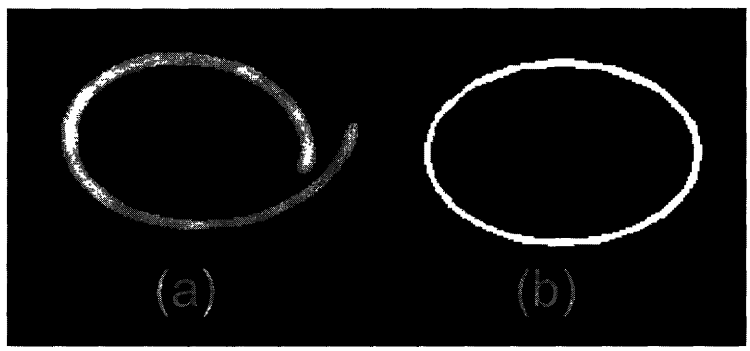

Figure 4-13: Printed oval (a) actual pattern (b) original design

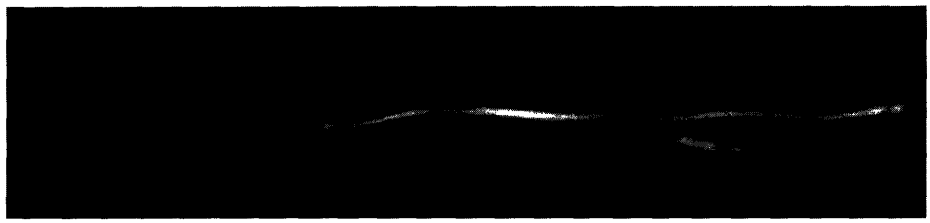

Figure 4-14: Two Silver lines

straight nor parallel as Figure 4-14 shows with the spacing between them changing from 100 μm to 300 μm.

Thermal expansion of the print head assembly was then, considered as a possible reason for unexpected patterns. Because the deposition temperature of silver is typically over 1100 °C, thermal radiation can result in expansion of assembly parts which hold the MEMS shutter. Thermal expansion coefficient of Stainless steel (200 mm long) and teflon (PTFE: poly-Tetrafluoroethylene) (50 mm long) that are used in the assembly parts are 1.5×10^{-5} mm/mm°C, 9.4×10^{-5} mm/mm°C, respectively. Thus, if the temperature of the assembly parts is 100°C, thermal expansion of stainless steel and teflon is on the order of 300 μm and 500 μm, respectively. These are significantly large expansion values compared to the print accuracy we are interested in. We measured the stainless steel holder temperature to be 60 °C when the crucible is cooled down to 150 °C. Thus, at deposition temperature the temperature of assembly blocks will be higher than 100 °C. Thermal expansion effect is very pronounced when printing letters. Figure 4-15 shows the optical microscope images of printed silver lines spelling the laboratory acronym. Figure 4-15 (d) shows the original design pattern. In the first deposition, Figure 4-15 (a), even though we can recognize letters, the parallel and vertical alignment are not retained. Especially for letters "O", the starting point and the end point do not match. These effects result from thermal expansions during deposition processes. If the thermal radiation from the crucible is reduced by inserting a metal heat shield between the crucible and the substrate, the thermal expansion effect reduces noticeably. As shown in Figure 4-15 (b), the "L" and "E" printed letters look similar to the original patterns, but the starting point and the end

point of "O" are still not coincident. When an additional shield is inserted, the thermal radiation effects are further reduced, and the actual printed patterns are almost identical to the original design as shown in Figure 4-15 (c). These examples shows the importance of thermal issues in metal printing. Generally, it is better to put the source far away from the substrate to reduce broadening of patterns, however, then material efficiency is low. If we want to have high material efficiency with keeping minimum broadening, the distance between the substrate and the aperture should be minimum and the distance between the aperture and the source should be small as it will be discussed in the next chapter. However, as the source gets closer, the thermal radiation can: (1) damage organic films on the substrate (2) cause thermal expansion of printer resulting in reduced print resolution. Thus, effective thermal shielding is necessary for optimized performance.

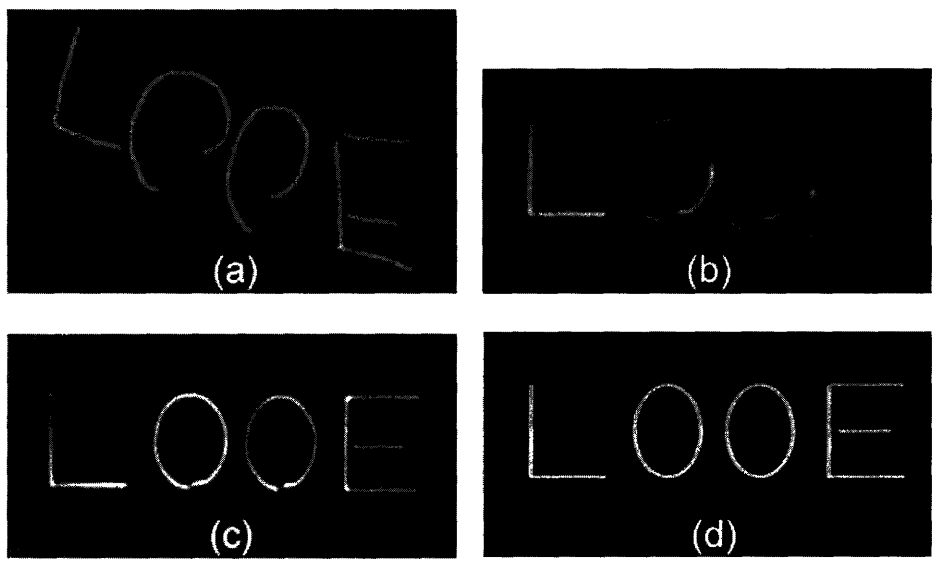

Figure 4-15: Optical microscope images of printed metal patterns: (a) without metal shielding layer (b) one metal shielding layer (c) two metal shielding layers (d) original design pattern

It has been shown that printing metal lines with arbitrary shapes is possible from the demonstration in Figure 4-15. Figure 4-16 shows a metal line with four metal pads for 4 point probe measurement. The line is approximately 5 mm long and the

thickness of line is 60 $\AA$ by Tencor P10 Profiler. The metal pads are silver film deposited using a shadow mask and the pad thickness is approximately 1200 $\AA$.

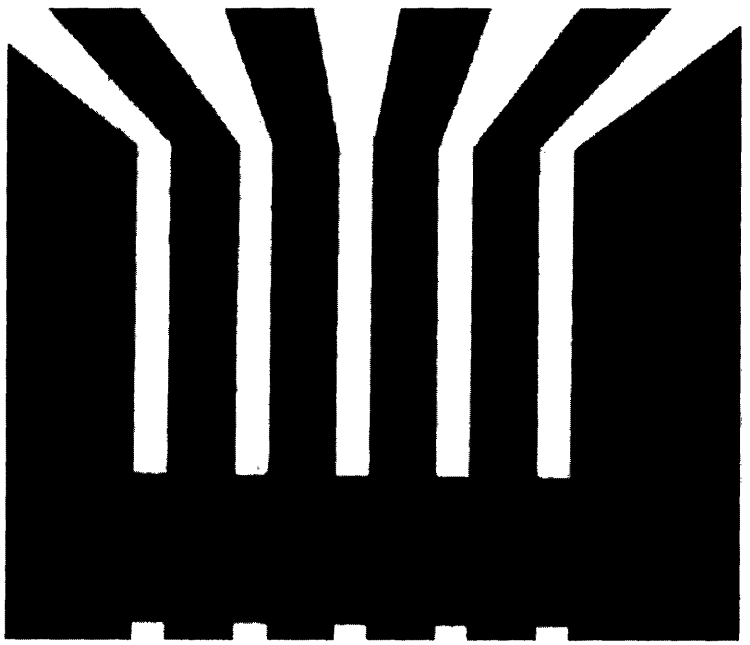

Figure 4-16: Metal line for resistivity measurement

Figure 4-17 shows the atomic force microscope (AFM) images of silver line and silver pad. From Figure 4-17 (a), the silver line is not a continuous film and is composed of silver nanoparticles, while the silver pad has a continuous film with packed silver layers as shown in Figure 4-17 (b). It is thought that the silver line is not continuous because the thickness is too thin. In order to have an electrically conducting line, a thicker continuous silver line should be made.

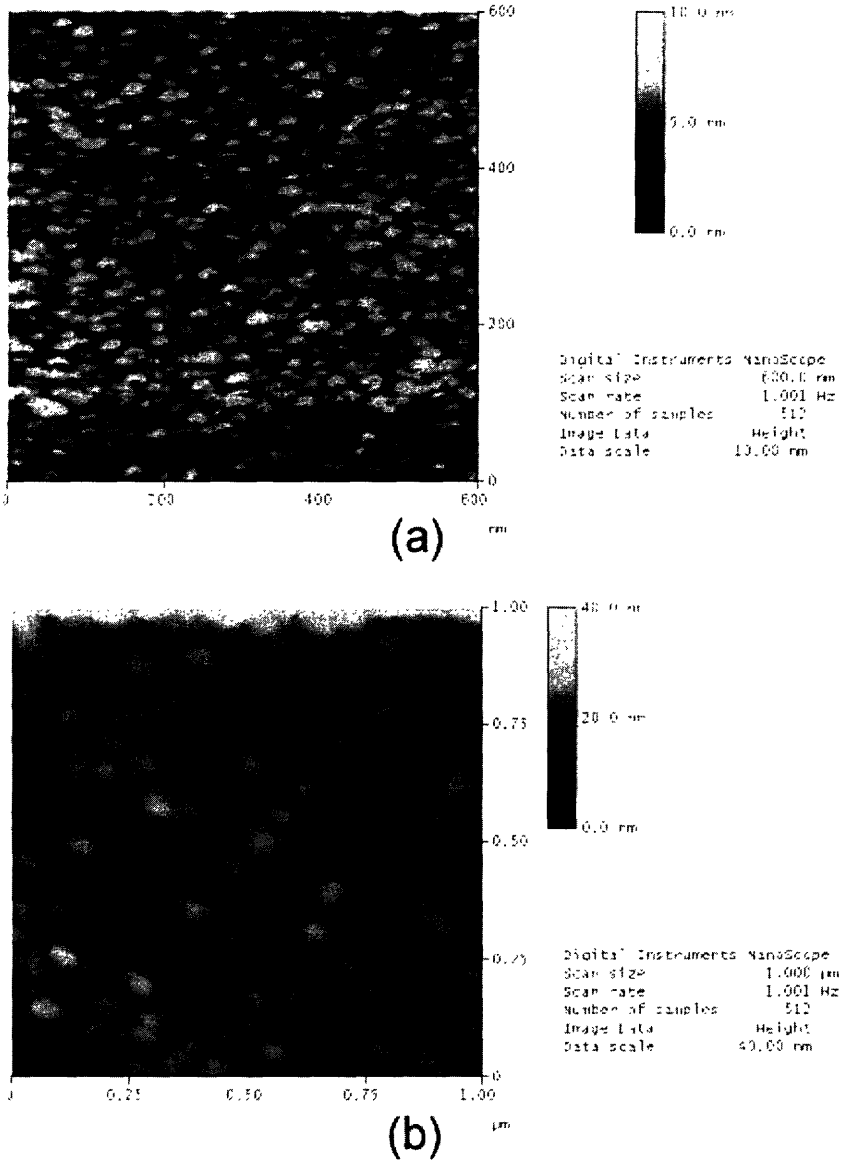

Figure 4-17: Atomic force microscope images of (a) silver line with the average grain size of 11.1 nm (b) silver pad with the average grain size of 40.5 nm. Digital Instrument Nanoscope IIIA is used in tapping mode.

Chapter 5

Influence of the System Geometry and Operating Conditions on the Reproduced Pattern

5.1 Broadening of Patterns

As shown in the previous chapter, the actual pattern sizes are bigger than the shutter opening size. The broadening effect varies depending on experimental setup. The main reason is a source emission geometry. Figure 5-1 shows the schematic picture of the experimental setup. h_1 is the distance between the substrate and the MEMS shutter and h_2 is the distance between the source and the MEMS shutter. The broadening effect is studied by changing one parameter (h_1 or h_2) while fixing the other.

5.1.1 Variation of Shutter to Substrate Distance

For better understanding of underlying principle, we did characterization of patterns using a fluorescence microscope and a WYKO optical profiler. Figure 5-2 shows the length of sides of a deposited square pixel as a function of distance between the substrate and the shutter (h_1 of Figure 5-1). The chamber pressure was 1×10^{-6} Torr.

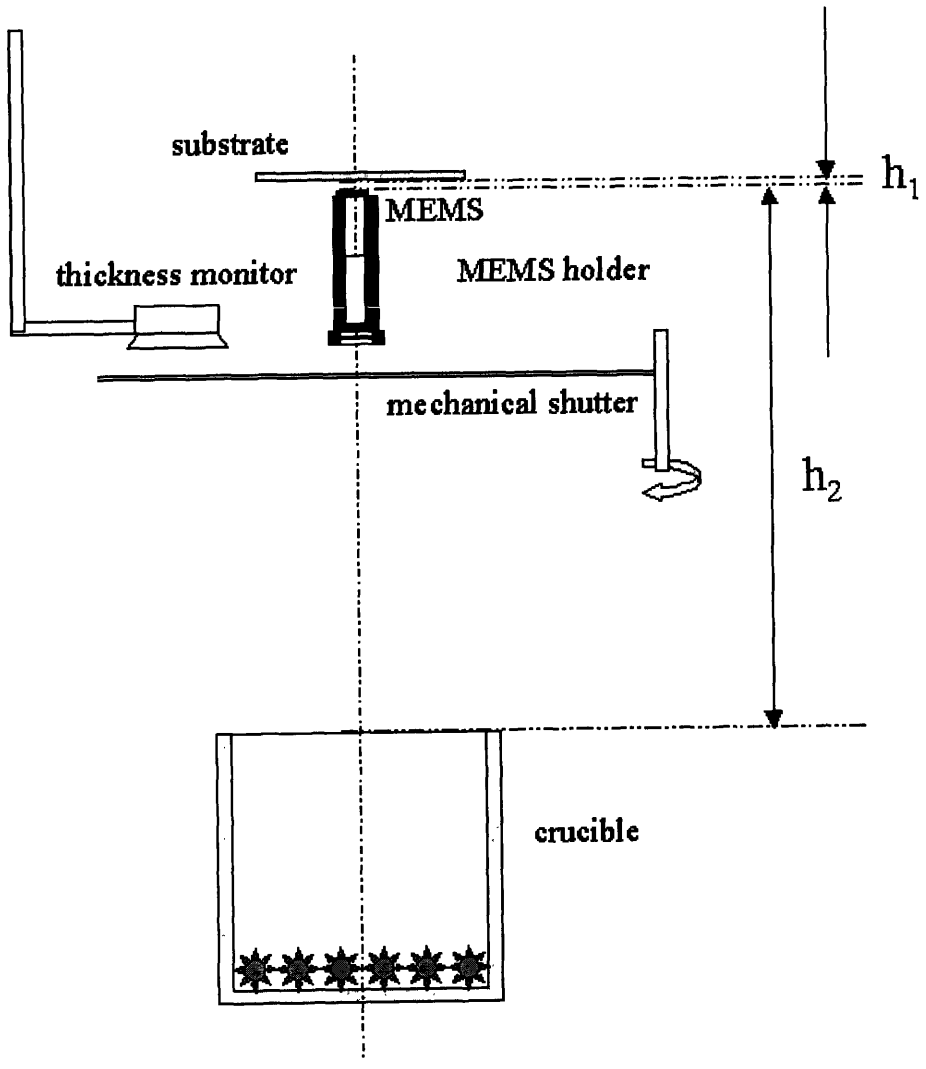

Figure 5-1: Source emission geometry

In this experiment, Silicon substrate is used which allowed us to check the substrate to MEMS shutter distance by measuring resistance between the Silicon substrate and the metal contact of the MEMS shutter. As the spacing increases, the feature size broadens significantly and it becomes twice of the original size if the distance between the aperture and the substrate is 0.6 mm.

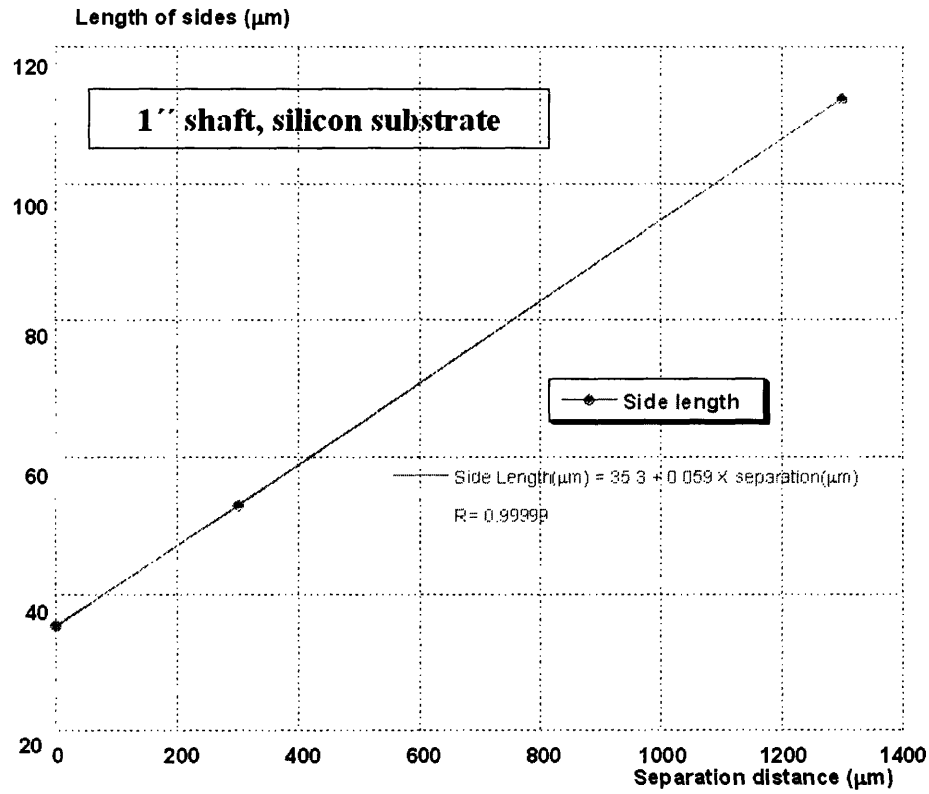

Figure 5-2: Broadening of pattern by varying the distance between the aperture and the substrate

Broadening of pattern occurs because the molecules travel following line of sight from the source to the opening in the MEMS shutter as shown in Figure 5-3. The mean free path of the molecules is longer than the chamber dimension at the pressure of 10^{-6} Torr. Thus, scattering events are negligible. From this analysis, it is desirable to have minimal distance for better definition. In Figure 5-2, it is also noted that the measured data fits well into a linear relation. The constant slope at different spacings indicates that the vibration effect in this system is small compared with the

printed geometry. At h_1=0, there is no broadening due to vibration effects because the MEMS shutter is in hard contact with the substrate. If there was a significant broadening due to vibration, the fit would not match the data without vibration. The slope of 0.06 is from a geometry of the experimental setup. This slope can be different if other dimensions are selected to make components in the experimental setup.

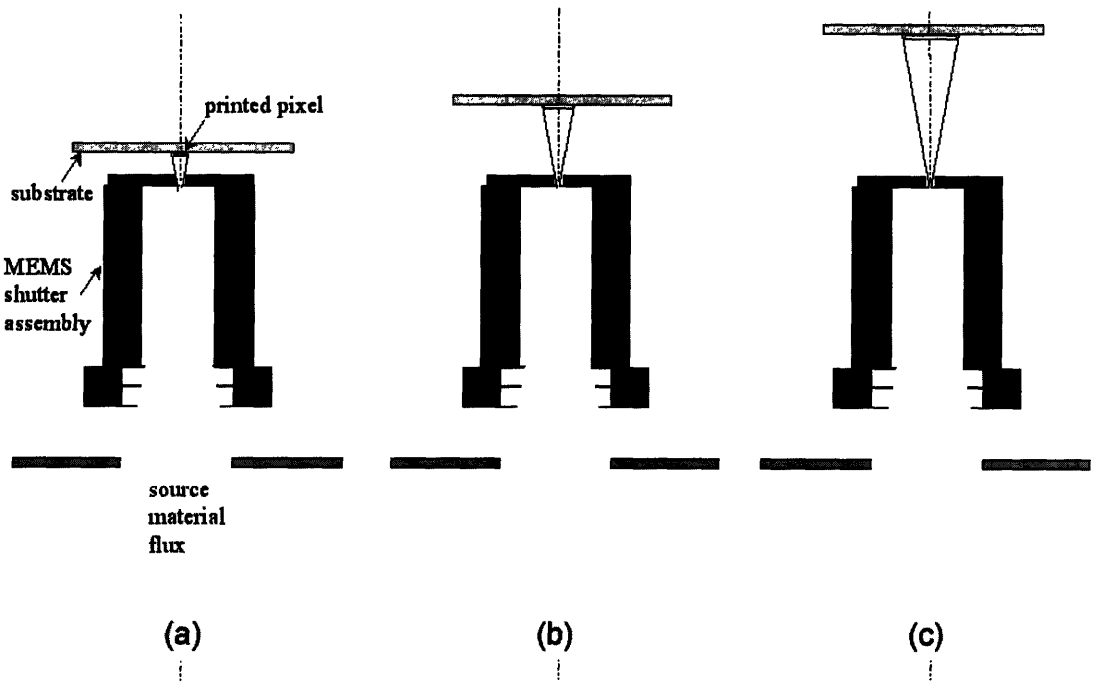

Figure 5-3: Broadening by geometry effect: the distance between the substrate and the MEMS shutter increases from (a) through (c)

Ideally, the pattern definition will be best if the substrate is always in contact with the MEMS shutter. However, the substrate should move in order to make patterns. So, it can not be in contact with the MEMS shutter all the time.

5.1.2 Variation of Source to Aperture Distance

We can also consider the case when the the spacing between the substrate and the aperture (h_1) is fixed and the distance between the source and the aperture (h_2) changes. In this case, the effect is different from the previous variation as it is

shown in Figure 5-4. As the source to the MEMS shutter distance increases from (a) through (c) in Figure 5-4, the broadening effect reduces but the material flux (number of molecules arriving at the substrate per unit area per unit time) decreases. Because the deposition flux decreases by $1/d^2$ (d=h_1+h_2: distance between a source and a substrate), less materials are deposited to a substrate while we get better definition.[45] For our geometry, the pattern broadening effect due to change in h_2 is not pronounced. Thus, if h_2 is small, it is possible to reduce h_1 for better deposition efficiency. However, for high temperature deposition as in case of metals, the thermal radiation can significantly influence the morphology of the printed patterns because thermal radiation increases as h_2 decreases. The effects of thermal radiation is described in Chapter 4.

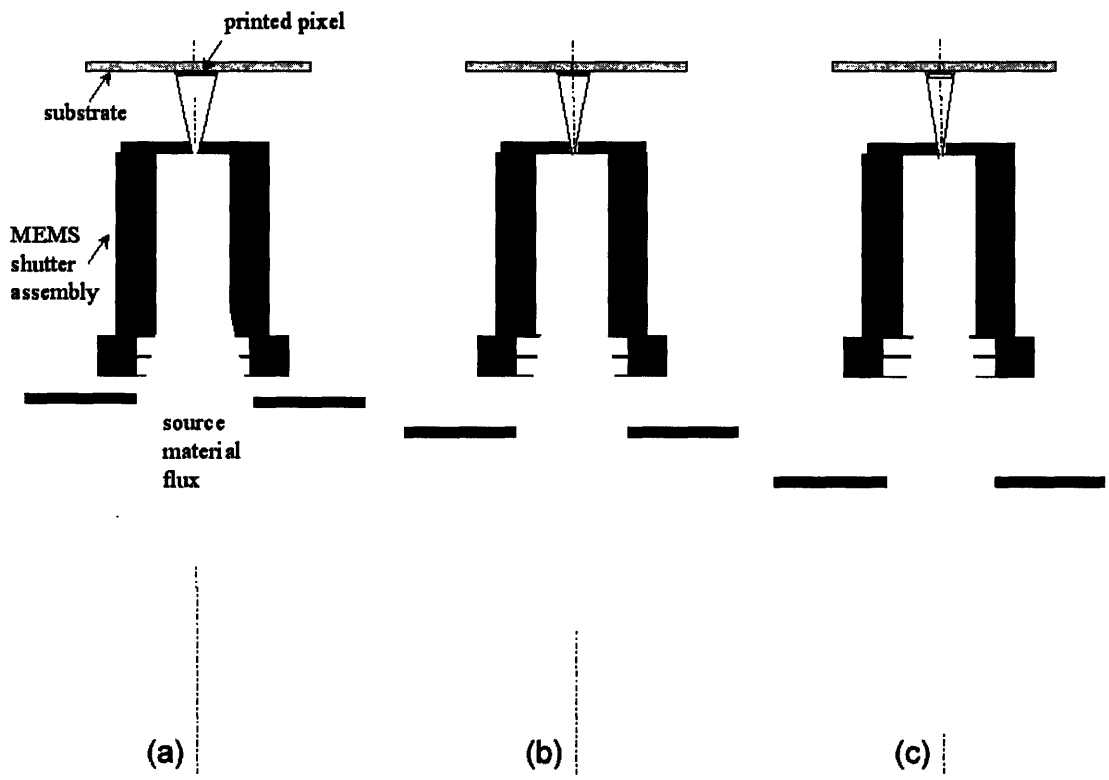

Figure 5-4: Effect of varying source to aperture distance (h_2): h_2 increases from (a) through (c)

From the analysis of variation of h_1 and h_2, we can reach following conclusions:

1. It is desirable to minimize the substrate to the shutter distance (h_1).

2. There is a trade off for varying the source to the shutter distance (h_2).

3. For a high temperature deposition, thermal radiation effects should be considered to decide the source to the shutter distance (h_2).

5.2 MEMS Clogging Issue

In the experimental setup of the molecular jet printer, there is no heating element for the MEMS shutter. Thus, evaporated materials can adsorb on the wall of the shutter which can result in clogging of the opening. There is a similar issue in inkjet printers as it is mentioned in 2.1.3. In inkjet printers, periodic printer head cleaning is performed to solve this problem. Figure 5-5 (a) shows the initial fluorescence image of the opening in the MEMS shutter taken after depositions and Figure 5-5 (b) shows the image of the same part after one month. Initially, some Alq_3 was deposited on the wall of the aperture as it is confirmed by green light of Alq_3 fluorescence. One month after taking the image (a), we could not find materials patterns on substrates even though same experiments were done five times. Another picture was taken for the same shutter as shown in Figure 5-5 (b). Meanwhile, experiments were done everyday and typically total 5 μm material was deposited in one experiment. The images shows that the shutter is closed and Alq_3 is deposited on the cover of the shutter.

In order to remove materials from the aperture, we soaked the shutter in chloroform and acetone for 5 minutes each and took pictures under a fluorescence microscope. Figure 5-6 (a) shows that materials are removed but the shutter opening is reduced. From Figure 5-6 (b), it is clear that the shutter is half open during solvent cleaning process. The main problem we have with the MEMS shutter is stiction: some of the suspended structures are stuck to the substrate after solvent cleaning. There is a 3 μm gap between the suspended structure and the substrate, but surface tension due to the presence of a liquid is enough to bring the two surfaces together. When the shutter is stuck to the substrate, it is usually not aligned with its initial position, and

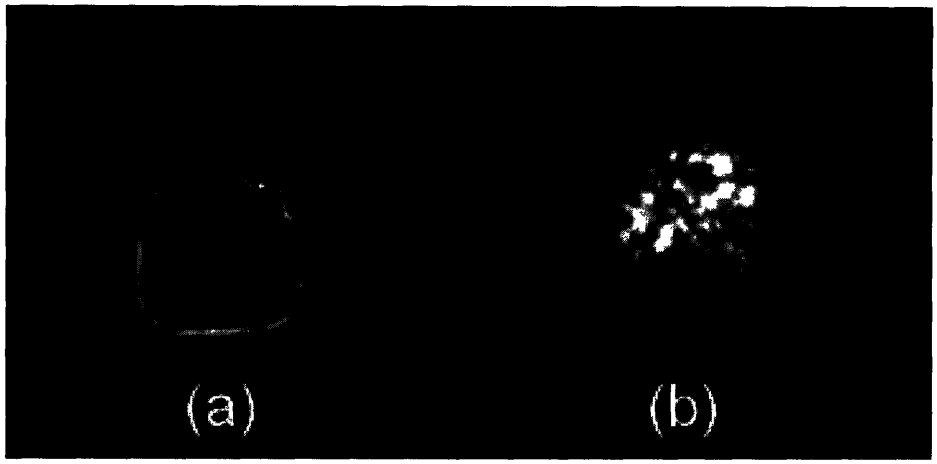

Figure 5-5: Fluorescence microscope images of shutter (a) initial image after depositions (b) one month after (a)

the hole is partly closed. If the surface under the shutter was not very clean after the fabrication, it could also happens that the shutter sticks to it after fabrication, while it is being used. An alternative solvent-free cleaning procedure would involve heating the MEMS shutter at a printer service station to evaporate the deposited material. This solvent-free cleaning process would likely prolong the useful MEMS life.

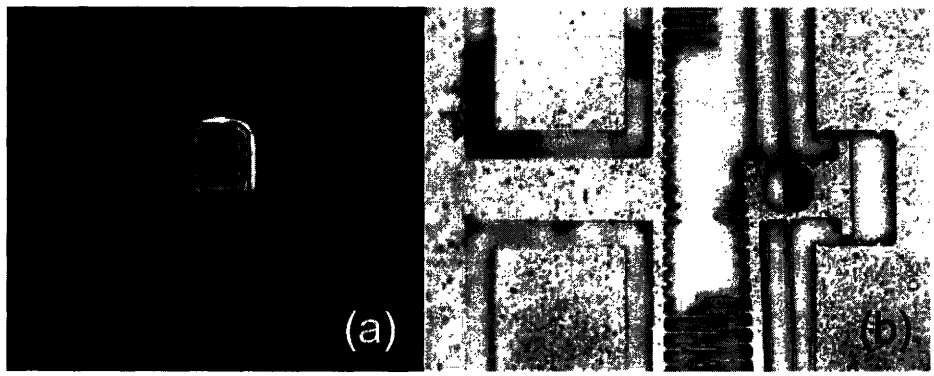

Figure 5-6: Microscope images after solvent cleaning (a) shutter under fluorescence microscope (b) part of the MEMS chip under optical microscope

Besides cleaning procedures, it is possible to modify the opening shape as it is shown is Figure 5-7. Figure 5-7 (a) shows when the shutter is partially open. If the

pattern size is reduced due to clogging or other reasons, we can increase the opening size as it is shown in Figure 5-7 (b). This diamond shape opening can give us control of the opening size.

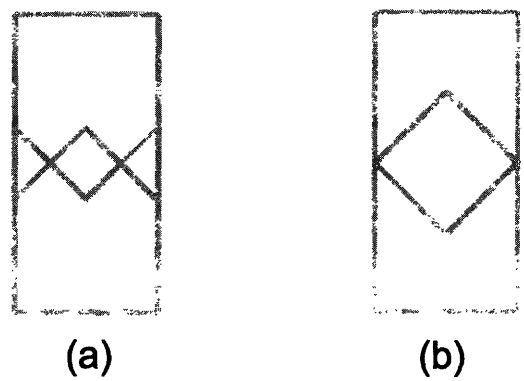

Figure 5-7: Modification of shutter opening shape

5.3 Numerical Analysis for Different Pressures

Can we use the molecular jet printer in ambient, as a typical inkjet printer? The mean free path of molecules decreases as the pressure of the background increases. We can expect that the increased scattering of molecules will influence the material patterns. As a next step, numerical calculation was done based on 2D collision model. The assumptions and parameters that are used in this simulations are as below:

1. The background atmosphere of the chamber is nitrogen (molecular weight of N_2= 28 g/mol) and the nitrogen molecules undergo random walk.

2. Alq_3 (Molecular weight = 465.5 g/mol, Diameter: 1 nm) is evaporated at various pressures and initial velocity of Alq_3 molecules is assumed constant in one direction.

3. Collision angle is randomly chosen.

4. 100,000 molecules are used for calculation.

5. The opening of the MEMS is 50 μm and the substrate to the MEMS spacing is 100 μm.

6. The mean free path of the molecules = $\frac{RT}{\sqrt{2}\pi d^2 N_A P}$ (R: gas constant, T: temperature, d: diameter of molecules, N_A: Avogadro's number, P: pressure)

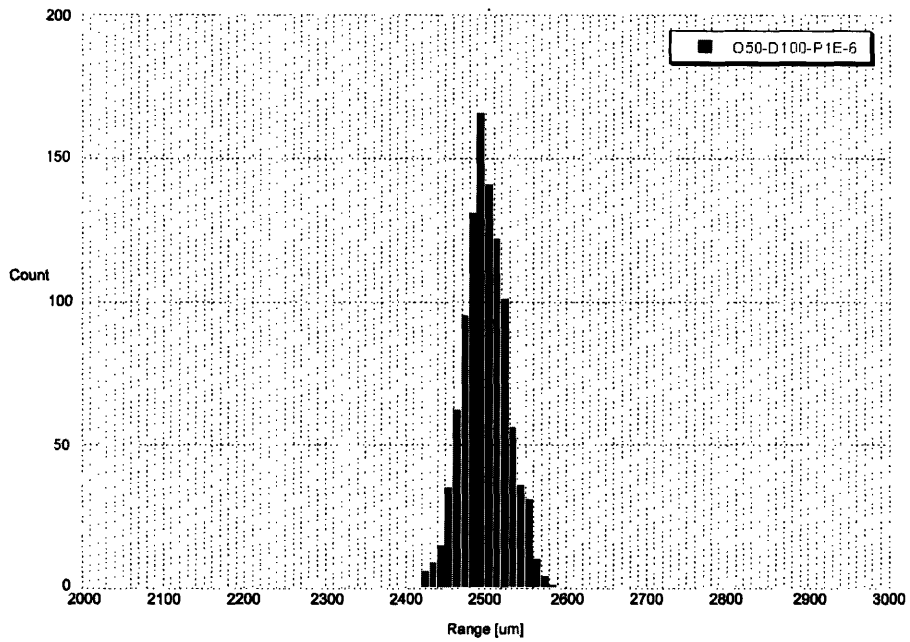

Figure 5-8: Calculated material pattern at 10^{-6} Torr

Figure 5-8 shows the calculated result of the expected molecule distribution when the background pressure is 10^{-6} torr. If we take the full width at half maximum (FWHM) of the graph, the simulation result matches with an experimental result within 50 % error. Considering the simplifications of the calculation, the simulation result gives a good sense of magnitude. Thus, similar calculations are done for different pressures. Figure 5-9 to Figure 5-15 show the change of material distribution in the range of 10^{-7} to 1 torr.

From the simulation results, the full width at half maximum of the printed pixel does not change significantly up to 10^{-2} Torr, though pixel thickness gets smaller due to the reduced flux at high background pressures. The mean free path (MFP) at

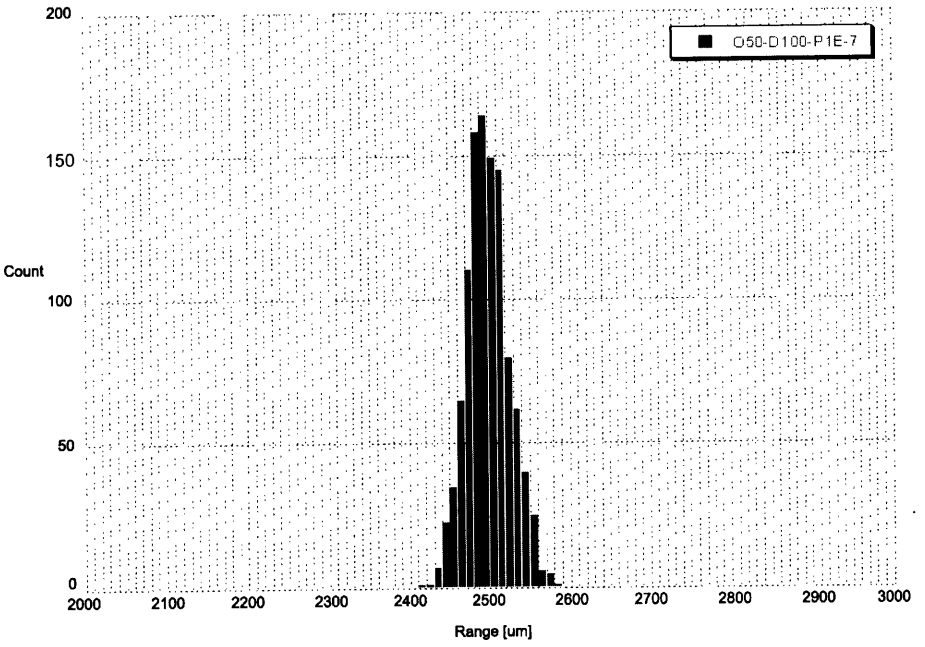

Figure 5-9: Calculated material pattern at 10^{-7} Torr

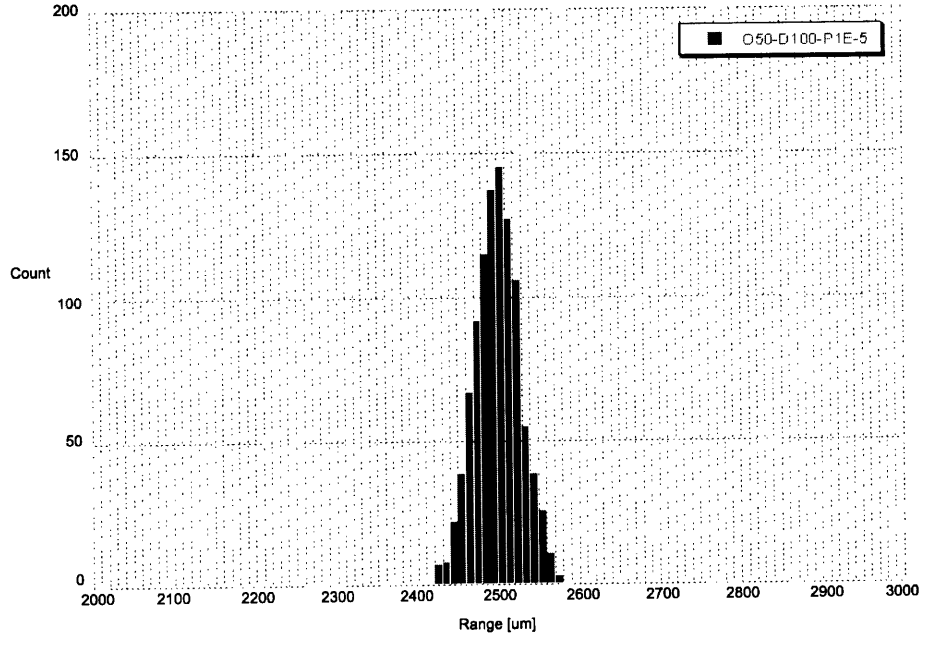

Figure 5-10: Calculated material pattern at 10^{-5} Torr

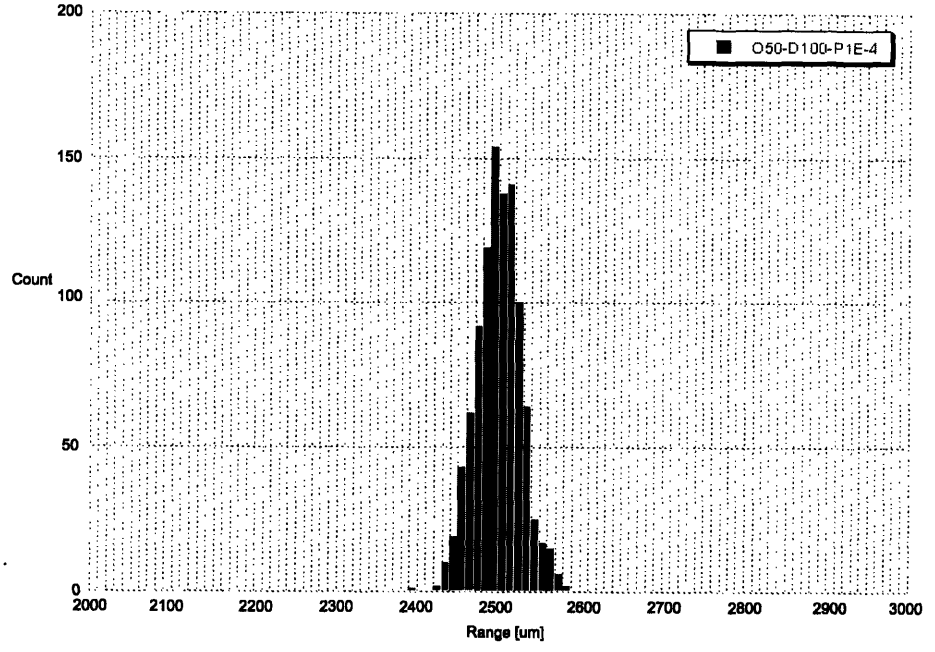

Figure 5-11: Calculated material pattern at 10^{-4} Torr

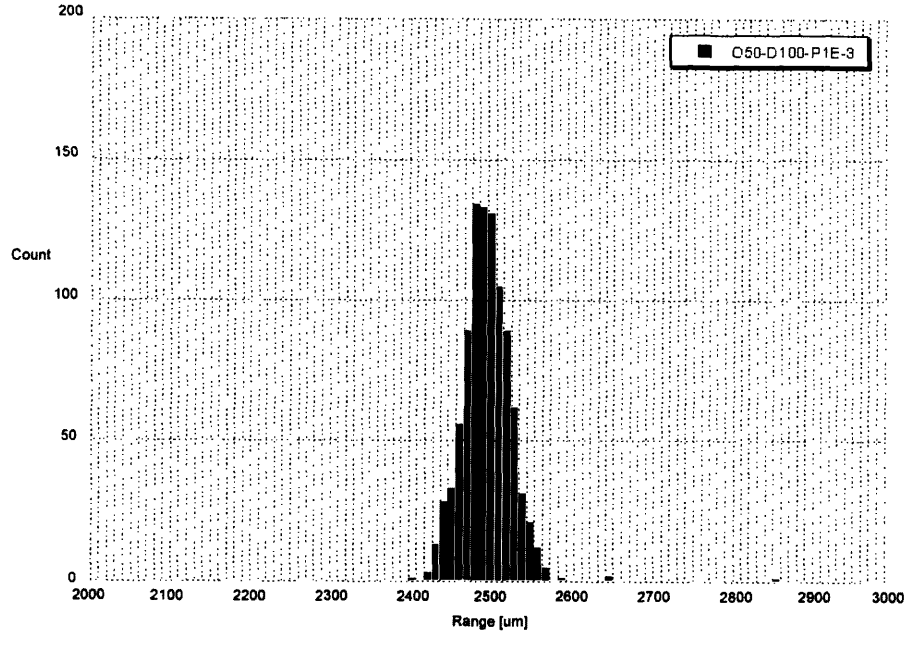

Figure 5-12: Calculated material pattern at 10^{-3} Torr

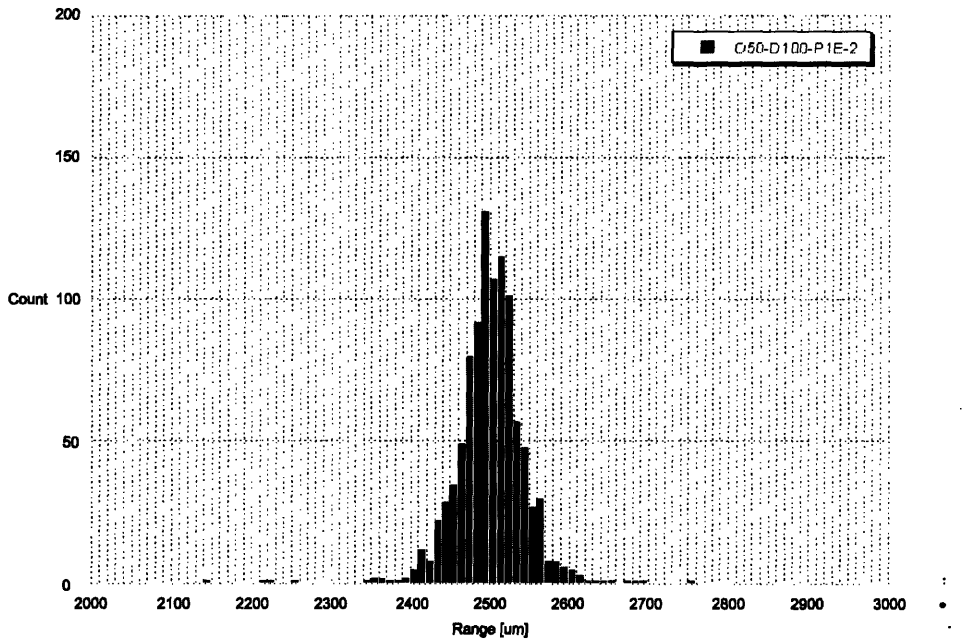

Figure 5-13: Calculated material pattern at 10^{-2} Torr

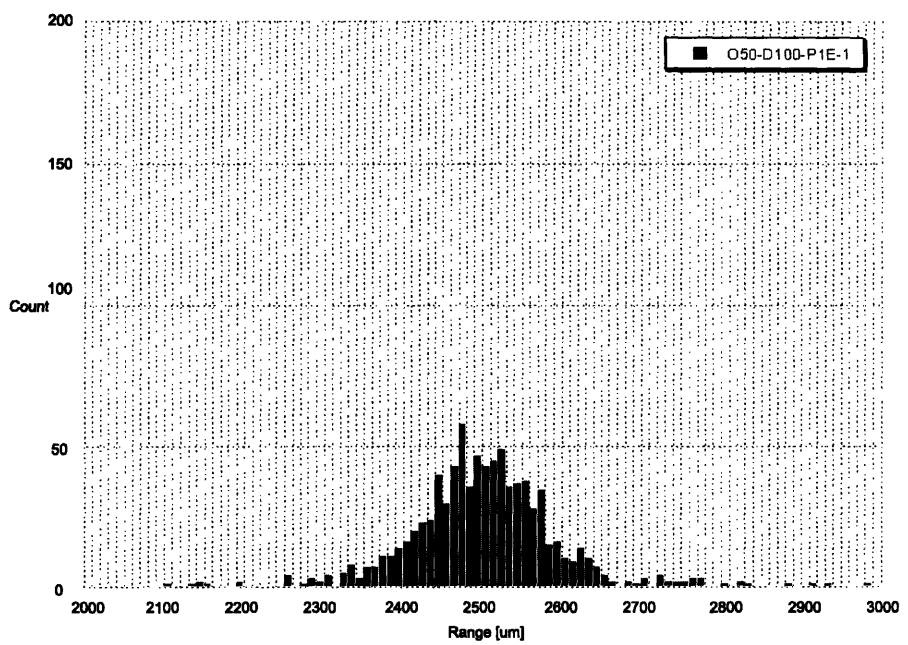

Figure 5-14: Calculated material pattern at 10^{-1} Torr

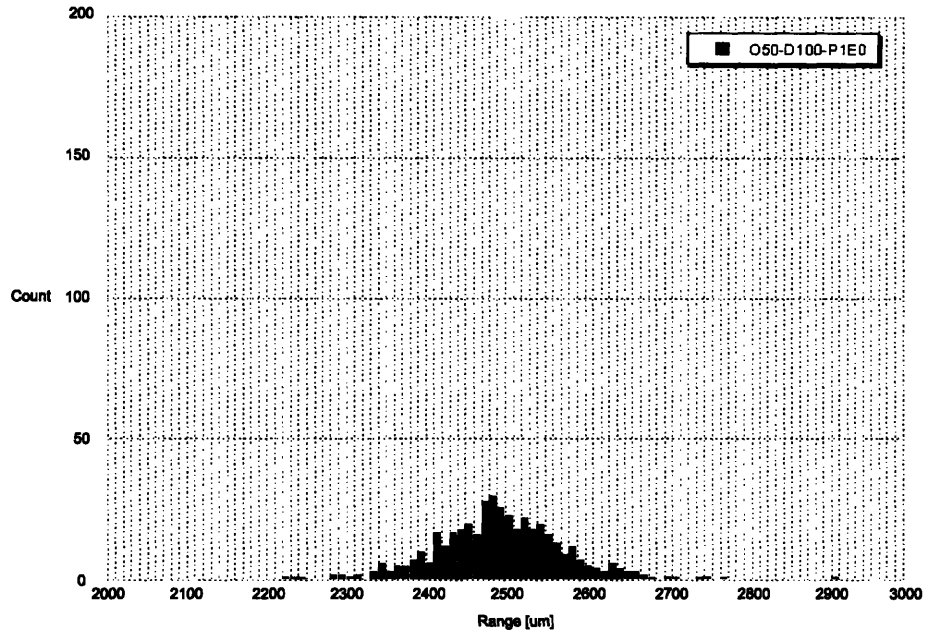

Figure 5-15: Calculated material pattern at 1 Torr

10^{-2} Torr is longer than 100 μm which is the spacing between the substrate and the MEMS shutter. Thus, most of molecules that reached the shutter can be adsorbed on a substrate without scattering. When the MFP is less than the MEMS to the substrate distance, the molecules experience many scattering events before reaching to the substrate. The number of molecules that can reach the substrate is reduced as the background pressure increases. Thus, the height of the pixel decreases as the flux decreases. If MFP is less than the substrate to the MEMS shutter distance, then molecules scatter many times before reaching the substrate and the pattern gets noticeably broad as the pressure is higher than 10^{-2} Torr.

From the pressure study, three regimes can be considered as shown in Figure 5-16. Based on the experimental setup of the system, printing at pressures lower than 10^{-2} Torr can give us well-defined patterns. For higher pressures, the source to the MEMS aperture distance has to be reduced to preserve the pattern resolution.

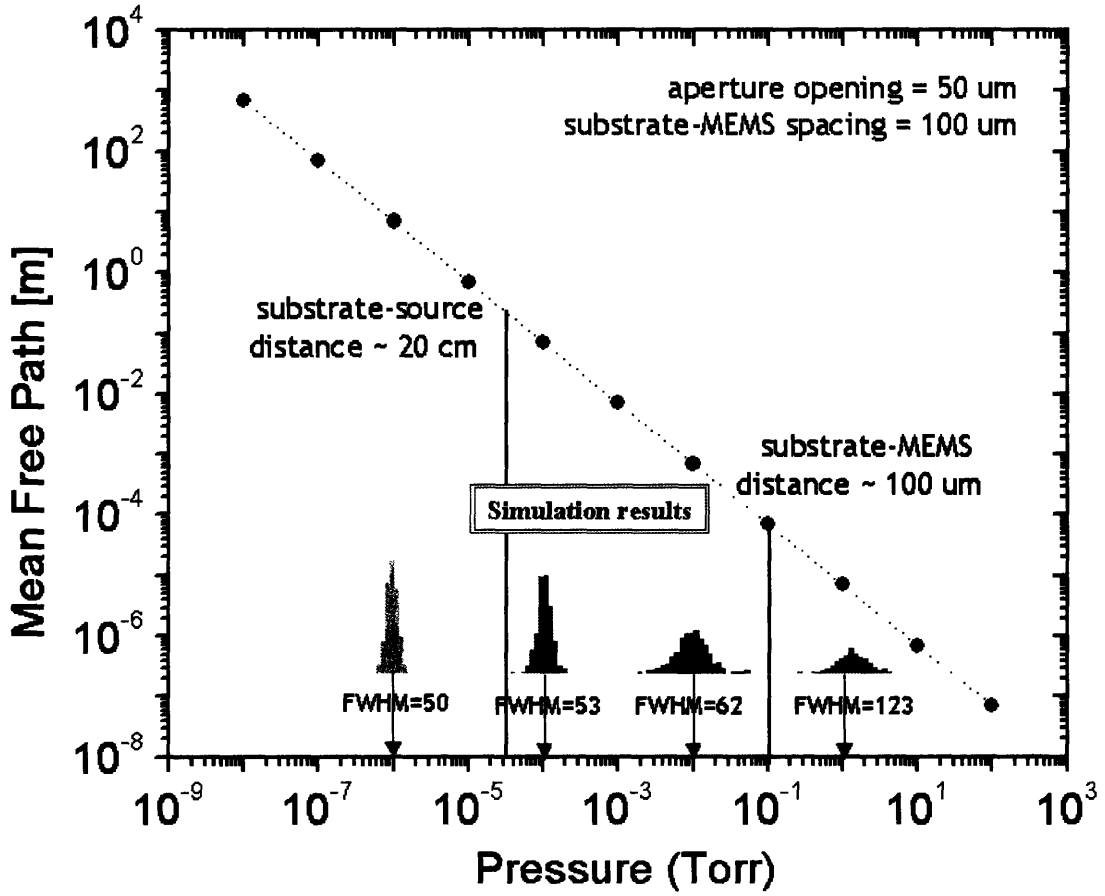

Figure 5-16: Pressure vs mean free path

Chapter 6

Future Work

6.1 Challenges of Molecular Jet Printer and Possible Solutions

6.1.1 Short Mean Free Path at 1 atm

The ultimate goal of the molecular jet printer is printing in ambient environment. As shown in the numerical calculation, the mean free path of the molecules is less than 1 μm at 1 atm. Without expensive positioning system, it is hardly achievable to control the spacing within the 1 μm accuracy. One possible solution is to use a local vacuum. Considering the size of laser printers, it is feasible to make a molecular jet printer with a pumping system in a comparable volume. Further study needs to be done to verify the numerical calculations by printing patterns at various pressures.

6.1.2 Deformation or Re-evaporation of Materials by Thermal Radiation

It is shown in experimental results that thermal radiation can produce undesirable effects by thermal expansion of the shutter mounting parts. In addition, deformation or re-evaporation of materials by thermal radiation can be issues in multilayer device structures. It is typical in modern semiconductor devices to use multilayer films for

better performance. If we print metals on organic films, heat from high temperature source can decompose organic materials or re-evaporate them. Typically, the sublimation temperature of organic materials is in the range of 150-300 °C. Thus, thermal management is important. One solution is cooling of substrates. Another solution is to separate a heating zone from a material transfer zone. In Organic Vapor Phase Deposition (OVPD), carrier gases are used to transport source materials to a substrate.[46] Figure 6-1 shows the schematic diagram of the next generation molecular jet printer head. In this system, materials are fed into the heating zone by gravity and the porous stopper prevents metal powder deposition. Materials are sublimated in a heating zone by resistive heating and they transfer through the Teflon tube. Small heating of the material transfer zone can help reduce stiction of materials to the tube. Pulsed Ar gas can help transfer of material and prevent degradation of organic materials in ambient. The transferred materials are deposited through the MEMS shutter that is attached to the end of the printer head.

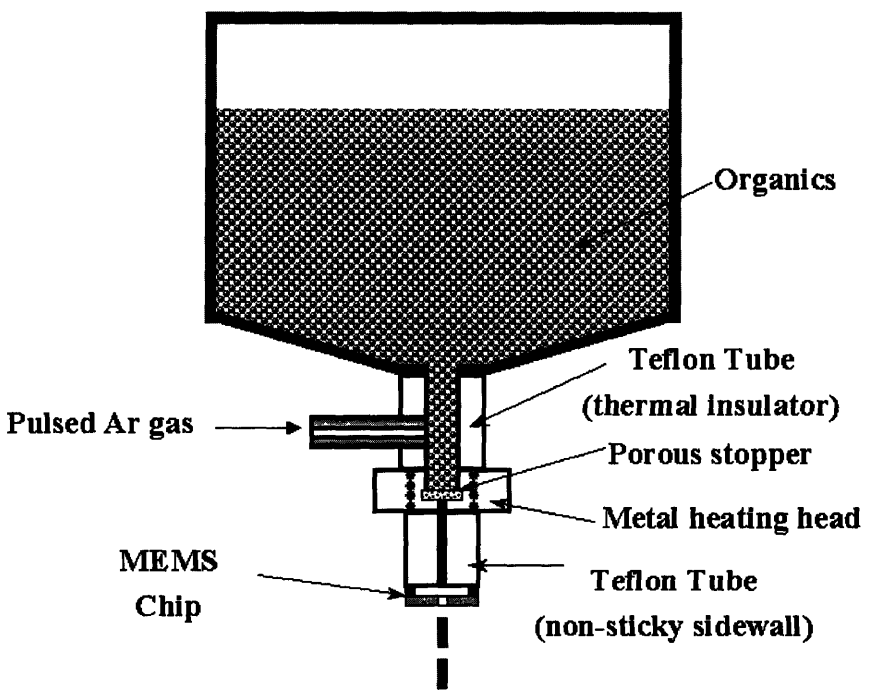

Figure 6-1: Schematic diagram of the next generation printer

6.1.3 Low Throughput Due to Limited Deposition Efficiency

An outstanding disadvantage of a typical evaporation system is a low throughput. For better uniformity, the distance between the source to the substrate is typically large. This limits the compactness of the system and requires high vacuum. Typically, 1 % of evaporated materials is deposited on to substrates and rest of materials deposited to the chamber wall. In molecular jet printer, the deposition efficiency (= the number of deposited molecules/the number of evaporated molecules) is higher than in a typical evaporation system because it is possible to reduce the source to substrate distance, without being limited by uniformity since each pixel is defined by the MEMS shutter. However, this distance can not be reduced to within a distance at which thermal radiation becomes important. One possible solution to overcome this limitation is to transfer materials from a separated heating zone as described in Figure 6-1. Another solution is to use multiple nozzles. In the current configuration, there is only one nozzle while the source diameter is 1 inch. By using multiple nozzels, we can increase the throughput. If we integrate 1000 nozzles next to each other and deposit 1000 $\AA$ thick pixels at an evaporation rate of 100 $\AA$/s, we can print a million pixels in less than 3 hours.

6.2 Organic Crystal Formation

Mascaro et al. reported that in certain circumstance, solvents may assist the formation of well-ordered films. Figure 6-2 shows the fluorescence and scanning electron micrographs of organic crystals (Alq_3) prepared by solvent annealing. They observed that solvent annealing and grating helped form high aspect ratio organic crystal on substrates.[3]

We also observed that Alq_3 crystals with needle shapes form on a glass substrate when the deposition is done at 0.05 Torr. Figure 6-3 shows a fluorescent microscope image of Alq_3 crystals on a glass substrate. The surface plot of the sample by AFM is shown in Figure 6-4. Crystal formation also occurs at high vacuum as shown in Figure 6-5. If we zoom in the image, we can see clearly that crystals form to certain

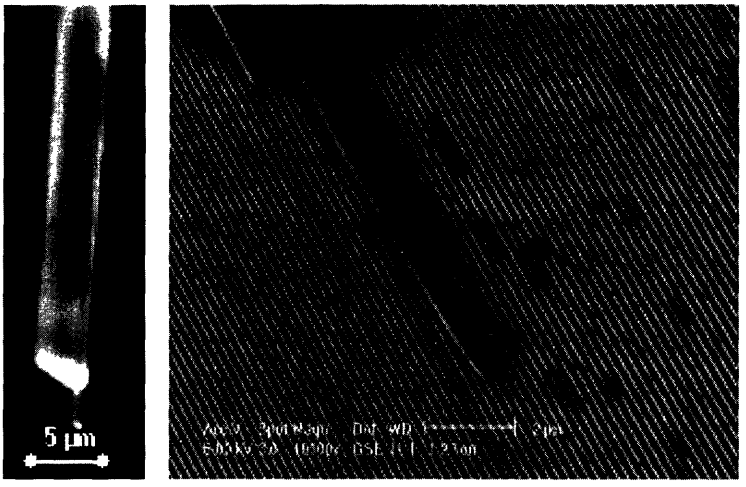

Figure 6-2: Fluorescence and scanning electron microscopy picture of organic crystal prepared by solvent annealing.[3]

orientations from the phase image of the crystal as shown in Figure 6-6 (b).

6.3 Controlled Doping

By using an effusion cell, it is possible to do precise control of a growth rate because the effusion cell has a stable temperature control. With an effusion cell, it is possible to increase the growth rate over 100 $\AA$/s for organic materials and the minimum growth rate is 0.1 $\AA$/s which changes depending on the thickness monitor accuracy. Thus, controlled doping (i.e. deposition of mixtures with molecular ratios of at least 1:1000) can be done if there are multiple sources.

6.4 Integration with Conventional Inkjet

Molecular jet printer can print small molecule organic materials and metals. Ink jet printer can print solution-based materials. By integration with a conventional inkjet printer, we can have full materials capabilities with arbitrary pattern formation capabilities. Then we can print active devices such as OLED displays, organic field effect transistors (OFET) etc. as shown in Figure 6-7.

Figure 6-3: Fluorescent microscope image of Alq_3 crystals grown at 0.05 Torr

Figure 6-4: Surface profile of Alq_3 crystals by atomic force microscope

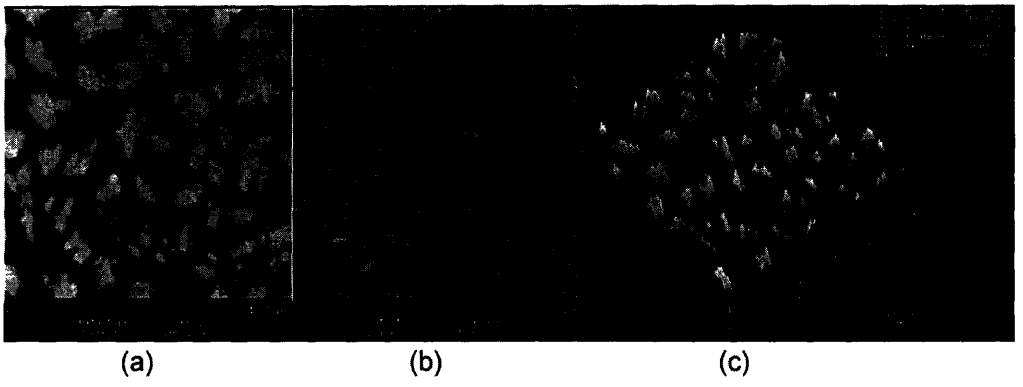

Figure 6-5: Atomic force microscope image of Alq_3 grown at 10^{-6} Torr (a) height image (b) phase image (c) surface image

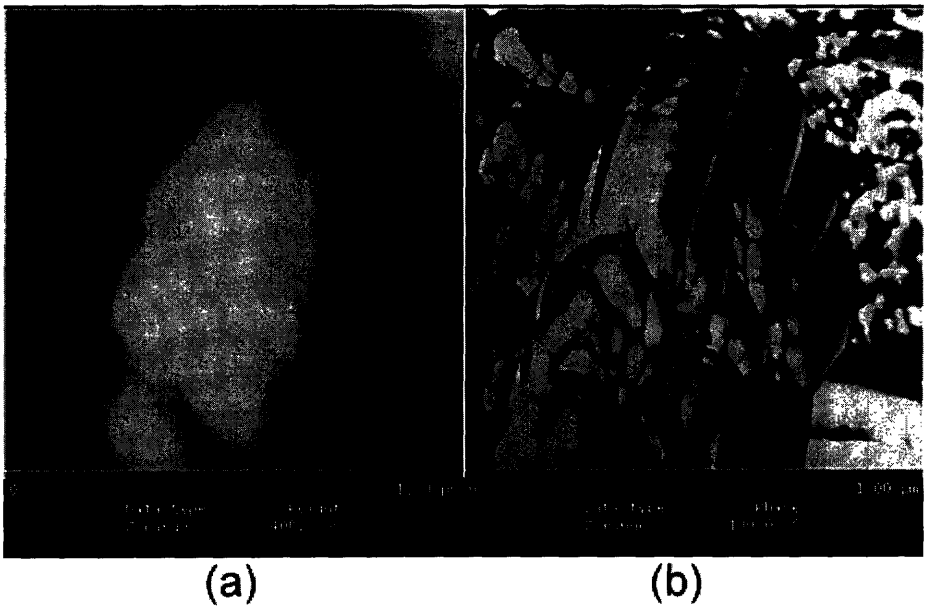

Figure 6-6: 1 μm by 1 μm scan of the Figure 6-4 (a) height image (b) phase image

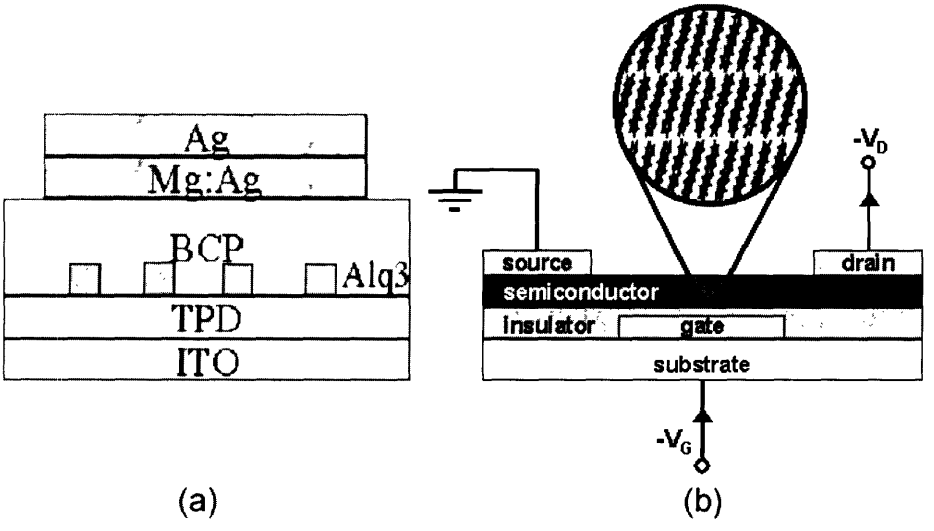

Figure 6-7: Structure of (a) OLED and (b) OFET

Chapter 7

Conclusion

The advantages of inkjet printing make it the ideal fabrication tool for the ubiquitous electronic technologies of the future. However, inkjet printing is currently limited to materials that can be processed in solution. We developed a novel micro-machined print head capable of expanding the capabilities of inkjet printing to metals and molecules that are not suited for solvent-based printing techniques. Deposition of metals is particularly desirable advantage of the printer. In this work, it is demonstrated:

- That we can make arbitrary organic and metal patterns by printing.
- That we can modulate the pixel size by changing a bias to the MEMS shutter.
- That we can have better resolution as the spacing between the substrate and the MEMS shutter is closer.
- That there is a trade-off between material efficiency and resolution as we change the distance between the MEMS shutter and the evaporation source.
- That effective thermal shielding is important for metal deposition.
- That clogging can be an issue because the MEMS shutter is at room temperature. We can clean the shutter or modify the design to solve this problem.

- That from numerical calculation, we can deposit 100 μm pixels by depositing at 0.01 Torr through a 50 μm aperture.

Part II

Development of Organic Memories

Chapter 8

Introduction

Organic electronics has attracted much attention due to the advantage of organic materials such as low cost processing, lightweight substrates, and mechanical flexibility. Several types of electronic and optoelectronic devices have been made using organic materials, but there is still a lack of progress in development of reliable organic electronic memories.

8.1 Demand for Low Cost High Performance Nonvolatile Memory

Conventional memories can be divided into two main categories: volatile memory (ex. random access memories (RAMs)), which lose stored information once the power supply is switched off, and nonvolatile memory (ex. hard disk, read-only memories (ROMs) etc.), which keep stored information also when the power supply is switched off. Nonvolatile memory market share has been continuously growing in the past few years, and further growth in the near future is foreseen, especially for Flash memories (in which a single cell can be electrically programmable and a large number of cells called a block, sector, or page are electrically erasable at the same time). Flash memories have an enhanced flexibility when compared to electrically programmable read-only memories (EPROMs), which are electrically programmable but erasable

via ultraviolet (UV) exposure. Electrically erasable and programmable read-only memories (EEPROMs), which are electrically erasable and programmable per single byte, are manufactured for specific applications only, since they use larger chip areas and, therefore, are more expensive.[47]

Buoyed by strong demand from cellular phone manufacturers, the flash memory market has grown rapidly. This growth trend is still strong, and it is expected to increase with the emergence of new demands such as digital TVs, personal digital assistants (PDAs), digital cameras, MP3 players, automotive uses, games, printers and multifunction cellular phones. According to the World Semiconductor Trade Statistics in 2001, the proportion of the overall semiconductor market represented by flash memories has grown from 2% in 1998 and earlier, to 3% in 1999, and 5.2% in 2000. Figure 8-1 shows the growth of the flash memory market in financial terms. The market in 1999 was $4,560.5 million, but in 2000, the value jumped 133.2% to $10,635.6 million. And, the market is projected to increase. The causes of the rapid growth between 1999 and 2000 were the strong growth of the cellular telephone market, digital consumer electronics, the emergence of new markets, such as networks, and a shift to high-capacity memories combined with a shortage of supply that led to higher prices.[48]

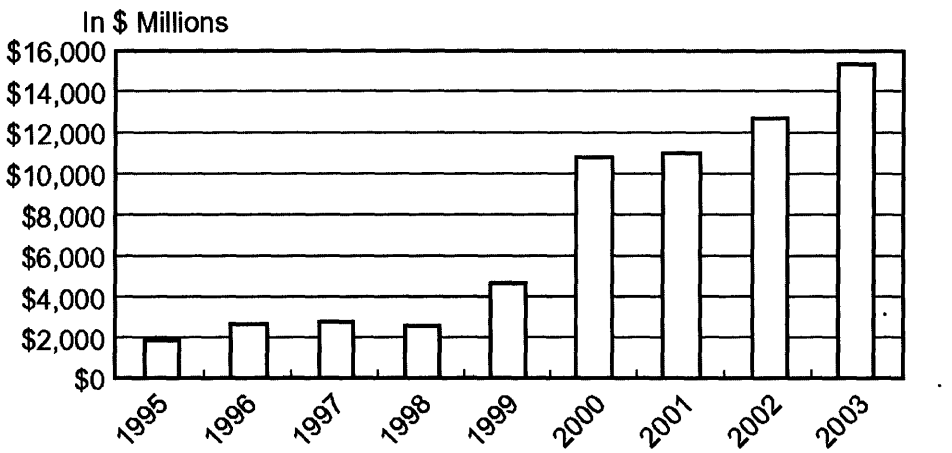

Figure 8-1: Flash memory market size

A significant fraction of the memory industry is manufacturing flash memory devices, which retain information when power is interrupted. Flash memory has a lower power consumption because it does not need continuously applied voltage, as in the case of a dynamic random access memory (DRAM) to maintain information.[49] As the density of memory devices increases, the manufacturing cost is increasing because of the increasing cost of the new equipment to reduce the minimum feature size. Furthermore, unsurmountable limitations to continued scaling are predicted to be imminent, facing demand for research on alternative non-volatile memory technologies such as ferroelectric memory,[49] nanocrystal memory,[50] molecular memory,[51] organic memory etc.[10] The motivation of this study is to develop a non-volatile memory based on organic materials that might be integrated into future organic integrated circuits.

8.2 Charge Conduction Mechanism

Weak van der Waals interactions between the molecules of an organic thin films results in low charge carrier mobility, which gives rise to space charge limited (SCL) conduction in these films. The SCL conduction model, as showed in Figure 8-2, is strongly dependent on the distribution of available electronic states within the film. Structural disorder in amorphous organic thin films can result in the presence of localized states which can trap and store charge in equilibrium, and can dominate the current-voltage (I-V) device characteristics because of a relatively low density of intrinsic free charge carriers.[52] [53] With trap states present, only a fraction of the charge injected can freely travel through the material as described in space charge limited conduction. Consequently, the effective mobility in trap-filled thin film is reduced by the factor Θ which is determined by the density and energy depth of traps and the sample temperature. If the trap density of the material is very large, the conduction is limited by carrier transport across trap states as in the case of trap-limited space charge conduction in Figure 8-2. For shallow traps of single energy, SCL mechanism results in the square law dependence of current on voltage, $I \propto V^2$.

For a large density of energy distributed traps, I$\propto V^m$ where m is typically a number in the range of 5 to 11.

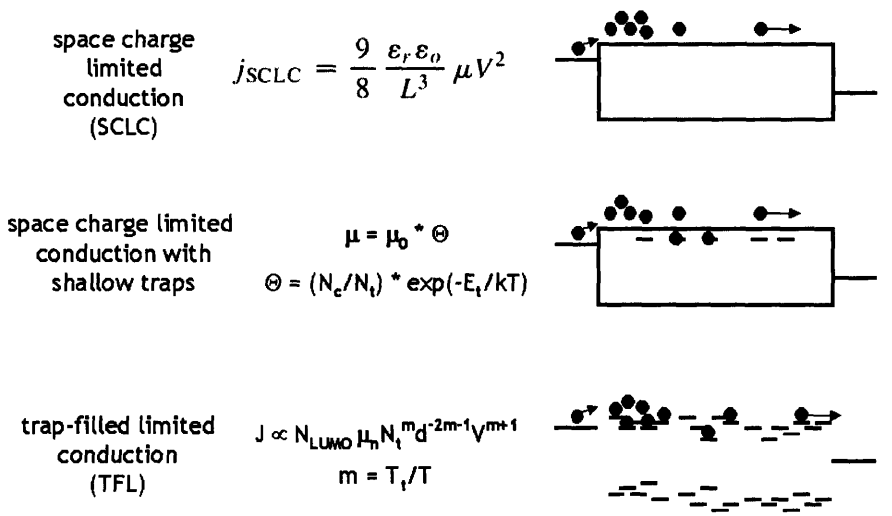

Figure 8-2: Conduction in Organic Thin Films (j = current density, μ = mobility, V = potential, L = thickness of film, N_c = effective density of conduction-band states at temperature T, N_t = trap density at energy E_t below the conduction band)

Due to the differences in the current dependence on voltage between the different regimes of conduction, by measuring I-V characteristics of organic thin films, we can characterize what is the main transport mechanism for a given biasing condition. Figure 8-3 shows typical I-V characteristic of low mobility semiconductor with a single trap level (a) and two distinct trap levels (b). Initially, the current flows by thermal carrier generation (1), and space charge conduction (2) but if there are shallow trap sites, the current is limited by trap-limited conduction (3). If voltage is high, then the trap sites can be all filled, and the mobility increases (4) similar to the case in the absence of trapping. If there are two trap levels, there are two trap filled limits as shown in Figure 8-3 (b) with voltages V_{TFL}^1 and V_{TFL}^2 indicating the critical voltage at which the trap levels are filled with charge carriers.

Developing and understanding of charge transport and trapping mechanisms is crucial for designing optimized electronic devices. It is evident that understanding the conduction mechanism by charge trapping and devising ways for controlling the

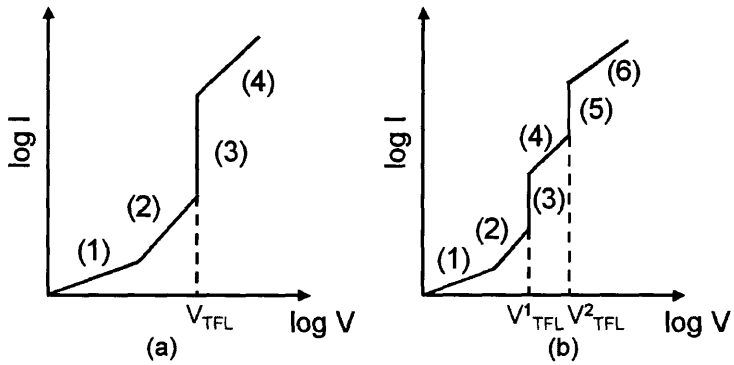

Figure 8-3: Sketch of space-charge limited conduction (SCLC) current-voltage characteristics for low mobility semiconductor with (a) a single trap level - (1) Ohmic Region (2) SCLC in the presence of shallow trapping (3) trap-filled limit (4) SCLC in the absence of trapping (b) two distinct trap levels - (3) and (5) trap filled limits marking the filling of all traps lying lower than the quasi-Fermi energy

energy of trap distribution is an important factor in designing active devices.[54] For example, recent studies of organic bistable memories proposed that charge trapping process can control the active state of the device.[10] [55] By controlled doping, we can engineer charge storage in active organic electronic devices.

Chapter 9

Organic/Metal/Organic Memory

9.1 Device Fabrication

9.1.1 Structure and Fabrication

Recently, electrically bistable organic device consisting of a thin metal layer embedded within the organic material is reported to show one million write-erase cycles in ambient conditions without significant degradation.[10] In that demonstration 2-amino-4,5-imidazoledicarbonitrile (AIDCN) was used for the organic material and aluminum (Al) for the embedded metal layer, as well as for the two external electrodes. However, there has been no accepted explanation why this structure shows memory behavior.[56] [55] To examine the observed memory phenomenon, we made similar organic/metal/organic structures. By thermal evaporation, we deposited aluminum tris (8-hydroxyquinoline) (Alq_3) for the organic material layer, and silver (Ag) for the embedded thin metal layer. In an alternate structure, laser dye [2-methyl-6-[2-(2,3,6,7-tetrahydro-1H, 5H-benzo [i,j] quinolizin-9-yl)-ethenyl]-4H-pyran-4-ylidene] propane-dinitrile (DCM2) (available from Exciton, Dayton, OH, under brand name LD688) is used instead of the middle metal layer. The schematic pictures of the structures that we studied are shown in Figure 9-1 and Figure 9-2. Energy level alignment of both structures is designed to introduce trap states in the devices. By using different materials, we can generate different energy depth trap states because

of the difference in the energy band alignment.

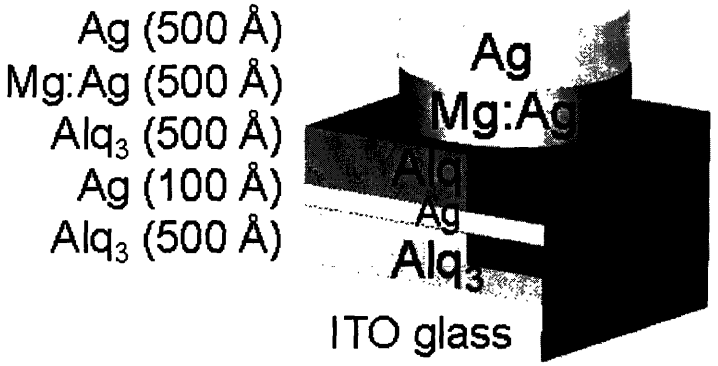

Figure 9-1: Structure of organic memory with a metal trap layer

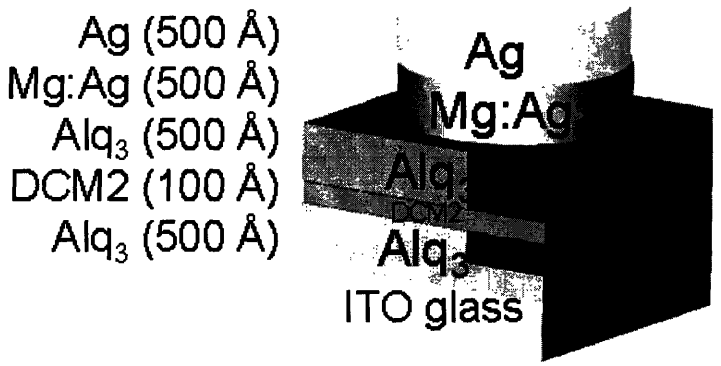

Figure 9-2: Structure of organic memory with an organic trap layer

Figure 9-3 shows expected energy band diagram of two devices with different trap states.[57] [58] [59] For a metal trap device, the actual band alignment is slightly different from Figure 9-3 because Metal/Organic and Organic/Metal interfaces are energetically different as described by Kahn et al.[58]

The devices are grown on indium tin oxide (ITO) coated glass and a composite Mg:Ag (10:1 mass ratio) and a Ag electrode is deposited through a circular shadow mask resulting in the device area of 0.78 mm^2 without breaking vacuum. Ag is used

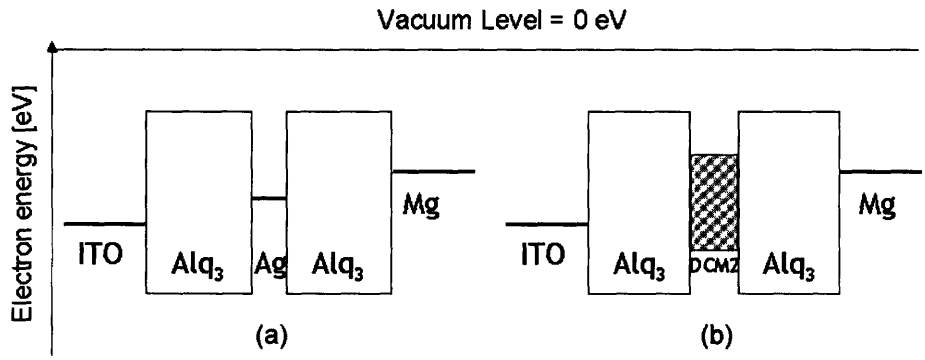

Figure 9-3: Expected energy band diagram of memory devices at equilibrium: (a) metal trap layer device (b) organic trap layer device

as a capping layer to prevent oxidation of Mg. The ITO glass is cleaned by solvents and UV-ozone following the procedures described in Figure 9-4.

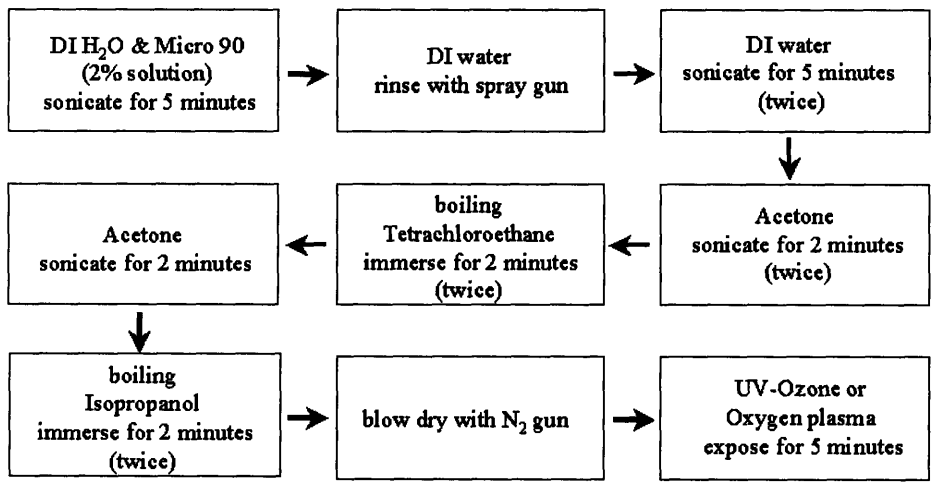

Figure 9-4: Substrate cleaning procedures

Figure 9-5 is the picture of the thermal evaporation system that is used for the device growth. The system has six evaporation boats with two power sources. Two independent thickness monitors can monitor film thickness during co-evaporation. The base pressure of this system is 7×10^{-8} Torr. The schematic picture of the inside view of the evaporation system used to make samples is shown in Figure 9-6.

The thermal evaporator is connected to two glove boxes via a vacuum transfer line so that all sample growth can be done in nitrogen or high vacuum. The picture of the glove boxes are shown in Figure 9-7. We can exchange shadow masks for patterning electrode layers in high vacuum ($\sim 1 \times 10^{-7}$ Torr) in the mask storage part of the transfer line.

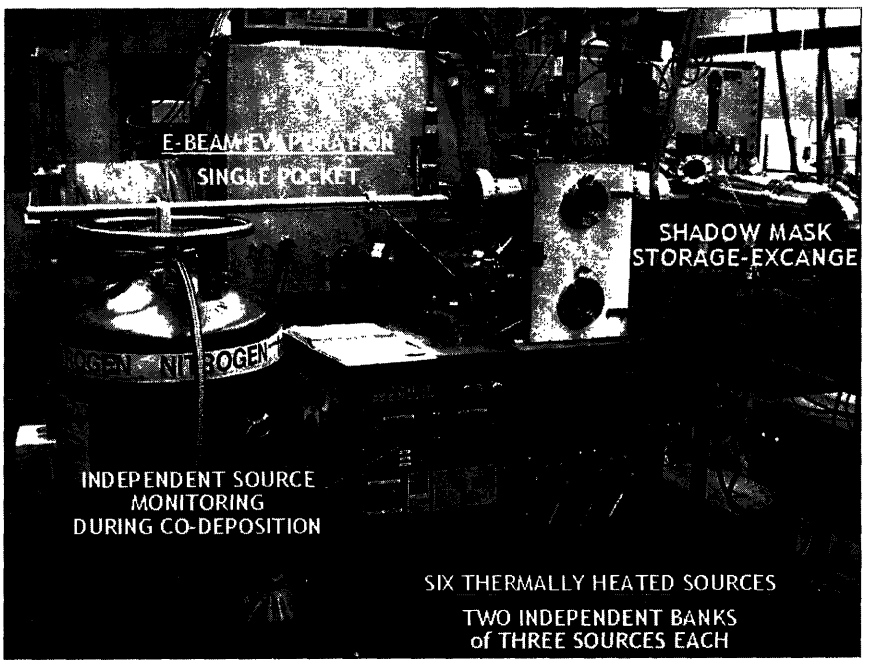

Figure 9-5: Thermal evaporation system for device growth

9.1.2 Choice of Materials

Alq_3 is a widely used material in organic devices ever since its use in the first organic light emitting devices.[20] Alq_3 has stable carrier transporting characteristics, easy film formation, and high stability. There are many references describing its electronic and optical properties. DCM2 is a red emitting dye that is chosen to form trap states in the Alq_3 due to its expected energy band lineup but other materials can be used as well. Experiments on these well-known material sets will allow us to generate a picture of the principles underlying the operation of the tested devices, and to reach

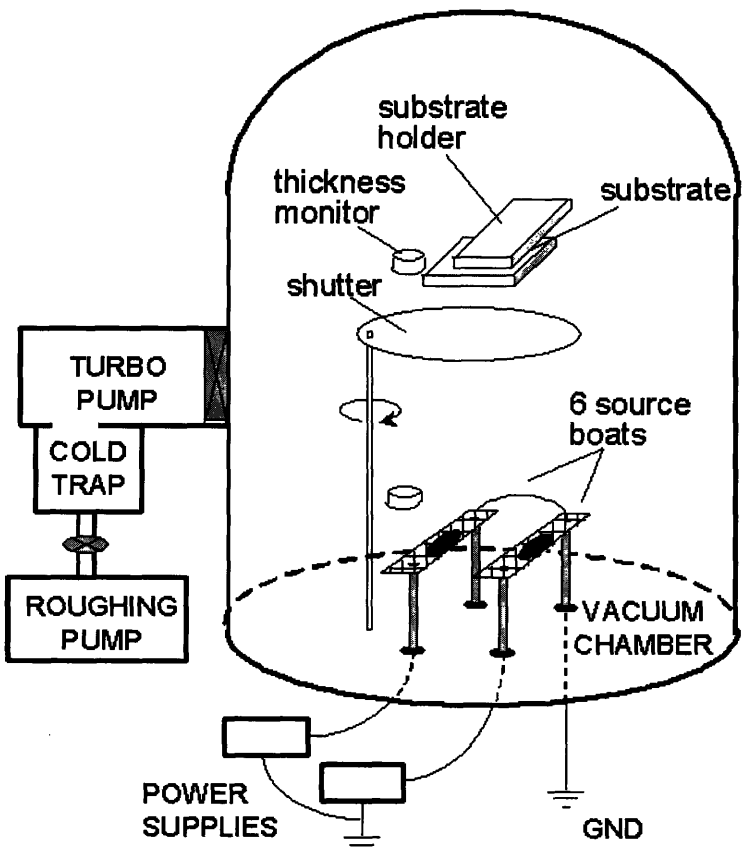

Figure 9-6: Schematic diagram of the inside view of the thermal evaporation chamber

general conclusions that apply to other material systems.

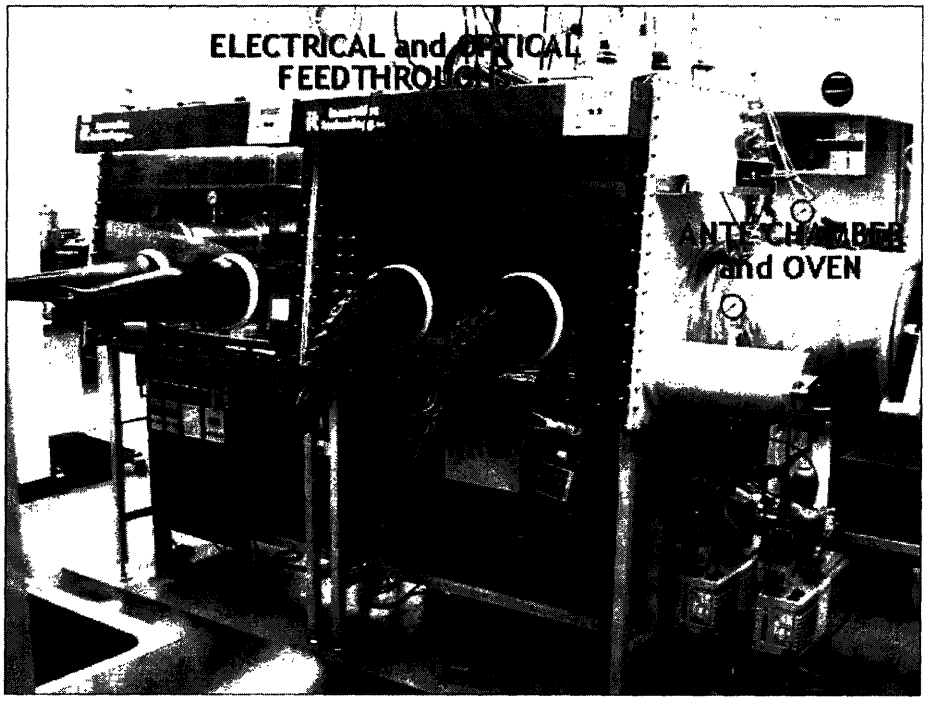

Figure 9-7: Two glove boxes for dry and wet processing

9.2 Experimental Results

9.2.1 Current-voltage Characteristics

The I-V sweep is measured by Agilent 4156C Semiconductor Parameter Analyzer in ambient without device packaging. The sweep starts from -3 V, reaches 3 V and returns to the starting voltage. Figure 9-8 shows the I-V characteristics of the Organic/Metal/Organic device sketched in Figure 9-1. Initially, the current is in the nA - μA range ("off" state), however, when the voltage reaches approximately 2.7 V, the current suddenly increases million times and stays in the high current state ("on" state) as the sweep is reversed. As the reverse bias increases, the current of the device decreases to one ten thousandth in magnitude. The ratio between high current and low current at a same voltage (on/off ratio) is plotted in the inset of Figure 9-8.

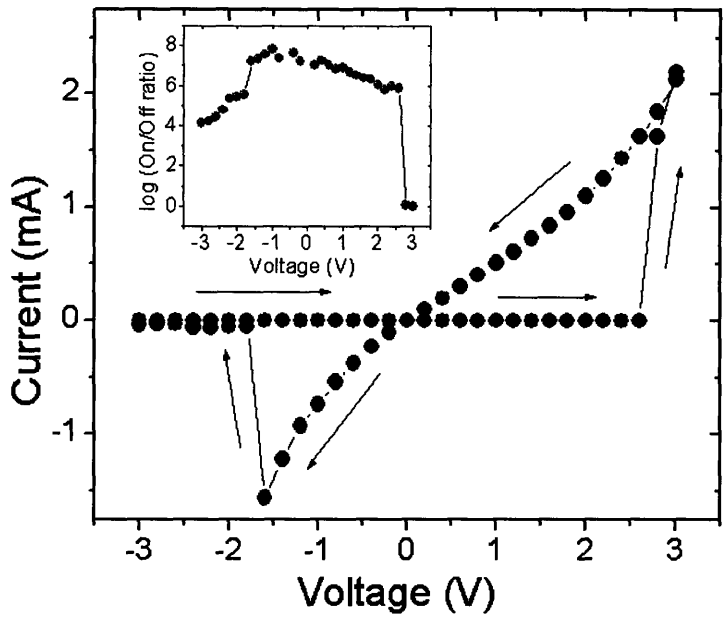

Figure 9-8: Current-voltage characteristics of the organic/metal/organic device sketched in Figure 9-1.

The cyclic characteristic of the organic/metal/organic device are measured as shown in Figure 9-9. -3 V to 3 V double sweep is repeated six times to see the changes of I-V. The log-log plot of I-V characteristics for forward bias region is shown at right. We can see that the current at the starting point changes by orders of magnitude depending on a specific sweep but the "on" state current is similar for every sweep. The slope at the switching is $\sim$ 50 mV/dec and the switching voltage is different from one sweep to another. We note that the sweeps with the smallest reverse bias currents have the highest turn-on voltages.

If the middle metal layer is replaced by DCM2 layer, the I-V characteristic changes as shown in Figure 9-10. The overall behavior looks similar, but the switching voltage is $\sim$ 1.7 V and on/off ratios is $\sim$ 50.

For 10 % DCM2:Alq_3 doping layer device, the effect of thickness is studied. Figure 9-11 shows the I-V characteristics of 100 $\AA$ and 50 $\AA$ thick DCM2:Alq_3 layer devices. The thicker middle layer device shows 3 orders of magnitude lower "off state" current (on/off ratio - 1000 times higher), and it has 0.1 V higher switching voltage.

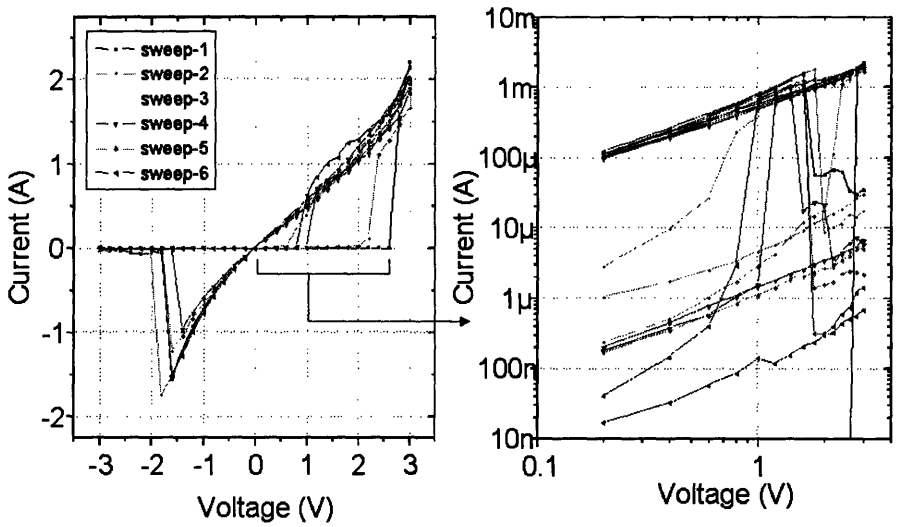

Figure 9-9: Cyclic characteristics of organic/metal/organic device

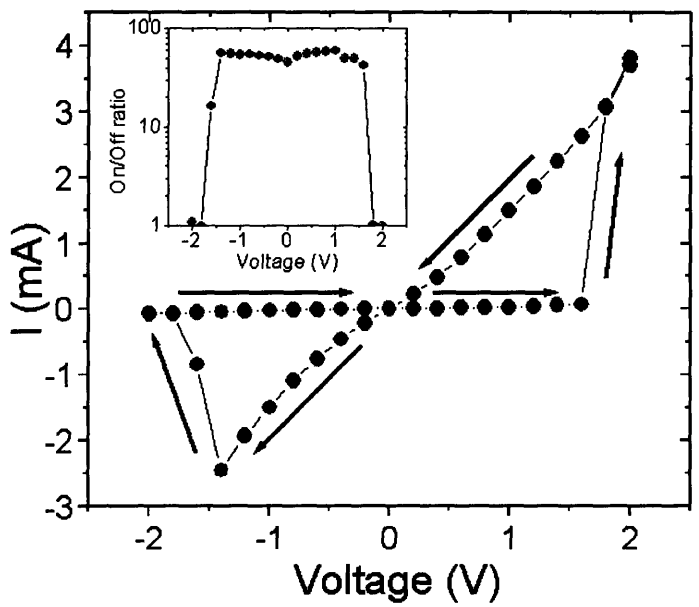

Figure 9-10: Current-voltage characteristics of organic/organic trap/organic device sketched in Figure 9-2.

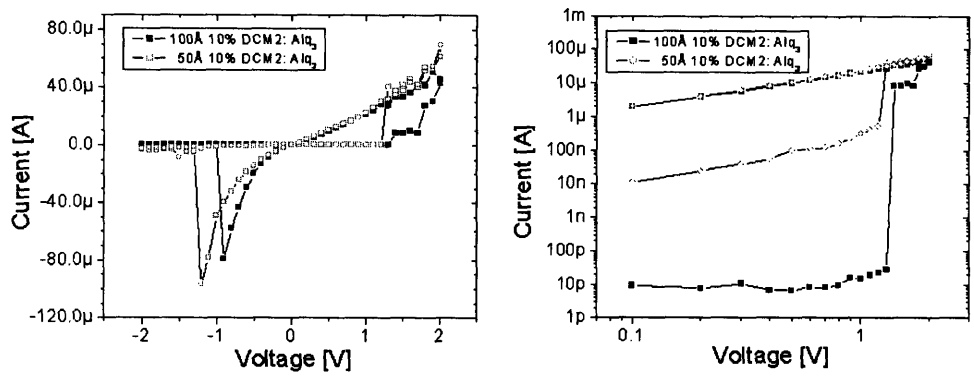

Figure 9-11: Current-voltage characteristics of the Figure 9-2 device with same concentration, but different thickness layers of the DCM2:Alq_3 layer.

9.2.2 Time Resolved Measurement

Figure 9-12 shows the time resolved I-V characteristic of the organic/metal/organic device. The write-read-erase-read cycles were recorded with a Tektronix TDS300B oscilloscope using an Agilent 33220A arbitrary waveform generator and a Keithley 428 current amplifier. The difference between the read and re-read currents demonstrates the "on" and "off" state of the device.

The time resolved I-V characteristic of Organic/Organic Trap/Organic device is also tested as Figure 9-13. The organic middle layer device has a lower switching voltage compared with a metal middle layer device. Both devices show memory behavior.

9.2.3 Formation of Nanocluster

In order to see how Ag layer is deposited on an organic layer, atomic force microscope picture is taken for the middle layer of the organic/metal/organic device. Figure 9-14 shows the AFM picture of 100 Å Ag on Alq_3, which forms nanoclusters that could trap charge. Ma et al.[56] and Bozano et al.[55] reported that very thin (< 100 Å) layer of Al on organic materials formed nanoclusters. Bozano et al. prepared and

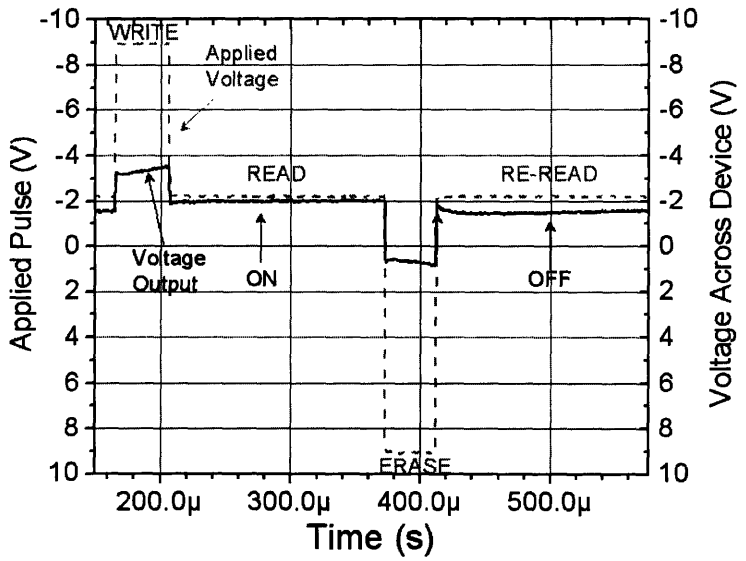

Figure 9-12: Time resolved characteristics of organic/metal/organic device

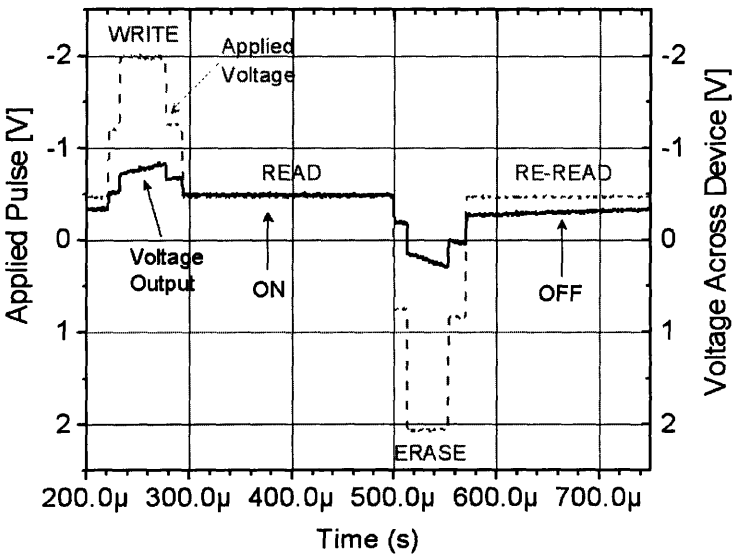

Figure 9-13: Time resolved characteristics of organic/organic trap/organic Device

analyzed different thickness insulating layers (5-40 nm) and different metals (Al, Cr, Cu, Mg, Ag). They reported that, in general, metal layers less than 10 nm thick showed a granular structure and a discontinuous profile.[55]

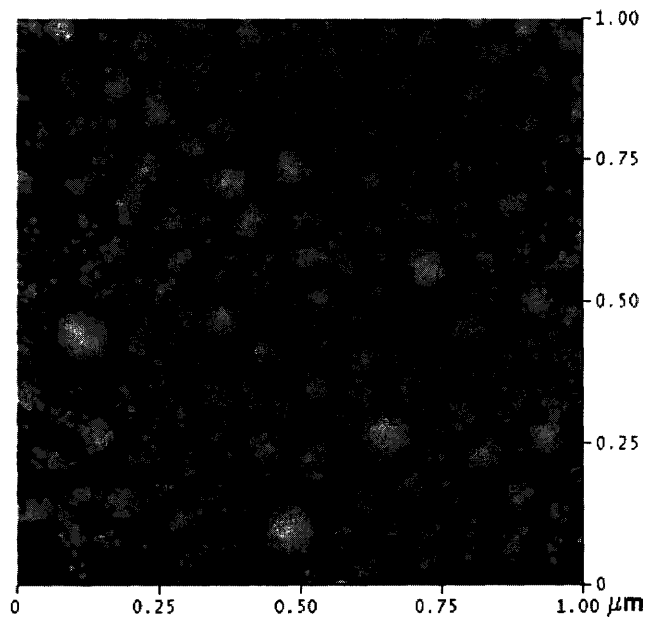

Figure 9-14: Atomic force microscope (AFM) image of 100Å Ag on Alq_3

9.3 Discussion

9.3.1 Mechanism: Trap Limited Conduction

In organic thin films, which are usually low mobility semiconductors, current flows by carrier injection. However, if there are trap states in materials, they reduce mobility of carriers and result in low current as described in Figure 8-2 of Chapter 8.2. In Figure 9-15 (a), the device is initially in low current state because there are many empty trap states, thus the mobility of carriers through the device is low and it results in a low current. However, as we apply voltages to the device, injected carriers can fill trap states. Thus, the mobility is increased to an intrinsic value without trap states. By trap filling processes, the device switches to a high current state at 2.7 V. When

the sweep is in reverse direction, the current stays high initially and changes back to low state as the traps are emptied again. This way, we can write and erase the memory device.

In short, the device is in the off states when the traps are not completely filled, but once all the traps are filled the device is turned on. The on/off ratio of this device is in the range of between 10^4 and 10^8. High on/off ratio is beneficial because we can program many different states and have high density storage capability. A sharp switching voltage and a large on/off ratio are desirable characteristics for the memory device. The maximum reported on/off ratio is 10^6.[10] The slope at the switching is $\sim$ 50 mV/dec as noted in 9.2.1. Typically, the inverse subthreshold of well designed metal oxide semiconductor field effect transistors (MOSFETs) at 300 K is 80 - 100 mV/dec. The organic memory device has a sharper switching voltage by trap filling limited conduction. From the six consecutive scans in Figure 9-9, we can see that the switching voltage changes depending on the previous state. If there are fewer empty states before starting a new sweep, it is easier to fill the trap states, thus the switching voltage is low. However, the on state currents are similar for all sweeps as discussed before, since the filled trap limit is the same for all sweeps.

There is another evidence that the charge trap mechanism plays an important role in the memory effect. If we compare Figure 9-15 (a) and (b), the memory device with a thin metal trap layer between organic materials shows higher on/off ratio due to the large reduction in mobility from its large trap density. The metal trap device has a higher on/off ratio because the off state current of the metal trap device is more than two orders of magnitude smaller than that of the organic trap layer device. The on state current of both devices are in the same order of magnitude because both devices use same materials and similar processing parameters except the middle trap layer.

From the photoemission spectroscopy experiments [57] and reported energy values [59] the energy of metal trap and organic trap is expected to be 0.9 eV and 0.3 eV, respectively. The organic trap layer device shows a lower switching voltage, because it is easier to fill the trap states due to shallow trap states of organic middle layer

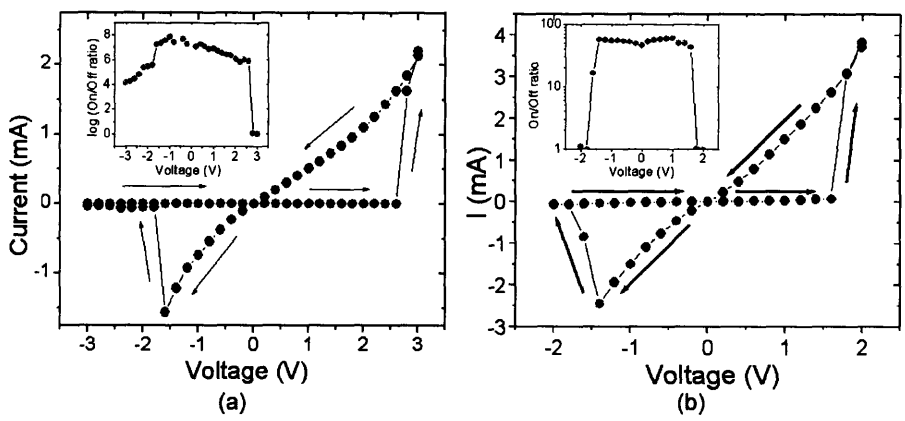

Figure 9-15: Comparison of Current-Voltage Characeteristics of (a) Metal and (b) Organic Trap Layer Device

device compared with metal traps. Because the metal trap is deeper, when the traps are not filled (off state), the carrier mobility is lower than that of the organic trap layer device, resulting in lower off state current.

The observed I-V characteristics of two different trap layer devices can therefore be explained by the trap filling model and the trap energy values. If we change the thickness of trap layer for the same DCM2 dopant concentration, as shown in Figure 9-11, the thicker trap layer device shows higher switching voltage and lower off current because it is harder to fill more trap states. From the experimental results and the underlining principles, we can have following conclusions:

If the trap energy and concentration are high,

1. The on/off ratio is high due to a low off current.

2. The switching voltage is high because we need more carriers to fill the trap states.

Chapter 10

Reverse Biased Organic Light Emitting Devices

10.1 Device Fabrication

10.1.1 Structure and Fabrication

The trapping phenomenon described in Chapter 9 suggests that charge can be stored in organic layered structures. We re-examined this premise in a second organic device that is similar to an organic LED.

The structure of the device consists of an organic layer (material #1)/trap layer/organic layer (material #1)/organic layer (material #2) between an anode and a cathode as shown in Figure 10-1. We use N,N'-diphenyl-N,N'-bis (3-methylphenyl)-1,1'-biphenyl-4,4'-diamine (TPD) as material #1 and aluminum tris (8-hydroxyquinoline) (Alq_3) as material #2. The trap layer is a mixture of 95% TPD and 5% laser dye [2-methyl-6-[2-(2,3,6,7-tetrahydro-1H, 5H-benzo [i,j] quinolizin-9-yl)-ethenyl]-4H-pyran-4-ylidene] propane-dinitrile (DCM2) (available from Exciton, Dayton, OH, under brand name LD688) deposited using co-evaporation. For substrate cleaning and electrode deposition, the same procedures are used as those described in 9.1.1. This structure is a modification of a standard OLED as it contains the trap layer.

A second set of trapping device structures with a metal trap layer is made by

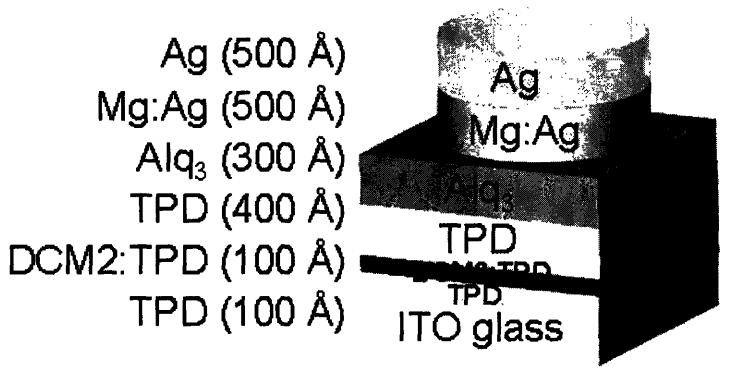

Figure 10-1: Structure of doped organic light emitting device

depositing 5 nm of Ag instead of the DCM2 doped TPD trap layer. Figure 10-2 shows the structure of the metal-trap layer device. Other metals can also be used for making the trap layer.

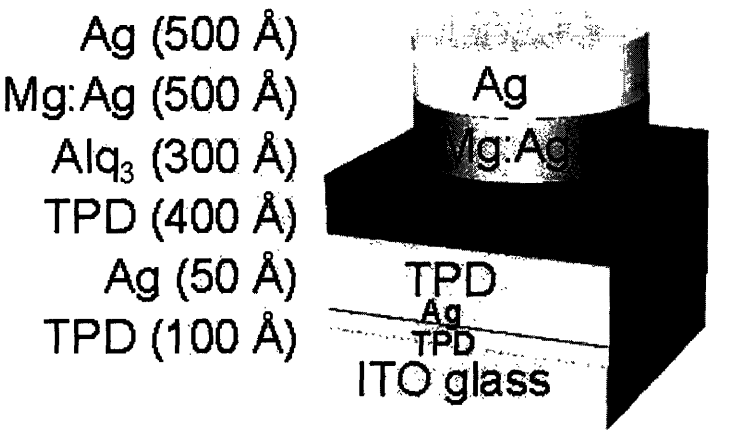

Figure 10-2: Structure of organic light emitting device with a metal trap layer

10.2 Experimental Results

10.2.1 Current-voltage Characteristics

Figure 10-3 shows the I-V characteristics of the doped organic light emitting devices measured using Agilent 4156C semiconductor parameter analyzer under ambient conditions. The shape of each I-V response is repeatable and depends on the bias at which the sweep is started. By comparing the I-V characteristics we find that current spikes at 1V forward bias are observed only when the device is first subjected to a reverse bias of at least -2V. To ensure that the device is in the same initial state, before every sweep that started at reverse bias, we performed a sweep that started at 0V bias. Comparing this I-V behavior to a control device, which has no doping layer but the same total thickness of the TPD layer, we note that the control device did not show the current spike for sweeps that started at reverse bias.

From a series of experiments using different charging time, we observe that the voltage at which the current spike occurs can be lowered to a certain degree if we first apply reverse bias for a few seconds prior to measuring the I-V sweep. Also, this experiment suggests that pre-charging time determines the amount of injected/stored charge in the charge trapping layer, and hence influences the current response in the forward bias sweep. For I-V sweeps that start at 0 V, the doped device compared with a TPD-Alq_3 OLED of same thickness, has about 10 % higher quantum efficiency due to a more balanced hole and electron transport.[60] The turn-on voltage, however, is higher in the doped device than in the OLED with the current 10-fold smaller at the same voltage.[61]

Figure 10-4 shows the I-V characteristics of the metal-trap devices of Figure 10-2. When a thin Ag film is deposited on top of the organic layer, it forms metal clusters similar to the earlier studies of Al on AIDCN.[55] The atomic force microscopy (AFM) image shows Ag cluster average size of $\sim$ 10 nm. The metal-trap devices still show the memory behavior. The peak of the electroluminescence spectrum, however, is shifted due to the microcavity effects induced by the reflection at the 5 nm Ag layer.

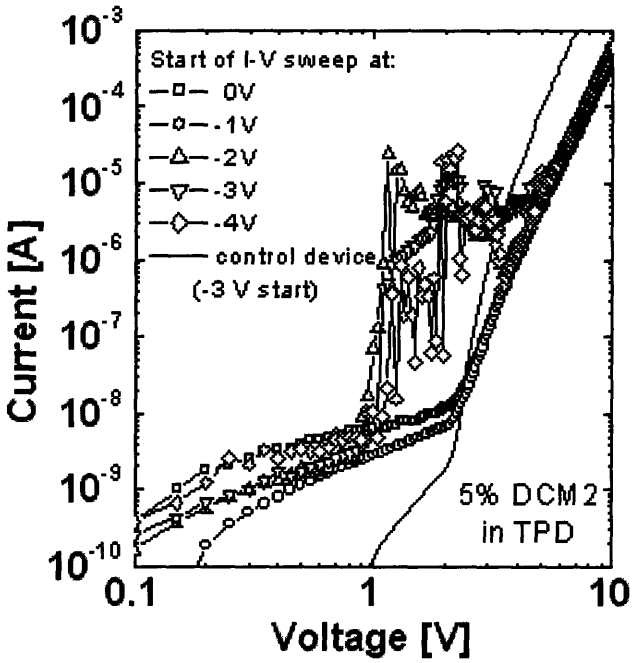

Figure 10-3: The current-voltage characteristic of 5 % DCM2 doped TPD trap layer device of Figure 10-1. The I-V characteristics were measured by Agilent 4156 C semiconductor parameter analyzer under ambient conditions with medium integration time setup. The legend indicates the voltage at which the sweep was started. The maximum voltage in each sweep was 10V.

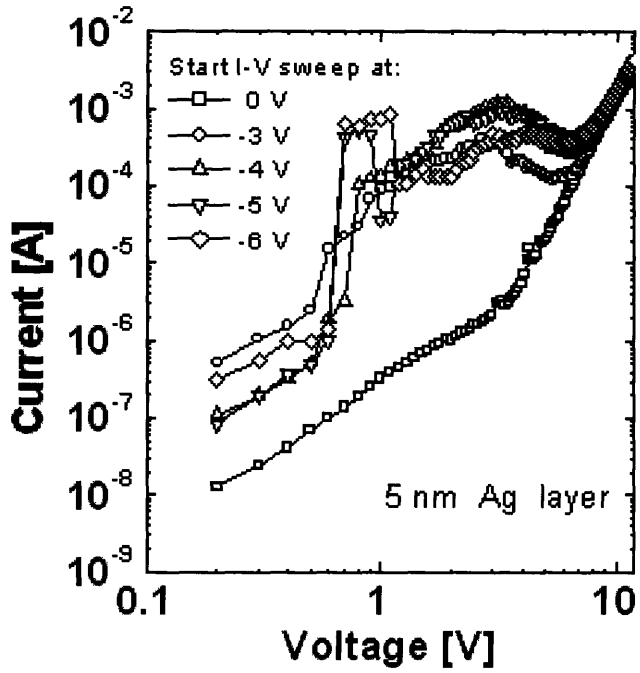

Figure 10-4: Current-voltage characteristic of metal trap device of Figure 10-2.

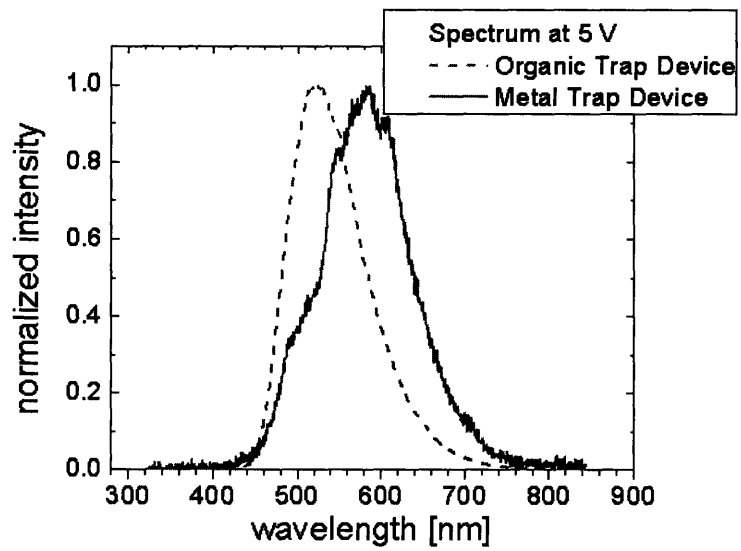

Figure 10-5: Electroluminescence spectrum of organic and metal trap layer device

10.2.2 Time Resolved Measurement

Figure 10-6 shows the time resolved I-V characteristic of the DCM2:TPD trap layer device. The write-read-erase-read cycles were recorded with an oscilloscope using an arbitrary waveform generator and a current amplifier. The difference between the read and re-read currents demonstrates the "on" and "off" state of the bit stored in the doped organic light emitting device. We measured the retention time of the device by delaying discharge. After applying negative bias, we waited for up to two hours before "reading" the device with an I-V sweep, and we still observed the current spike associated with charge storage.

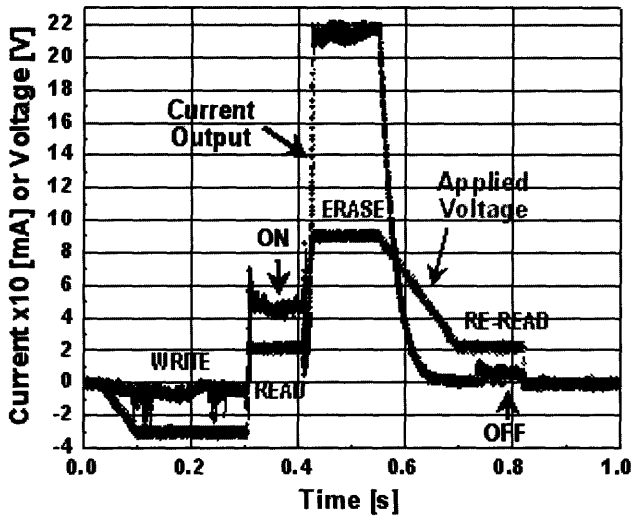

Figure 10-6: Write-Read-Erase-Read cycle of the 5 % DCM2:TPD trap layer device of Figure 10-1. The writing, reading and erasing voltage is -3 V, 2 V and 9 V, respectively.

10.3 Discussion

10.3.1 Mechanism: Charge Storing

A schematic band diagram shown in Figure 10-7 illustrates the proposed operating mechanism of the charge trapping OLED. When the device is reverse biased, electrons

injected from the anode charge the trap layer. If we then apply a forward bias, holes from the anode recombine with the trapped DCM2 electrons generating the current spike. The remainder of the injected holes combine with injected electrons from the cathode to form excitons on Alq_3. By changing the magnitude of the reverse bias, we can control the amount of stored charge in the trap layers and therefore the magnitude of the spike current. If the magnitude of the reverse bias is too small, no current spike in forward bias is observed as the reverse bias voltage is insufficient to facilitate electron injection over the anode/TPD interface. If too great reverse bias is applied, the net amount of stored charge is reduced due to hole injection at the cathode. This leads to a smaller spike current response for reverse biases of < -5 V.

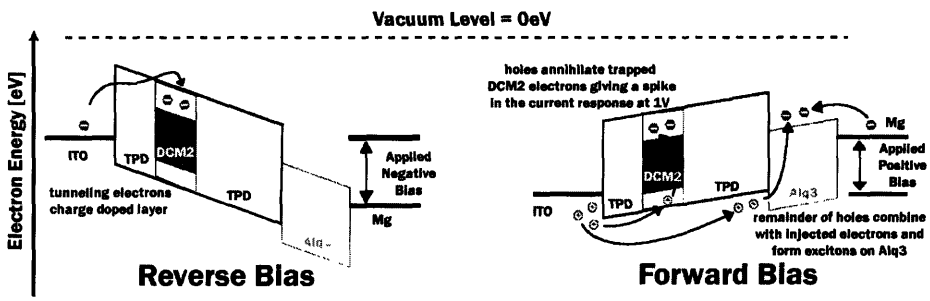

Figure 10-7: Proposed operation mechanism of doped organic light emitting device. The expected energy band diagrams are not drawn to scale.

The hole injection at the cathode is small at a low reverse bias because Alq_3 is an electron transporting layer. The hole injection becomes significant at a high reverse bias because more holes can transport through the Alq_3 layer because Alq_3 is not a perfect hole blocking layer. At reverse bias, electrons are injected from the anode by tunneling because the TPD layer is 100 $\AA$ and the roughness of ITO used for making samples is $\sim$ 15 $\AA$ from the AFM picture of Figure 10-8.

From the difference in the current at a low voltage ("reading voltage", for example, 1 V), we can tell whether charges are stored in the trap layer. This way, we can write and read the memory state. The device can be erased by applying a large forward bias as explained in Figure 10-7. We can also read the state of the device from an optical

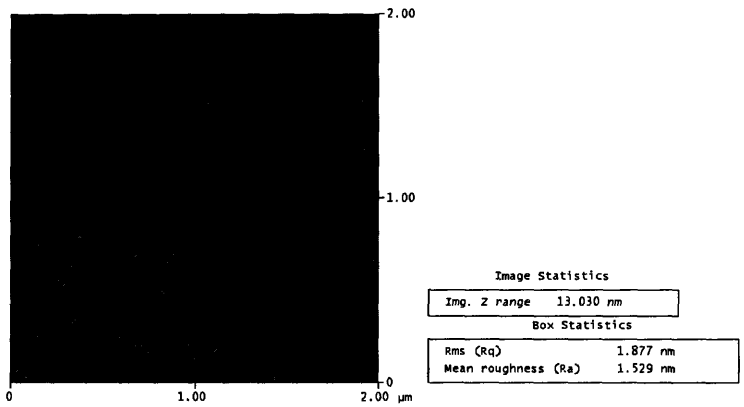

Figure 10-8: Roughness Study of ITO by atomic force microscope

signal because electrons and holes recombine and emit light if charges are stored in the trap layer. This way, we can write electrically and read either from electrical or optical signals. Ma el al. reported organic bistable light emitting devices by combining an organic memory with a polymer light emitting diode.[62] This device has a high switching voltage ($\sim$ 6 V) because it is a series connection of the two different devices.

Based on the above model, we made similar trapping devices with a metal trap layer by depositing 5 nm of Ag instead of DCM2 doped TPD. From the previous study, it is known that the metal trap has a higher energy. By comparing Figure 10-3 with Figure 10-4, we can see that the metal trap device shows higher current because metal layer can store more charges compared with organic material. The on/off ratio of this device is smaller than the organic/organic trap/organic layer device, but it shows more stable I-V characteristics and longer retention time.

In order to see the effect of different doping concentrations, we fabricated samples with 10 % and 20 % DCM2 doped TPD trap layer, and compared the device characteristics with the 5 % DCM2 doped device as shown in Figure 10-9. If we increase the doping concentration, we need more voltage to extract trapped charges from the device. This is consistent with assertion that devices with a higher concentration of trap states are harder to neutralize. In the case of the highly polar DCM2 the

energy structure changes with doping possibly resulting in deeper trap energies when matched to TPD.[52] The retention time of the device also increases as we increase the doping concentration consistent with the deeper trap assertion.

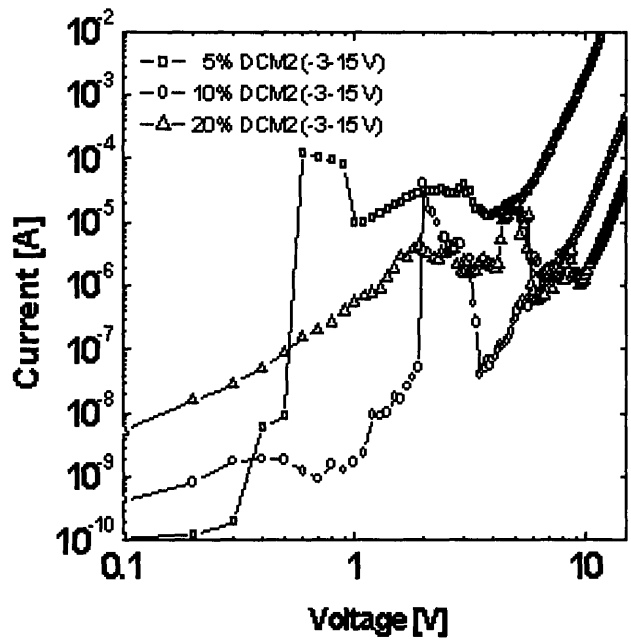

Figure 10-9: The comparison of the current-voltage characteristics for the devices with different doping concentrations. The doping concentrations are taken from the mass fractions of the DCM2 in the doped layers.

10.3.2 Photoluminescence Quenching Measurement

In order to verify that charges are stored in the trap layer, we measured photoluminescence (PL) of DCM2 for charged and discharged trap layer. The device structure is as shown in Figure 10-3. The DCM2:TPD trap layer device is used for the PL measurement, because we can not see photoluminescence from a metal trap layer. The PL measurement was performed by exciting the device with a 532 nm frequency doubled Nd:YAG laser while applying a square wave bias over the device using Agilent 33250A arbitrary waveform generator. The 532 nm wavelength light is only absorbed by DCM2, resulting in red PL signal that is detected by Newport 818-SL photodiode

connected to Stanford Research SR 830 lock-in amplifier. The lock-in amplifier is referenced to the frequency of the square wave bias applied over the device, and the response is recorded on the Tektronix TDS 300B oscilloscope. When the trap layer is charged, the PL intensity from DCM2 decreases due to the trapped-electron-induced Auger quenching of DCM2, as shown in Figure 10-10. This is a strong evidence that the charges are stored in the trap layer. Assuming that only charged molecules are quenched with no influence on the neighboring molecules, the $\sim$ 10 % change in the PL intensity implies the same percentage of charged DCM2 sites or 10^{18} cm^{-3} (the density of the DCM2 is 1.1 g/cm^{-3}, and the molecular weight of DCM2 and TPD is 355.2 g/mol and 516.3 g/mol, respectively).

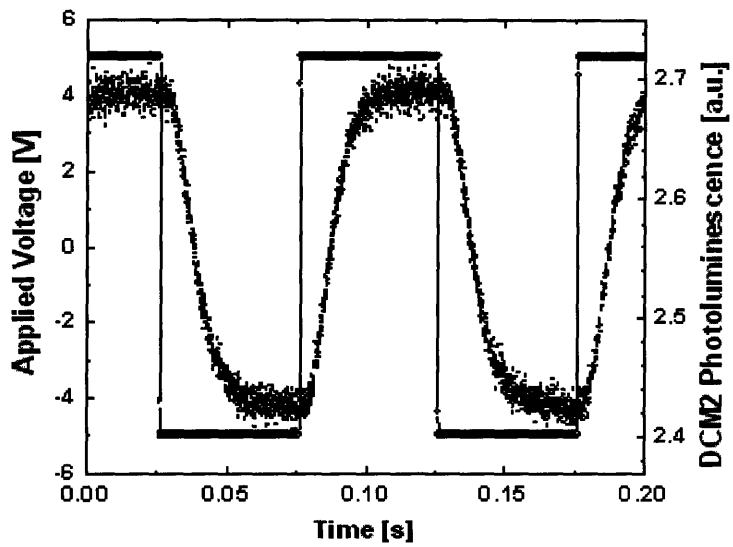

Figure 10-10: The DCM2 photocurrent with the applied pulse. The chopper frequency was in the range of 620-650 Hz and the OG-530 filter (Ealing catalog Inc., Rocklin, CA) was used to detect only DCM2 PL signal.

Fujii et al. reported that photoluminescence (PL) intensity from an organic multilayer structure using Alq_3 and TPD had been modulated by applying reverse bias voltage and PL intensity decreased with increasing reverse bias voltage. They claimed that the PL intensity of the device decreased due to field assisted dissociations of excitons.[63]. Hieda et al. reported PL quenching of a hole transport material

tetra(N,N-diphenyl-4-aminophenyl)ethylene (TTPAE) induced by injected carriers in organic thin films. They evaporated thin films of TTPAE onto thermally oxidized Si substrates and put Cr/Au as a top electrode. From displacement current measurements, they showed that the quenching efficiencies depend strongly on the polarities of injected charges and that quenching can not be explained by the external field-induced exciton dissociation.[64] They made a hypothesis that Coulomb interaction between photoexcited molecules and injected carriers caused PL quenching. And they showed that hole injections played an essential role in the quenching mechanism.[65] Recently, Young et al. reported that the electroluminescent (EL) efficiency of an OLED containing a doped layer Alq_3:DCJTB is found to decrease with increasing current density. And it is attributed to the quenching of DCJTB* by cationic species, either $DCJTB^+$ or possibly $Alq_3{}^+$, but not the corresponding anionic species.[66] [67] In comparison, our work shows that charges are actually stored in the designed trap layer (doped DCM2:TPD layer) of multilayer structures by electron tunneling and shows a direct evidence of trapped charges in organic materials by photoluminescence quenching experiment.

Chapter 11

Conclusion

Charge trapping in organic hetero-junction structures results in two distinct phenomena that both manifest as a memory behavior. Trapped charge can

1. increase the carrier mobility in organic structures.
2. generate current during the de-trapping process.

Both processes are demonstrated in practical structures. We demonstrated:

- That organic hetero-junction structures can controllably trap and release electronic charges.
- That the energy band structure and experimental data from these devices give a strong indication that both DCM2 sites and metal trap layer are trapping electrons under reverse bias
- That charges are actually stored in the trap layer by PL quenching measurement and the trap density is on the order of 10^{18} cm^{-3}.
- That for a fixed charging time, the magnitude of applied reverse bias determines the amount of stored charge in the trap layer, influencing the current response in the forward bias sweep.
- That when the organic trap layer is replaced with a metal layer, the higher density of trap states in the metal layer results in higher discharge current.

- That from time resolved measurements, the trapping layers within an OLED structure allow storage of information on the OLED by applying reverse bias on the device. The retention time of the device is in excess of 2 hours.

Bibliography

[1] Universal display corporation (http://www.universaldisplay.com).

[2] D. J. Gundlach, L. L. Jia, and T. N. Jackson. Pentacene tft with improved linear region characteristics using chemically modified source and drain electrodes. *IEEE Electron Device Letters*, 22:571–573, 2001.

[3] D. Mascaro. *Forming oriented crystal needles by solvent vapor annealing of amorphous thin films on nano-patterned substrates.* PhD thesis, Massachusetts Institute of Technology, 2004.

[4] H. Sirringhaus, T. Kawase, R. H. Friend, T. Shimoda, M. Inbasekaran, W. Wu, and E. P. Woo. High-resolution inkjet printing of all-polymer transistor circuits. *Science*, 290:2123–2126, 2000.

[5] K. Takahashi, N. Kuraya, T. Yamaguchi, T. Komura, and K. Murata. Three-layer organic solar cell with high-power conversion efficiency of 3.5%. *Solar Energy Materials and Solar Cells*, 61:403–416, 2000.

[6] K. J. Albert, N. S. Lewis, C. L. Schauer, G. A. Sotzing, S. E. Stitzel, T. P. Vaid, and D. R. Walt. Cross-reactive chemical sensor arrays. *Chemical Reviews*, 100:2595–2626, 2000.

[7] S. Poyard, N. Jaffrezic-Renault, C. Martelet, S. Cosnier, and P. Labbe. Optimization of an inorganic/bio-organic matrix for the development of new glucose biosensor membranes. *Analytica Chimica Acta*, 364:165–172, 1998.

[8] Q. M. Zhang, H. F. Li, M. Poh, F. Xia, Z. Y. Cheng, H. S. Xu, and C. Huang. An all-organic composite actuator material with a high dielectric constant. *Nature*, 419:284–287, 2002.

[9] V. G. Kozlov, V. Bulovic, P. E. Burrows, and S. R. Forrest. Laser action in organic semiconductor waveguide and double-heterostructure devices. *Nature*, 389(6649):362–364, 1997.

[10] L. P. Ma, J. Liu, and Y. Yang. Organic electrical bistable devices and rewritable memory cells. *Applied Physics Letters*, 80:2997–2999, 2002.

[11] S. Wasmus and A. Kuver. Methanol oxidation and direct methanol fuel cells: a selective review. *Journal of Electroanalytical Chemistry*, 461:14–31, 1999.

[12] Z. N. Bao, V. Bulovic, and A. B. Holmes. Electroactive organic materials. *MRS Bulletin*, 27(6):441–442, 2002.

[13] N. C. Greenham and R. H. Friend. Semiconductor physics of conjugated polymers. *Solid State Physics*, 49:1, 1995.

[14] A. C. Fou, O. Onitsuka, M. Ferreira, M. F. Rubner, and B. R. Hsieh. Fabrication and properties of light-emitting diodes based on self-assembled multilayers of poly(phenylene vinylene). *Journal of Applied Physics*, 79:7501–7509, 1996.

[15] V. Bulovic, P. E. Burrow, S. R. Forrest, and M. E. Thompson. Transparent light-emitting devices. *Nature*, 380(6569):29–29, 1996.

[16] G. Gu, P. E. Burrows, S. Venkatesh, S. R. Forrest, and M. E. Thompson. Vacuum-deposited, nonpolymeric flexible organic light-emitting devices. *Optics Letters*, 22(3):172–174, 1997.

[17] C. C. Wu, S. D. Theiss, G. Gu, M. H. Lu, J. C. Sturm, S. Wagner, and S. R. Forrest. Integration of organic LED's and amorphous Si TFT's onto flexible and lightweight metal foil substrates. *IEEE Electron Device Letters*, 18(12):609–612, 1997.

[18] M. Pope, H. P. Kallmann, and P. Magnante. Electroluminescence in organic crystals. *Journal of Chemical Physics*, 38:2042–2043, 1963.

[19] L. J. Rothberg and A. J. Lovinger. Status of and prospects for organic electroluminescence. *Journal of Materials Research*, 11(12):3174–3187, 1996.

[20] C. W. Tang and S. A. Vanslyke. Organic electroluminescent diodes. *Applied Physics Letters*, 51:913–915, 1987.

[21] J. H. Burroughes, D. D. C. Bradley, A. R. Brown, R. N. Marks, K. MacKay, R. H. Friend, P. L. Burn, and A. B. Holmes. Light-emitting-diodes based on conjugated polymers. *Nature*, 347:539–541, 1990.

[22] P. L. Burn, D. D. C. Bradley, R. H. Friend, D. A. Halliday, A. B. Holmes, R. W. Jackson, and A. Kraft. Precursor route chemistry and electronic-properties of poly(p-phenylene-vinylene), poly[(2,5-dimethyl-p-phenylene)vinylene] and poly[(2,5-dimethoxy-p-phenylene)vinylene]. *Journal of the Chemical Society-Perkin Transactions 1*, pages 3225–3231, 1992.

[23] D. Braun and A. J. Heeger. Visible-light emission from semiconducting polymer diodes. *Applied Physics Letters*, 58:1982–1984, 1991.

[24] T. M. Brown, J. S. Kim, R. H. Friend, F. Cacialli, R. Daik, and W. J. Feast. Built-in field electroabsorption spectroscopy of polymer light-emitting diodes incorporating a doped poly(3,4-ethylene dioxythiophene) hole injection layer. *Applied Physics Letters*, 75:1679–1681, 1999.

[25] C.W. Tang, S.A. VanSlyke, and C.H. Chen. Electroluminescence of doped organic thin films. *Journal of Applied Physics*, 65:3610–3616, 1989.

[26] J. Shi and C.W. Tang. Doped organic electroluminescent devices with improved stability. *Applied Physics Letters*, 70:1665–1667, 1997.

[27] M. A. Baldo, M. E. Thompson, and S. R. Forrest. High-efficiency fluorescent organic light-emitting devices using a phosphorescent sensitizer. *Nature*, 403:750–753, 2000.

[28] P. F. Tian, P. E. Burrows, and S. R. Forrest. Photolithographic patterning of vacuum-deposited organic light emitting devices. *Applied Physics Letters*, 71:3197–3199, 1997.

[29] M. Ohring. *The Materials Science of Thin Films.* Academic Press, 2001.

[30] Y. N. Xia, J. A. Rogers, K. E. Paul, and G. M. Whitesides. Unconventional methods for fabricating and patterning nanostructures. *Chemical Reviews*, 99:1823–1848, 1999.

[31] P. Calvert. Inkjet printing for materials and devices. *Chemistry of Materials*, 13:3299–3305, 2001.

[32] Z. N. Bao, J. A. Rogers, and H. E. Katz. Printable organic and polymeric semiconducting materials and devices. *Journal of Materials Chemistry*, 9:1895–1904, 1999.

[33] D. Pede, G. Serra, and D. De Rossi. Microfabrication of conducting polymer devices by ink-jet stereolithography. *Materials Science and Engineering C-Biomimetic Materials Sensors and Systems*, 5:289–291, 1998.

[34] P. F. Blazdell, J. R. G. Evans, M. J. Edirisinghe, P. Shaw, and M. J. Binstead. The computer-aided manufacture of ceramics using multilayer jet printing. *Journal of Materials Science Letters*, 14:1562–1565, 1995.

[35] A. D. Bermel and D. E. Bugner. Particle size effects in pigmented ink jet inks. *Journal of Imaging Science and Technology*, 43:320–324, 1999.

[36] R. W. Vest, E. P. Tweedell, and R. C. Buchanan. Ink jet printing of hybrid circuits. *International Journal for Hybrid Microelectronics*, 6:261–267, 1983.

[37] K. F. Teng and R. W. Vest. Metallization of solar-cells with ink jet printing and silver metallo-organic inks. *IEEE Transactions on Components Hybrids and Manufacturing Technology*, 11:291–297, 1988.

[38] C. M. Hong and S. Wagner. Inkjet printed copper source/drain metallization for amorphous silicon thin-film transistors. *IEEE Electron Device Letters*, 21:384–386, 2000.

[39] Y. Y. Lin, D. J. Gundlach, S. F. Nelson, and T. N. Jackson. Stacked pentacene layer organic thin-film transistors with improved characteristics. *IEEE Electron Device Letters*, 18:606–608, 1997.

[40] D. J. Gundlach, T. N. Jackson, D. G. Schlom, and S. F. Nelson. Solvent-induced phase transition in thermally evaporated pentacene films. *Applied Physics Letters*, 74:3302–3304, 1999.

[41] H. Sirringhaus, P. J. Brown, R. H. Friend, M. M. Nielsen, K. Bechgaard, B. M. W. Langeveld-Voss, A. J. H. Spiering, R. A. J. Janssen, E. W. Meijer, P. Herwig, and D. M. de Leeuw. Two-dimensional charge transport in self-organized, high-mobility conjugated polymers. *Nature*, 401:685–688, 1999.

[42] W. Fix, A. Ullmann, J. Ficker, and W. Clemens. Fast polymer integrated circuits. *Applied Physics Letters*, 81:1735–1737, 2002.

[43] D. J. Gundlach, C. C. Kuo, S. F. Nelson, and T. N. Jackson. Organic thin-film transistors with field-effect mobility >2 $cm^2/V{\cdot}s$. *57th Device Research Conference Digest*, 21:164–165, 1999.

[44] H. Sirringhaus, N. Tessler, and R. H. Friend. Integrated optoelectronic devices based on conjugated polymers. *Science*, 280:1741–1744, 1998.

[45] J. D. Plummer, M. D. Deal, and P.B. Griffin. *Silicon VLSI Technology.* Prentice Hall, 2000.

[46] M. Baldo, M. Deutsch, P. Burrows, H. Gossenberger, M. Gerstenberg, V. Ban, and S. R. Forrest. Organic vapor-phase deposition. *Journal of Crystal Growth*, 156:91–98, 1995.

[47] P. Pavan, R. Bez, P. Olivo, and E. Zanoni. Flash memory cells-an overview. *Proceedings of the IEEE*, 85(8):1248–1271, 1997.

[48] Flash memory market trends. Technical Report 3, Fujitsu Limited, Electronic Devices, 2001.

[49] J. F. Scott and C. A. Araujo. Ferroelectric memories. *Science*, 246:1400–1405, 1989.

[50] E. Kapetanakis, P. Normand, D. Tsoukalas, K. Beltsios, J. Stoemenos, S. Zhang, and J. van den Berg. Charge storage and interface states effects in Si-nanocrystal memory obtained using low-energy Si+ implantation and annealing. *Applied Physics Letters*, 77:3450–3452, 2000.

[51] E. W. Wong C. P. Collier and, M. Belohradsky, F. M. Raymo, J. F. Stoddart, P. J. Kuekes, R. S. Williams, and J. R. Heath. Electronically configurable molecular-based logic gates. *Science*, 285:391–394, 1999.

[52] C. F. Madigan and V. Bulovic. Solid state solvation in amorphous organic thin films. *Physical Review Letters*, 91:247403, 2003.

[53] M. A. Lampert. Simplified theory of space-charge-limited currents in an insulator with traps. *Physical Review*, 103:1648–1656, 1956.

[54] P. E. Burrows, Z. Shen, V. Bulovic, D. M. McCarty, S. R. Forrest, J. A. Cronin, and M. E. Thompson. Relationship between electroluminescence and current transport in organic heterojunction light-emitting devices. *Journal of Applied Physics*, 79:7991–8006, 1996.

[55] L. D. Bozano, B. W. Kean, V. R. Deline, J. R. Salem, and J. C. Scott. Mechanism for bistability in organic memory elements. *Applied Physics Letters*, 84:607–609, 2004.

[56] L. P. Ma, S. Pyo, J. Ouyang, Q. F. Xu, and Y. Yang. Nonvolatile electrical bistability of organic/metal-nanocluster/organic system. *Applied Physics Letters*, 82:1419–1421, 2003.

[57] I. G. Hill, A. Rajagopal, A. Kahn, and Y. Hu. Molecular level alignment at organic semiconductor-metal interfaces. *Applied Physics Letters*, 73(5):662–664, 1998.

[58] A. Rajagopal and A. Kahn. Photoemission spectroscopy investigation of magnesium-alq$_3$ interfaces. *Journal of Applied Physics*, 84(1):355–358, 1998.

[59] Y. Hamada, H. Kanno, T. Tsujioka, H. Takahashi, and T. Usuki. Red organic light-emitting diodes using an emitting assist dopant. *Applied Physics Letters*, 75(12):1682–1684, 1999.

[60] G. G. Malliaras and J. C. Scott. Numerical simulations of the electrical characteristics and the efficiencies of single-layer organic light emitting diodes. *Journal of Applied Physics*, 85:7426–7432, 1999.

[61] S. Naka, H. Okada, H. Onnagawa, Y. Yamaguchi, and T. Tsutsui. Carrier transport properties of organic materials for EL device operation. *Synthetic Metals*, 111:331–333, 2000.

[62] L. P. Ma, J. Liu, S. M. Pyo, and Y. Yang. Organic bistable light-emitting devices. *Applied Physics Letters*, 80:362–364, 2002.

[63] A. Fujii, Y. Ohmori, C. Morishima, and K. Yoshino. Photoluminescence queching under reverse bias in organic multilayer structure utilizing 8-hydroxyquinoline aluminum and aromatic diamine. *Japanese Journal of Applied Physics*, 33, 1994.

[64] S. Egusa, N. Gemma, A. Miura, K. Mizushima, and M. Azuma. Carrier injection characteristics of the metal organic junctions of organic thin-film devices. *Journal of Applied Physics*, 71:2042–2044, 1992.

[65] H. Hieda, K. Tanaka, K. Naito, and N. Gemma. Fluorescence quenching induced by injected carriers in organic thin films. *Thin Solid Films*, 331(1-2):152–157, 1998.

[66] C. H. Chen, C. W. Tang, J. Shi, and K. P. Klubek. *Macromolecule Symposium*, 125(49), 1997. DCJTPB is 2-(1, 1-dimethylethyl)-6(2-(2, 3, 6, 7-tetrahydro-1, 1, 7, 7-tetramethyl-1H, 5H-benzo(ij) quinolizin-9-yl) ethenyl)-4H-pyran-4-ylidene) propanedinitrile.

[67] R. H. Young, C. W. Tang, and A. P. Marchetti. Current-induced fluorescence quenching in organic light-emitting diodes. *Applied Physics Letters*, 80:874–876, 2002.